SANDIA REPORT

SAND2005-6885
Unclassified - Unlimited Release
Printed November 2005

Development of Experimental Verification Techniques for Non-linear Deformation and Fracture on the Nanometer Scale

D.F. Bahr
Mechanical and Materials Engineering
PO Box 642920
Washington State University
Pullman, WA 99164-2920

N.R. Moody
Microsystems and Materials Mechanics – 8754
Sandia National Laboratories
PO Box 969 MS 9409
Livermore, CA 94551-0969

Prepared by
Sandia National Laboratories
Albuquerque, New Mexico 87185 and Livermore, California 94550

Sandia is a multiprogram laboratory operated by Sandia Corporation,
a Lockheed Martin Company, for the United States Department of Energy's
National Nuclear Security Administration under Contract DE-AC04-94-AL85000.

Sandia National Laboratories

Issued by Sandia National Laboratories, operated for the United States Department of Energy by Sandia Corporation.

Available to DOE and DOE contractors from
U.S. Department of Energy
Office of Scientific and Technical Information
P.O. Box 62
Oak Ridge, TN 37831

Telephone: (865) 576-8401
Facsimile: (865) 576-5728
E-Mail: reports@adonis.osti.gov
Online ordering: http://www.doe.gov/bridge

Available to the public from
U.S. Department of Commerce
National Technical Information Service
5285 Port Royal Rd
Springfield, VA 22161

Telephone: (800) 553-6847
Facsimile: (703) 605-6900
E-Mail: orders@ntis.fedworld.gov
Online order: http://www.ntis.gov/help/ordermethods.asp?loc=7-4-0#online

SAND2005- 6885
Unclassified - Unlimited Release
Printed November 2005

Development of Experimental Verification Techniques for Non-linear Deformation and Fracture on the Nanometer Scale

D.F. Bahr
Mechanical and Materials Engineering
PO Box 642920
Washington State University
Pullman, WA 99164-2920

N.R. Moody
Microsystems and Materials Mechanics – 8754
Sandia National Laboratories
PO Box 969 MS 9409
Livermore, CA 94551-0969

ABSTRACT

This work covers three distinct aspects of deformation and fracture during indentations. In particular, we develop an approach to verification of nanoindentation induced film fracture in hard film / soft substrate systems; we examine the ability to perform these experiments in harsh environments; we investigate the methods by which the resulting deformation from indentation can be quantified and correlated to computational simulations, and we examine the onset of plasticity during indentation testing.

First, nanoindentation was utilized to induce fracture of brittle thin oxide films on compliant substrates. During the indentation, a load is applied and the penetration depth is continuously measured. A sudden discontinuity, indicative of film fracture, was observed upon the loading portion of the load-depth curve. The mechanical properties of thermally grown oxide films on various substrates were calculated using two different numerical methods. The first method utilized a plate bending approach by modeling the thin film as an axisymmetric circular plate on a compliant foundation. The second method measured the applied energy for fracture. The crack extension force and applied stress intensity at fracture was then determined from the energy measurements.

Secondly, slip steps form on the free surface around indentations in most crystalline materials when dislocations reach the free surface. Analysis of these slip steps provides information about the deformation taking place in the material. Techniques have now been developed to allow for accurate and consistent measurement of slip steps and the effects of crystal orientation and tip geometry are characterized. These techniques will be described and compared to results from dislocation dynamics simulations.

Finally, the stress required to cause fracture of passive films on stainless steels was studied using nanoindentation under in situ and ex situ conditions. For films formed at a passive potential, the alloy chemistry dominated the film strength. Increasing the electrolyte salt concentration from 0.01M NaCl to 0.1M NaCl and changing the substrate on which the film was grown from 904L to 304 stainless steels reduced the applied tensile stress for fracture from 1.74GPa to 1.63GPa and from 1.76GPa to 1.63GPa, respectively. Trends in film strength as a function of environment are the same between in situ and ex situ testing, suggesting the two tests are both feasible methods of analyzing environmental effects on film strength.

CONTENTS

1. Introduction

1.1 Nanoindentation of hard films / soft substrates

Metals, such as aluminum and titanium, form native oxides on the surface. In turn, these oxides enhance protection of the underlying metal against wear and corrosion. The mechanical integrity of these protective oxides needs to be characterized in order to increase protection against harsh environments. Improving the mechanical properties will lead to better product quality and a longer lifetime.

Nanoindentation has been used to study the mechanical response of various metal/ oxide systems. [1,2] During the loading of these systems, a sudden discontinuity has been observed. In some cases the sudden discontinuity has been attributed to yielding and nucleation of dislocations in the substrate [3,4] and other cases have shown that it was caused by film fracture. [1, 2,5-7] Previous studies have demonstrated via atomic force microscopy, electron microscopy, or optical microscopy that a film fracture event generates a circumferential crack around the indentation in the oxide film. [2,8,9]

Chechinen and co-workers studied the critical load and depth of the discontinuity during indentation for an Al_2O_3/Al system as a function of film thickness. [1] They showed that both the critical load and depth for thicker films followed a Weibull type distribution with parameters typical to materials with moderate brittleness and hardness. A model was developed to describe the critical parameters for load and depth. The model was in good agreement for thicker films but some deviation occurred for thinner films.

Another way to quantify film fracture is to determine the radial stress as a function of contact load needed for failure. Various analytical methods have been used to model the system. [10,11] One method was to model the film as an axisymmetric circular plate with clamped edges supported on a compliant foundation. [2,6,7] Pang and Bahr used nanoindentation to test an anodically grown TiO_2 film on a mechanically polished Ti substrate. [2] This system exhibited plastic deformation prior to the load at which the discontinuity was seen which indicates that the discontinuity was owing to thin film fracture Using the axisymmetric clamped plate model, a critical stress was quantified for each film thickness by using a superposition of the bending stress and membrane stress induced by the contact load. Stress is a common way to measure the

mechanical response of materials. However, the stress at failure is influenced by the film thickness and defect density and is not truly a material property.

A study by Weppleman and Swain used micro-indentation to study thin film fracture. [12] TiN films of various thicknesses were grown on stainless steel by physical vapor deposition methods. The induced stresses in the film/substrate system were determined by using finite element analysis. It was found that for films which are thin (h_f) compared to the radius (R) of the indenter tip (R/h_f>6.7) the first fracture was caused by high radial stresses outside the contact radius. A study by Chai and Lawn showed that the highest radial stress at the surface occurred in the region outside the contact edge for thin films. [13] Thicker films were found to have a maximum radial stress near the edge of the contact radius. A weight function was used to plot the stress intensity factors K_I and K_{II} against a/h_f where a is the crack size and h_f is the film thickness. The thin film fracture was dominated by a Mode I loading situation.

One other method to analyze film fracture is to approach the test from an energy standpoint. A critical amount of energy is required to fracture a thin film. This energy can be determined by producing a load depth curve from nanoindentation until fracture occurs. The total energy applied during the indentation can calculated by simply integration to the fracture depth. The energy used to plastically deform the substrate must be subtracted from the total energy, leaving the amount of energy needed to fracture the thin film.

Malzbender and de With [14] demonstrated that the dissipated energy during indentation was related to the fracture toughness of the coating and interface by performing simple integrations of the loading and unloading portions from indentation to determine the amount of energy needed to damage the film. The films that they produced were shown to delaminate and chip along with through thickness fracture in the film. The energy needed for delamination and chipping was then calculated. The crack extension force was then used to calculate the interfacial stress intensity and critical stress intensity for fracture. The plastic deformation in substrate was not taken into account, this will lead to an overestimation of the energy release rate.

Other studies have suggested that the fracture energy could be estimated as the energy consumed during the first circumferential crack during the load drop or plateau on the load-displacement curve. [15] Three different methods have discussed estimation methods for the fracture energy from the load-depth curves. Li *et al* [16] suggested an approach based on the idea that the total energy released during crack initiation is the fracture energy divided by the

new surface area. The total energy measured from the load-depth curve was determined by extrapolating the loading curve from the beginning of the excursion to the end. The energy method from Li *et al* is represented by the area in quadrilateral ABCD in figure 1-1. Work performed by van der Varst and de With [17] used an internal variable theory to separate the different activities that produce total dissipated energy. The extent of damage at the interface, plastic deformation in the system, damage in the system, and the generation of heat were taken into account. They used such internal variables as crack length, plastic strain, and degree of micro damage to derive a work function that only depended on the initial and final states to determine the energy. The surface roughness was found to increase the scatter in the data. However, the data was seen to follow a master curve. The indentation in the sample produced circumferential cracking outside the contact area of the tip. The work from the ring cracking was calculated by multiplying the load at the discontinuity by the discontinuity length and dividing by the surface area of the crack. This method can be represented on the load-depth schematic (figure 4-1) as the area in triangle OAC. This does not take into account the effects from the substrate and the energy calculated is an overall dissipated energy from the system, not just the film. The third energy method suggested by Abdul-Baqi and Van der Giessen [18] was to multiply one half of the cracking depth by the load jump. This method is represented by the area in triangle OAD in figure 1.1.

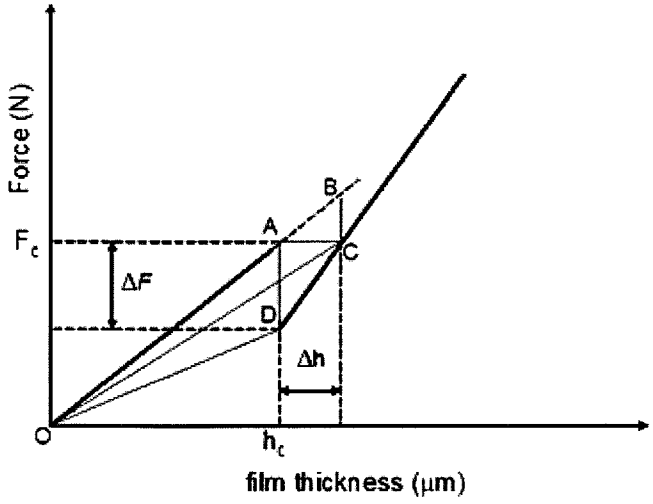

Figure 1.1 Schematic load depth curves used for fracture energy estimations. The energy estimations for Abdul-Baqi is outlined as OAD, Van der Varst and de With is OAC, and Li et al is ABCD.

Numerical simulations performed by Abdul-Baqi and van der Giessen demonstrated that the energy determination by Li *et al* was found to underestimate the overall energy for small fracture energies and small film thicknesses, where the methods by Abdul-Baqi *et al* and van der Varst *et al* were reasonable estimations. However, the second and third methods overestimate the overall energy for large fracture energies and large film thicknesses. The problem with these methods is that the loading is assumed to be linear with depth. However, the indentation follows elastic-plastic contact theories where the load and depth have a power law relationship. [19,20] Also, substrate effects were not taken into account for any of the above methods to determine the energy to initiate a crack.

In this current study a first order analytical model was developed to quantify thin film fracture using nanoindentation.. Then, we will outline a method to separate the energy dissipated from fracture of the film and the energy dissipated to plastically deform the substrate. Being able to separate these energies from the total energy applied by the nanoindenter allows a determination of the energy release rate for film fracture and calculating the critical stress intensity factor under plane stress.

1.2 Analysis of slip steps around indentation

It was shown in earlier work at Washington State University [21] that AFM can be used in conjunction with OIM to identify specific slip planes responsible for any particular slip step visible on a material's surface around an indentation. Similar techniques have been used to identify slip steps around STM tip indentations in gold [22], within the cavity left by spherical indentations in MnZn ferrite [23], and around Berkovich indentations in MgO and LiF [24-26]. None of these works, however, can explain a mechanism for the development of the observed steps which predicts the affects of changing variables such as surface orientation, tip geometry or different mechanical properties of materials, or are directly comparable to the capabilities of dislocation dynamics.

Much of the knowledge currently available in the literature in regards to the mechanics of indentations is entirely phenomenological. Material properties such as hardness can be measured and used for comparison purposes, however no mechanistic information, such as why a material is harder or softer, can be gathered from an indentation test alone. Nor can traditional hardness

tests determine exactly how a minor change in microstructure or composition will change the bulk mechanical behavior of a material. Slip steps should provide a useful insight into the development of the plastic zone around indentations and the dislocation mechanisms taking place during deformation.

Relating surface slip steps to changes in deformation mechanisms could allow indentation testing to be a very powerful empirical benchmark for validating dislocation dynamics (DD) and mezzo-scale modeling simulations. TEM is often used as a tool for experimental validation of atomistic simulations, but it is often too limited to be very useful for examining the larger length scales which can be employed in DD and combination finite element analysis (FEA) – DD simulations. In this way, problems such as hydrogen embrittlement and the contribution of grain boundaries to deformations can be modeled using DD simulations and experimentally verified using indentation testing.

Observation of slip steps around indentations have shown that the pattern of slip steps is very consistent and repeatable for indentations made in the same material and with the same indenter tip and loading conditions. The general formation of these slip step patterns changes only with changes in the crystal structure and orientation of the material being indented. Smaller variations occur with changes in the geometry of the indenter tip and stacking fault energy of the material. Observation of these steps alone cannot provide quantitative values of the stresses around the indentation, however, they can provide a qualitative view of the stress state that must be present to cause a particular pattern of slip steps.

1.3 Film fracture testing in corrosive environments

The passive film on stainless steel alloys is a dynamic system which continuously reacts with its surrounding environment. This makes structural and properties characterization challenging. Whatever precaution is taken to transfer the sample on which the film is grown from the electrolyte to ambient laboratory conditions or an ultra high vacuum chamber, the passive film changes during the transition [27]. In-situ studies of passive films overcome the change in the passive film due to the exposure to atmosphere and allow investigation of the films in their service conditions. While many surface analysis methods are not compatible with aqueous environments, mechanical properties of the passive films can be compatible with these solutions.

The presence of a passive film influences the mechanical properties of a stainless steel (SS). Li *et al* [28] studied the influence of the passive film formed on 321SS in $MgCl_2$ solution at 115°C for an hour on the yield stress of the alloy. Due to generating an additive stress which increased dislocation multiplication and motion, the passive film decreased the yield stress of the specimen from the flow stress of specimen without film. Other researchers have performed bulk experiments which enable measurements of passive film strength, but these usually couple both the bulk metallic alloy as well as the very thin passive film [29-32].

Chiba and Seo [33] investigated the friction coefficient, which is the ratio of the lateral force to the normal force under contact loading, of a passive iron surface passivated in borate solution by comparing the results of in-situ and ex-situ nanoscratch tests: The friction coefficient obtained with ex-situ nano-scratching was remarkably smaller than that obtained with in-situ nanoscratching; in-situ nanoscratching results shown that increasing the potential in the passive region resulted in a higher friction coefficient. On the other hand, the friction coefficient obtained with ex-situ tests was independent of the applied potential. They suggested that repassivation of the rupture sites at the moving front of the indenter tip resisted the movement of the indenter due to the pile up formed by the repassivation process. The repassivation process was promoted by the potential difference between the substrate and the solution. Mudali and Katada [34] used Electrochemical Atomic Force Microscopy (ECAFM) to study passive films formed on nitrogen-bearing austenitic stainless steel, and demonstrated that the stiffness of passive films decreased with an increase of the applied potential. However, ECAFM can not truly quantify the strength of the films. The slope of the force-displacement curve of AFM tip contacting the passive film showed that in situ tests were softer (or more compliant) than ex situ tests.

The nanoindentation technique is widely used to probe the mechanical properties of small volumes [35]. This method produces a continuous record of the penetration depth of an indenter as the load is increased between the tip and sample, producing what is referred to as a loading-unloading curve. Discontinuities in this loading curve are indicative of either dislocation nucleation and multiplication or a through-thickness fracture of the film. The load discontinuity is most likely indicative of film cracking rather than dislocation nucleation and multiplication if the material exhibits permanent deformation prior to the load discontinuity [7,36].

In our previous studies [37,38], ex-situ nanoindentation tests were made to investigate the influences of alloy and solution chemistries on the load required to fracture the passive film formed on austenitic stainless steel alloys at anodic potentials where the passive film is stable and metastable. For the passive film formed at a stable passive potential, the substrate on which the film was grown was the most significant factor affecting the load at fracture. On the other hand, the salt concentration and the substrate on which the film was formed were the two factors impacting the load at fracture of the passive film formed at a metastable pitting potential.

In this current study, in-situ nanoindentation tests were preformed to simultaneously evaluate the effect of multiple variables using the Taguchi method; particularly salt concentration, time, pH, temperature, and alloy composition on the load at fracture of passive films formed on austenitic stainless steel alloys at two representative potentials, a stable passive potential and a metastable pitting potential. The loads at fracture for the film tested in-situ and ex-situ [37,38] were used to roughly compute and compare the tensile stress applied needed to fracture the passive film using Hertzian contact mechanics.

2. Experimental Procedures

Two different aluminum substrates were used in this study. The samples were made from a commercially available ingot of 1100 aluminum and a 99.99% pure Al ingot. The substrates were encapsulated in an evacuated quartz tube, back filled with argon gas and annealed at 500°C for 24 hrs. After annealing, samples from both materials were polished. One set of samples from the 1100 Al and 99.99% pure aluminum were mechanically polished by grinding the samples to 1200 grit and then polishing to 0.05μm with colloidal silica. Another set of samples from the 1100 Al was electropolished in an electrolyte of 25% Nitric acid and 75% methanol at -20°C using a bias of 10V. After polishing, different film thicknesses were obtained by thermally growing oxides at 500°C for 1, 2, and 3 hrs and air quenching at room temperature. The oxide growth was shown by Aylmore, Gregg, and Jepson to follow a linear law with time between 500 and 550°C. [39] Using the linear law, the theoretical film thickness should be 35nm, 50 and 65 nm for 1, 2, and 3 hrs growth time at 500°C, respectively. The oxide thicknesses were measured using a Gaertner spectral ellipsometer, and were determined to be 25, 54, and 63 nm for 1, 2, and 3hr growth times, respectively. The oxide thickness was not influenced by the underlying substrate in these materials. Gulbransen and Wysong studied the growth of aluminum oxide on

aluminum and over a temperature range of 400 to 500°C. [40] The oxide layer was found to be amorphous in structure but the heating time was only 30 min. [40,41]. A final set of experiments was carried out on anozided aluminum substrates to "scale up" the oxide thickness to allow more detailed observations in the scanning electron microscope.

The aluminum substrates were polycrystalline. Three grains with different crystallographic orientations on the 99.99% pure aluminum substrate were tested using nanoindentation to examine influence of grain orientation. The orientations were determined using electron backscattered diffraction (EBSD).

Another set of experiments was performed on Grade II polycrystalline titanium with a primarily α HCP grain structure. These samples were ground to 600 grit and then mechanically polished using 0.05 μm colloidal silica. A thin oxide was then anodically grown using an EG&G 173 and 175 potentiostat and controller. The film was grown in a 0.1 M H_2SO_4 solution. The final potential was reached using step polarization. The potential was increased by 1V every few minutes (once the current density stabilized at each potential) until a maximum of 9.4V was reached. The potential was measured against an Ag/AgCl reference electrode and a graphite counter electrode. The sample was then held at the maximum potential for 5min. The titanium oxide thickness was determined using x-ray photoelectron spectroscopy (XPS) depth profiling. A sputtering rate of 35 angstroms per minute was used. The thickness of each oxide was measured by determining the depth at which the oxygen is 50% of its maximum concentration. The film thickness was found to be 200nm.

Nanoindentation for thin film fracture was carried out using a Hysitron Triboscope coupled with a Park Autoprobe scanning probe microscope. The indentations were made with a cube corner diamond indenter (90° included angle) with an effective tip radius of 570 nm. The tip radius was calculated by performing a series of elastic loading curves in tungsten. A tip radius was then calculated for each elastic curve using the Hertzian elastic loading profile. [19]. The Al_2O_3/Al systems were then indented with maximum loads ranging from 15μN to 5000μN. Atomic force microscopy (a Park Autoprobe CP) was used to measure surface roughness.

Most of the experiments for slip step analysis were performed in 21-6-9 stainless steel. This is a nitrogen strengthened austenitic alloy with the composition shown in Table I. A few of the experiments used a commercially pure nickel alloy, Ni200. Both alloys were prepared by

annealing in air to produce a very large grain size, producing microstructures with grains in excess of 1mm in diameter in both alloys. Several samples of each material were cut from these annealed specimens and mechanically polished to a 0.05 μm colloidal silica finish. Each sample was then scanned using EBSD to reveal a map of the surface orientations of many grains across much of the sample area. These grain maps were then used to select large grains with orientations near {001}, {011} and {111} for subsequent indentation experiments.

Table I Composition of the 21-6-9 stainless steel used in this study.

Element	Fe	Cr	Ni	Mn	N	Al	C	O	P	S	Si
Wt %	balance	19.1	6.9	9.5	0.26	0.012	0.034	0.0005	0.023	0.0002	0.51

Two types of indentation experiments were carried out in these selected grains; conventional microhardness testing using a Leco microhardness tester with a Vickers tip and a conical tip as well as instrumented indentations using a Nanoinstruments Nanoindenter II with a 90° conical tip. The conical tip used in the microhardness indenter is nominally a 90° tip but has a blunt tip radius of approximately 23 μm whereas the tip used in the Nanoindenter has a tip radius of approximately 1 μm. These tips will be referred to in this paper as the blunt and sharp conical tip, respectively.

Indentations were imaged *post facto* using contact mode AFM in a Park Autoprobe CP scanning probe microscope to reveal the formation of slip steps around indentations. Most AFM images presented in the paper are either deflection images or derivative images of height information to accentuate small surface features.

The materials and the procedure used to prepare the specimens for corrosion testing can be found in details in refs. [37,38]. In summary, an EG&G 173 and 175 potentiostat and controller were used to grow the passive films. Aqueous chloride test solutions, adjusted to the required pH and salt concentration by HCl and NaCl, were used to fill a small glass electrochemical cell especially designed for in-situ nanoindentation as shown in figure 2.1, with Ag/AgCl and platinum as reference and counter electrodes, respectively. A Peltier element was used to achieve the desired temperature of the electrolyte. The required solution temperatures were measured prior to experimentation and were determined by varying the applied DC voltage

to the Peltier element until the desired temperature was reached. To protect the scanner of the scanning probe microscope, an aluminum heat sink was used to minimize the temperature gradient between the cell and scanner.

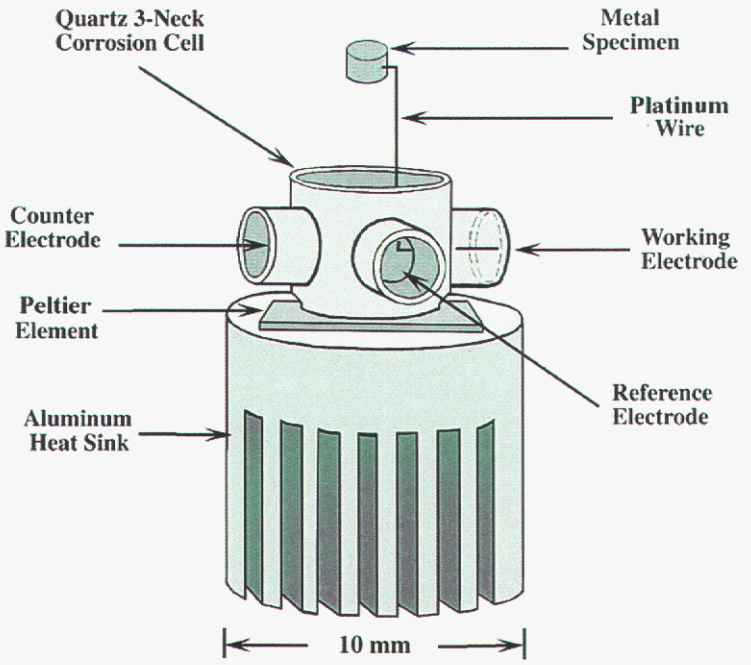

Figure 2.2 Schematic of the electrochemical cell created for in situ nanoindentation

Nanoindentation fracture load measurements of anodically passive films formed were performed using a Hysitron Triboscope with a Park Autoprobe CP Scanning Probe Microscope (SPM). A maximum force of 500 μN was used for the nanoindentation tests. The in-situ indentation tests were made using a Berkovich tip with a tip radius of curvature of approximately 730nm and a loading rate of 50 μN s^{-1}, while ex-situ tests were made at the same rates using either the Berkovich tip or a cube corner tip with a tip radius of approximately 450 nm. Solutions of 0.01, 0.05, and 0.1 M NaCl salt concentrations at pH's of 1, 3, and 5 were used in this study. To measure the fracture load of the passive film formed in an electrolyte, the potential was held cathodically for approximately 40 minutes. Then the sample was anodically

polarized at constant rate of 2mV/s to and then held for two hours to grow the passive film; indentations were performed while the sample was under the electrochemical control using the potentiostat. The spring constant calibration for the nanoindentation loading system was performed within a couple μm of the sample surface to minimize the effect of contact angle between the electrolyte surface and the extension of the tip. Other researchers have found that this angle influences the loading capabilities due to the surface tension [42].

3. Results of indentation – oxide film fracture tests

An EBSD image of one of the samples can be seen in figure 3.1 along with the orientation color code for a face centered cubic crystal structure. The three different grains which were tested are represented as squares in figure 3.1. The resulting load-depth curves from each graph overlap each other. This shows that the surface of the sample is more influential to the loading profile than the orientation in this material and therefore will not be considered in this study.

Two typical load depth curves from indentations into the electropolished 1100 aluminum with a 63 nm thick oxide are shown in figure 3-2. A maximum load for one of the indentations was chosen to produce a discontinuity in the load-depth curve. The second indent was unloaded prior to the load at which the discontinuity occurred in the other indentation.

The load-depth curve with a maximum load prior to the discontinuity resulted in a residual depth after indentation. This residual depth demonstrates that plastic deformation occurred in the system during indentation, indicating the presence of dislocations and the discontinuity was not caused from a yielding phenomenon (a sudden nucleation and multiplication of dislocations). The two solid lines represent the theoretical elastic response if the indentations followed the Hertzian elastic response for aluminum (E_r= 69 GPa) and crystalline aluminum oxide (E_r = 302 GPa) for the tip. The indentation experiment shows that there is a deviation from the theoretical elastic response, again suggesting plastic deformation is occurring in these systems prior to the discontinuity. This therefore precludes dislocation nucleation as the cause of the discontinuity and suggests it is due to film fracture. [2] Similar curves were produced for the mechanically polished 1100 aluminum and mechanically polished 99.99% pure aluminum.

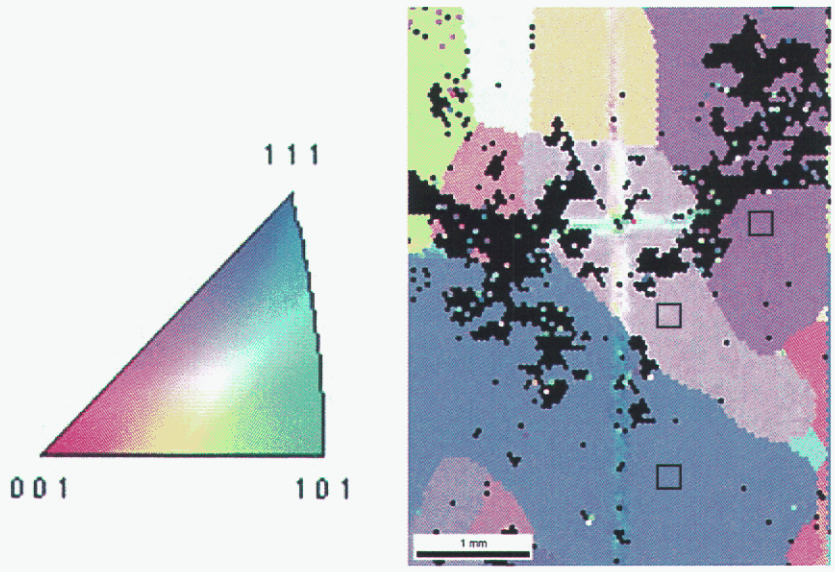

Figure 3.1 Orientation imaging microscopy of an electropolished 1100 aluminum alloy showing the grain size and crystallographic direction

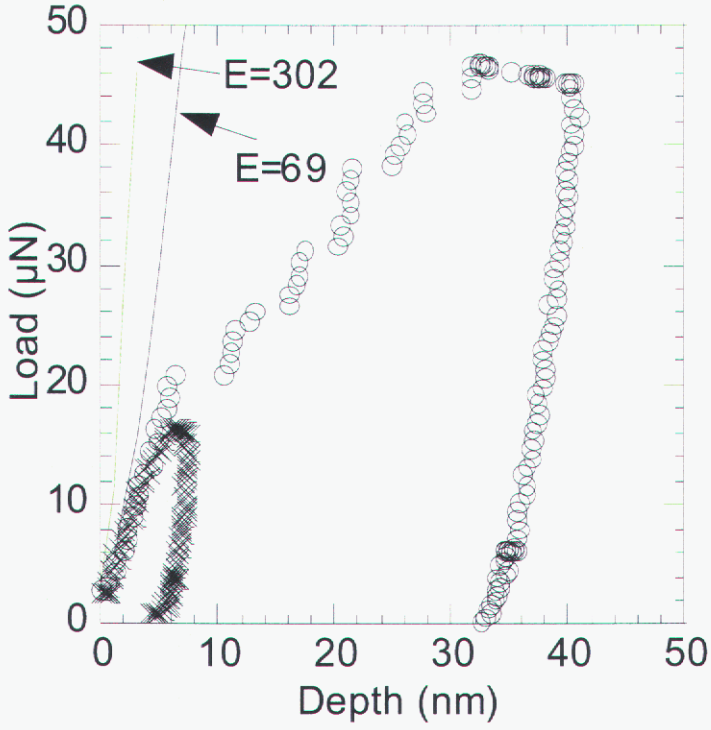

Figure 3.2 Representative load-displacement curves for the 63nm thick oxide on the 99.99% Al substrate with maximum loads prior to and above the discontinuity.

The cause of the sequential discontinuities after the first could not be determined. Multiple discontinuities have also been attributed to the phenomenon of yielding. This is referred to as "staircase" yielding. During indentation mobile dislocations may become immovable through interactions with diffusing solute atoms or other dislocations. [43] The immovable dislocations would break free and become mobile at a critical stress. Continuous interaction of dislocations and increasing the indentation load could lead to "staircase" yielding. However, in the current experiment it would be unlikely that dislocation nucleation would become the controlling factor during this indent. Observations show that multiple cracking and crushing of the film is occurring during continuous loading past the first discontinuity. Figure 3-3 shows an indentation with a maximum load well beyond the critical load for the first excursion.

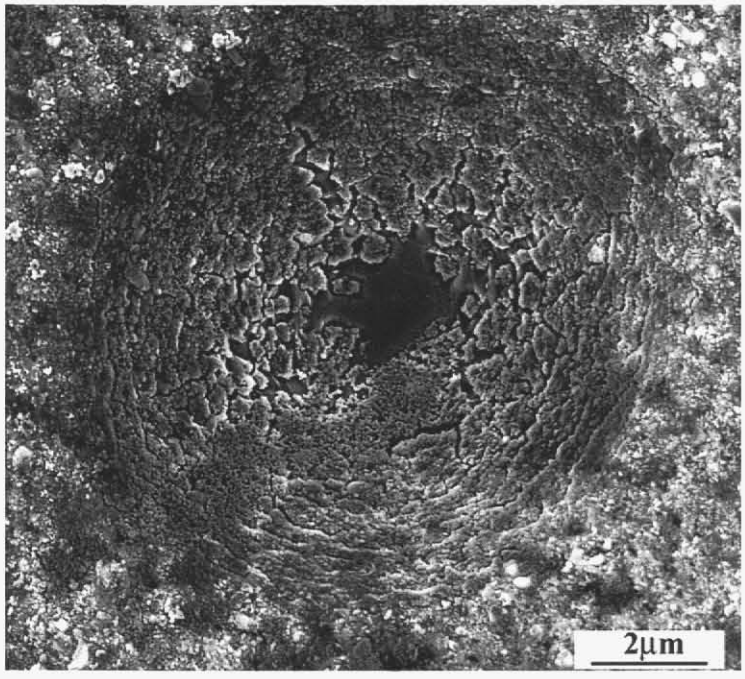

Figure 3.3 Micrograph of an indentation made well beyond the first discontinuity with sequential discontinuities in the load-depth curve

Circumferential cracking dominates at the edge of the indentation. Crushing of the film occurs as closer to the center of the indentation. The center region is exposed aluminum.

Atomic force microscopy was carried out to attempt to identify the crack around the indentation, which was expected to be similar to previous studies. [2,8,9] However, the roughness of the thermally grown oxide was approximately 20-30% of the film thickness. An

AFM image of the thermally grown oxide films can be seen in Figure 3-4. He, Evans, and Hutchinson [44] has also been shown that a ratcheting effect occurs on thermally grown hard films on ductile substrates. The ratcheting effect is caused from the film undergoing compression during the cooling of the film from thermal expansion. The ductile substrate alloyed the film to deform and a rough surface is produced. Tolpygo and D.R. Clarke [45] studied the growth of an alumina thin film by thermal oxidation on an Fe-Cr-Al alloy. The study was found to show a wrinkling morphology of the alumina surface. This provided a rough surface which limited the ability to find cracks in the oxide during indentation. This rough surface, which exhibited equiaxed grains of approximately 100 nm in diameter, made unambiguous identification of the specific crack of interest impossible. However, this roughness provides the motivation for choosing a possible initial crack size in the following fracture analysis. Both AFM and use of the Hysitron imaging system show no evidence of any significant pile up or sink in phenomena in the materials in this study.

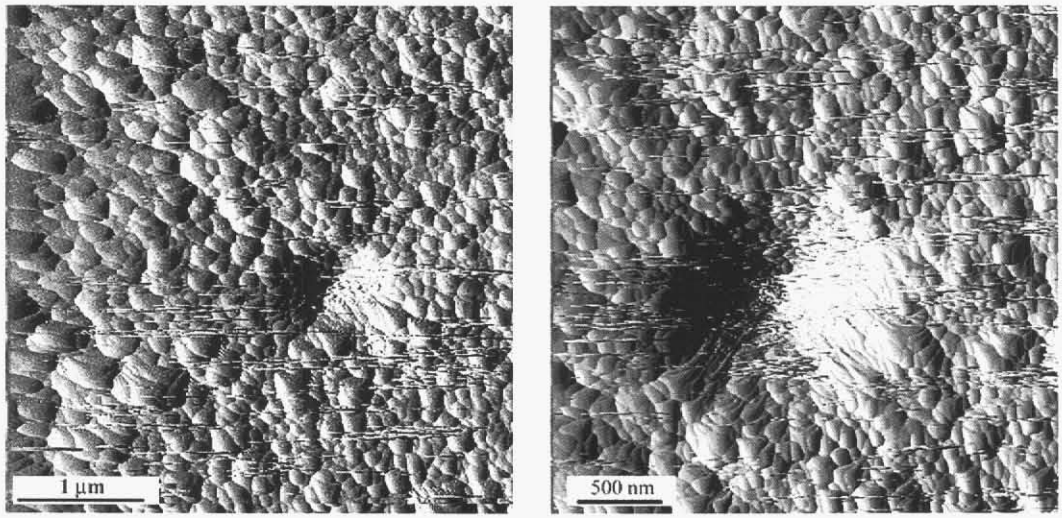

Figure 3.4 Micrographs of a thermally grown oxide on a mechanically polished 1100Al substrate using atomic force microscopy. Film fracture could not be observed due to the resolution of the atomic force microscope.

A scaled up version of the aluminum oxide-aluminum system was produced by anodization. Producing the oxide by means of anodization was chosen because of its minimal surface roughness. The anodized film contained porosity but the porosity did not effect the position of the circumferential crack and was thicker than the thermally grown oxides. This was

to increase the resolution in order to observe the cracking in the film. Figure 3-5 shows the corresponding load-depth curves for the indentation micrographs in figure 3-6. The load-depth curve that reached a maximum load of 10mN produced circumferential cracking around the indentation (fig. 3-6a). The crack was positioned outside the contact area of the indenter tip. The tip contact radius is noted as a_c and the crack distance from the center of the indent is marked as c. Figure 3-6b shows the corresponding micrograph for the load-depth curve with a maximum load of 7mN. The corresponding load-depth curves for the shows that the circumferential is accompanied by a discontinuity at about 8mN. The discontinuity at 5mN was caused from the porosity in the film. The porosity allowed the film to be crushed under the applied load of the indenter. This does not occur in the thermally grown oxides because porosity was likely not present.

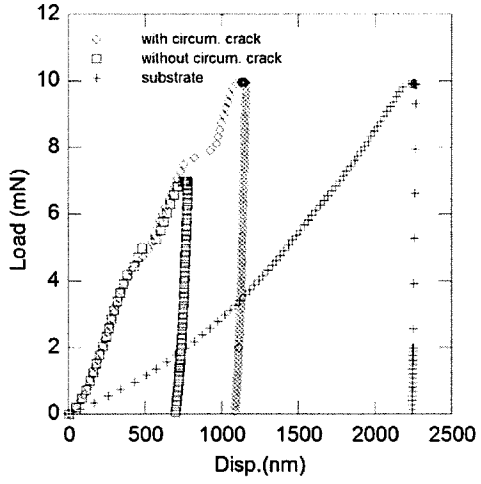

Figure 3.5 Load-depth results from two indents into an anodized aluminum with maximum loads of 7mN and 10mN along with a resulting load-depth curve into the aluminum substrate without a film.

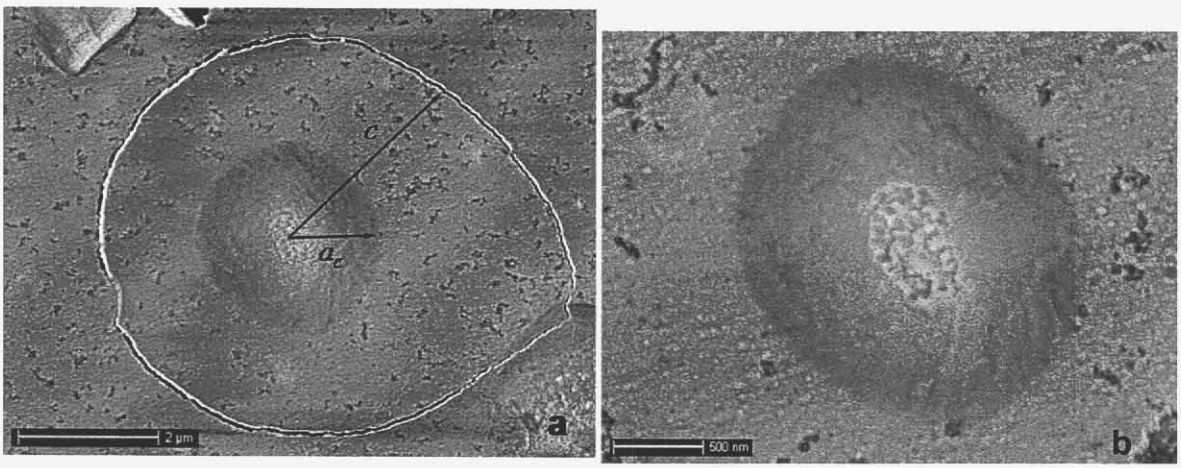

Figure 3.6 Micrographs of indentations on anodized aluminum with maximum loads of a) 10mN and b) 7mN. A circumferential crack occurred around the indentation in micrograph a (10mN max load) where cracking was not present in micrograph b (7mN max load).

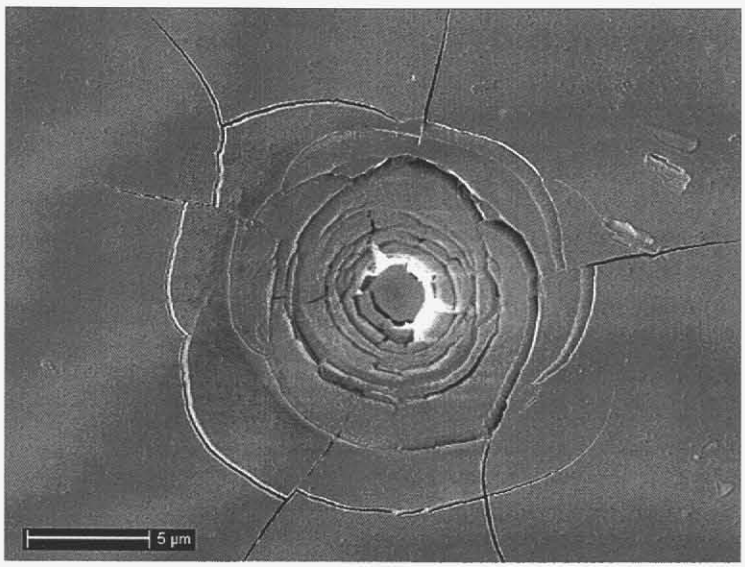

Figure 3.7 Sequential film cracking of the anodized aluminum

Figure 3-7 shows an indentation beyond the first discontinuity for the anodized aluminum. The indentation beyond the first discontinuity showed that sequential circumferential cracking occurred and then radial cracks developed, very similar to figure 3-3. The sequential circumferential cracks were present in an indentation study of submicron silica films on a

polymer substrate by Andersson *et al.* [9] The silica film had an amorphous structure similar to the films in the current study.

The critical load and depth at each discontinuity were recorded and a histogram was produced for each substrate as shown in figure 3-8. The first critical loads and depths were found to follow a normal distribution.

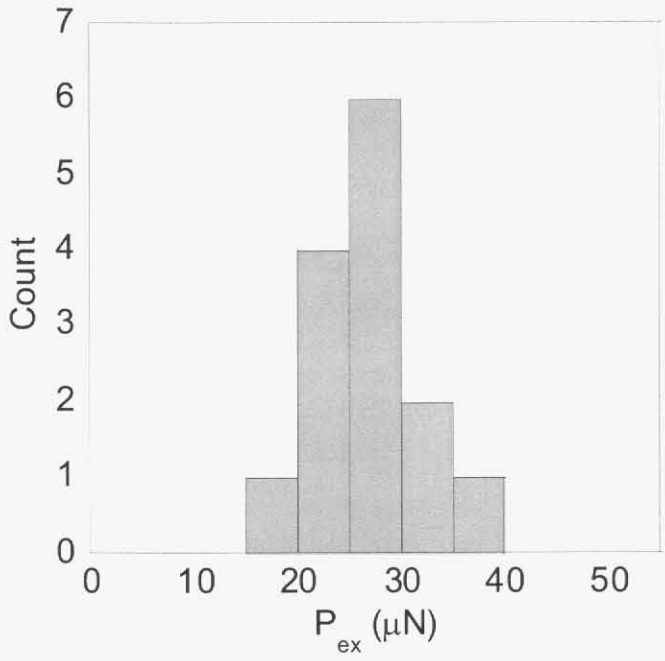

Figure 3.8 Representative histrogram of the critical loads for the 1100 electropolished substrate with a 54 nm thick film. The histogram shows that critical loads follow a normal distribution.

A summary of the average critical loads for the oxides grown on the 1100 and 99.99% mechanically polished substrates along with the 1100 electropolished aluminum substrate is shown in figure 3-9. The applied load at fracture stayed constant for each substrate with increasing film thickness. The thermally grown oxide on the 99.99% pure aluminum substrate was found to fracture at critical loads larger than the oxide grown on the 1100 aluminum substrates. The 25 nm thick film on the 99.99% aluminum substrate fractured at an average load of 49.4 μN. The 25 nm thick oxides on the mechanically polished 1100 and the electropolished 1100 substrates fractured at an average load of 29.26 and 24.75 μN, respectively.

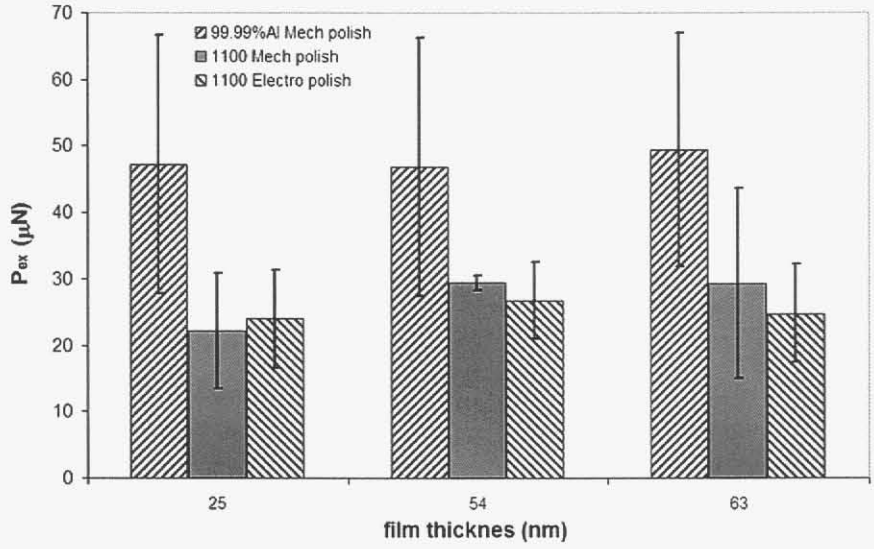

Figure 3.9The average critical loads were found to be relatively constant for a given substrate. The 99.99% Al substrate had a larger critical load than the 1100 Al substrate.

Estimating the applied radial stress at failure is a better way to evaluate thin film fracture than merely examining the loads if we are going to compare results between laboratories. The radial tensile stress applied to the film is a function of film thickness, plastic zone size in the substrate, modulus of the film, and the critical deflection of the film. The radial stress at failure was determined by modeling the indentation as a point load on a hard elastic plate on a soft substrate in similar tests during previous studies. [2,7] During indentation it is assumed that the film elastically deforms until brittle fracture. We assume that given the relative hardness differences between alumina and aluminum that the plastic deformation in the system is occurring entirely in the substrate. The film can then be modeled as an elastically deforming axisymmetric circular plate with a clamped edge. The clamped edge was defined as the end of the substrate plastic zone radius. The plastic zone radius can be approximated by [46]

$$c = \sqrt{\frac{3P_s}{2\pi\sigma_f}} \qquad (1)$$

where P_s is the load carried by the substrate and σ_f is flow stress. The load carried by the substrate was found to empirically follow a power law relationship from the load (P) displacement (δ) curve of the substrate with just the native oxide. [47]

$$P_s = K\delta^n + C \qquad (2)$$

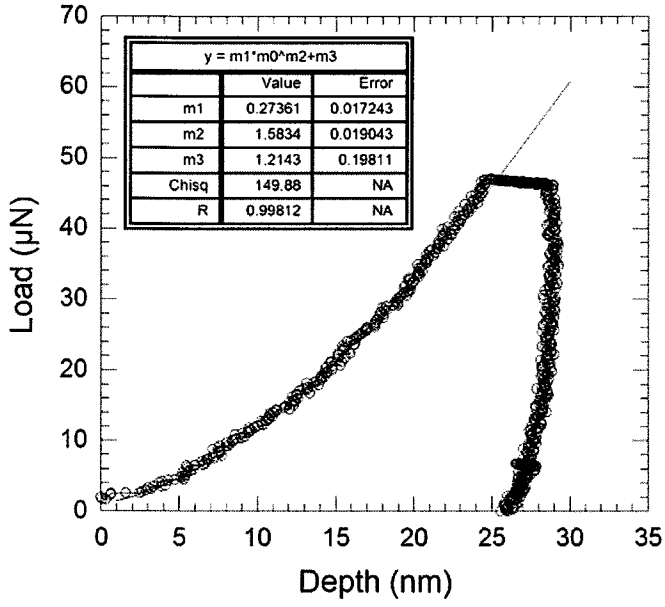

Figure 3.10 Curve fit operations for the mechanically polished 1100 Al substrate

The constants for the mechanically polished 1100 substrate were 0.274, 1.58, and 1.21 for K, n, and C, respectively. The constants were taken from curve fitting the loading profile from indentations with a maximum load of 900μN. Figure 3-10 illustrates the curve fit on an indent with a maximum load of 50 μN. Superimposing the loading profile of the substrate and the load-depth curves from the film/substrate system shows that the at a given depth the substrate will carry a smaller load. The load-depth curves from the underlying substrate and the film/substrate system can be seen in figure 3-11. The oxide film has a higher stiffness than (E = 411GPa) than the underlying substrate (E=72 GPa) which ables the film/substrate to carry a higher load at lower depths than solely the substrate. Even for an amorphous film (E=150 GPa) similar behavior should be noted.

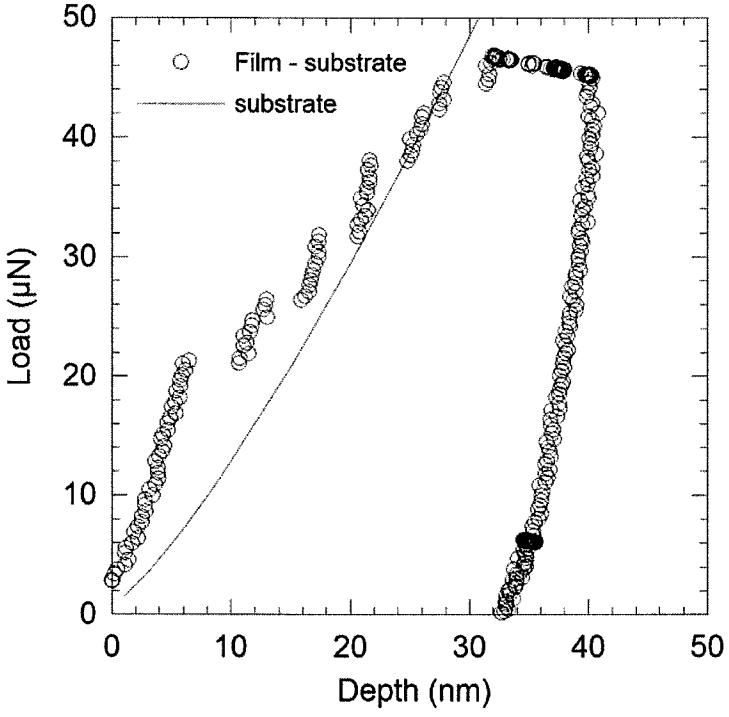

Figure 3.11 The loading profile for the indent into the 1100 aluminum substrate reaches a smaller load at a given depth than the film substrate system

The radial stress has been demonstrated to cause the through thickness cracking of a hard film on soft substrate. [12] The radial stress prior to fracture can be estimated from a superposition of the bending stress and stretching stress created from the contact load [48]

$$\sigma_r = 0.357E_f \frac{\delta^2}{c^2} + 2.198E_f \frac{\delta h_f}{c^2} \qquad (3)$$

where δ is the depth at fracture, h_f is the film thickness, E_f is the modulus of the film (assumed to be 411 GPa, references provide ranges between 380 [49] and 415 [50] GPa) and 0.375 and 2.198 are empirical constants for the stretching and bending stresses. [48] The bending stress, stretching stress, and the overall radial stresses at fracture for the chosen parameters can be seen in table 2

Table 2 Summary of average applied loads and calculated stresses at fracture

Substrate	h_f (nm)	Load (μN)	bending stress (GPa)	membrane stress (GPa)	radial stress (GPa)
99.99%	25	47.23 +- 19.40	2.44 +- 0.15	0.15 +- 0.10	2.59 +- 0.10
Mechanically polished	54	46.81 +- 19.37	5.28 +- 0.24	0.19 +- 0.07	5.57 +- 0.18
	63	49.40 +- 17.53	6.02 +- 0.33	0.19 +- 0.09	6.21 +- 0.29
1100	25	22.12 +- 8.71	3.47+- 0.04	0.14 +- 0.01	3.61 +- 0.03
Mechanically polished	54	29.43 +- 1.14	7.43 +- 0.09	0.15 +- 0.01	7.58 +- 0.08
	63	29.26 +- 14.35	8.73 +- 0.24	0.14 +- 0.03	8.87 +- 0.21
1100	25	23.97 +- 7.43	1.86 +- 0.06	0.10 +- 0.02	1.96 +- 0.04
Electropolished	54	26.73 +- 5.85	3.92 +- 0.19	0.11 +- 0.03	4.03 +- 0.02
	63	24.75 +- 7.38	4.68 +- 0.22	0.10 +- 0.04	4.77 +- 0.19

The film thickness and the radial stress to failure were linearly proportional as the thickness was increased from 25 nm to 63 nm. As mentioned before, the radial stress is a superposition of a bending stress along with membrane stress. Separating the total radial stress at failure shows that the bending stress is significantly larger than the membrane stress in this film system. The separation of the total radial stress at fracture into its bending stress and membrane stress can be seen figure 3-12.

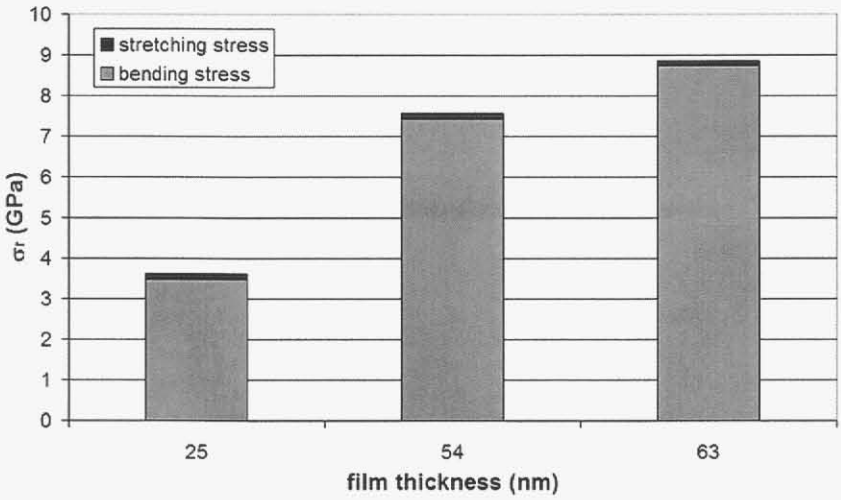

Figure 3.12 The total radial stress at fracture for the thermally grown oxide on the 1100Al mechanically polished substrate. The radial stress at fracture increased with film thickness and is dominated by the bending stress.

The oxide film on the mechanically polished 1100 substrate had a critical radial stress of 3.61 to 8.87 GPa for the 25 nm and 63 nm thick films. The membrane stress was found to stay constant for the different substrate materials and corresponding preparation technique. The membrane stress at failure depends on the critical depth, the plastic zone size, and the modulus of the film. The bending stress has a linear relationship with film thickness. Increasing the film thickness was the main contributor to the increase in radial stress at failure.

The spherical cavity model under nanocontacts is an estimation into plastic zone size in the underlying substrate. The assumption made throughout the current study is that the through thickness cracking of the oxide films occurs at the plastic zone boundary. Physical observations for the location of the through thickness cracking were made with the use of a scanning electron microscope. Micrographs were taken of two indentations made into the anodized aluminum oxide (Figure 3-13). A circumferential crack occurred during loading for both indents outside the contact area of the tip. The spherical cavity model estimated the circumferential crack radius to be a) 2.77 and b) 2.82μm. The calculation for the radius is dependent on the load carried by the substrate even though both indents in figure 3-13 had same maximum applied load by the indenter. The load carried by the substrate at fracture for two indents is a) 1.94 and b) 2.00mN. The radius for the circumferential crack in micrograph 3-13a was 2.3 and 2.5μm and in figure 3-13b was 2.9 and 3.7μm, depending on where the measurement was made. The measurement for circumferential radius is reasonably similar to the estimation made by the spherical cavity model under nanocontacts.

Surface flaws can greatly reduce the ultimate strength for thin films. These detrimental flaws are not necessarily well developed cracks. [51] However, a surface crack would be a worst case scenario. Propagation of the cracks could lead to a complete failure leaving the underlying metal exposed to the environment and loss of wear protection. A stress intensity factor can be calculated for a given material and crack dimension. Once the critical stress intensity factor has been reached the crack would propagate. Estimating the stress intensity at fracture for thin film applications would tell how much external load and what crack size would cause fracture.

The critical radial stresses showed that fracture of the thin film in this system was primarily caused from bending. The plate bending created a bending moment at the clamped edge of the flat circular plate (this model was previously used for estimating the radial stress). A

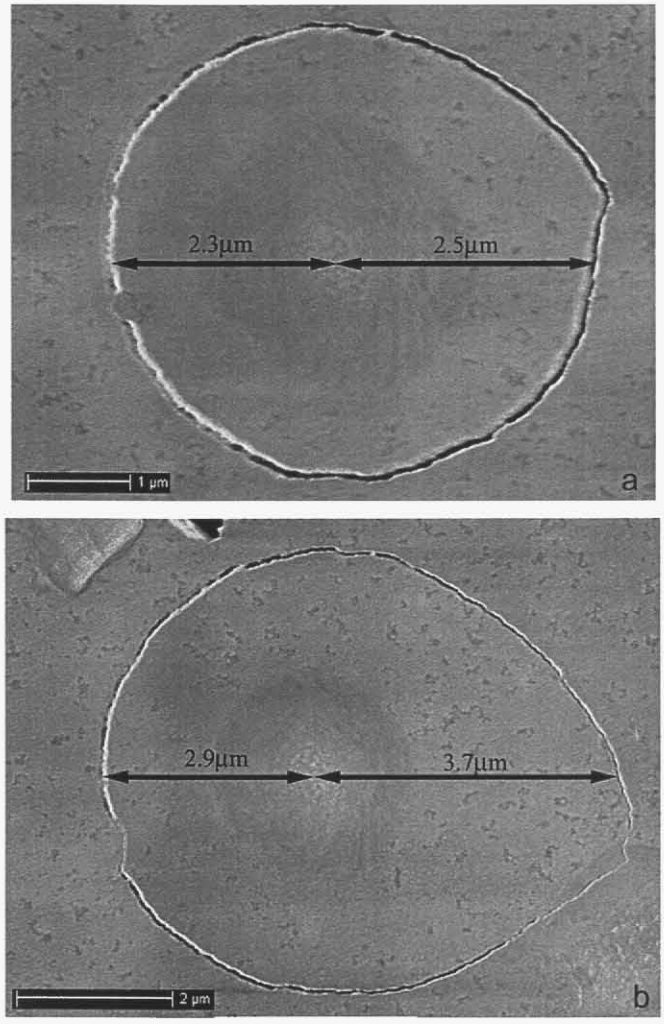

Figure 3.13 Physical observations of circumferential cracking measured a radius of a) 2.3 to 2.5µm and b) 2.9 to 3.7. The fracture radius was estimated to be a) 2.77 and b) 2.82µm using the spherical cavity model.

schematic of the resulting bending moment can be seen in figure 3-14. The overall applied load from the indenter tip is partially supported by the film and partially by the substrate. The load carried by the film does not influence the bending moment at the point of fracture. The only repulsive force, to the overall applied load by the indenter, that contributes to the bending moment is load supported by the underlying substrate.

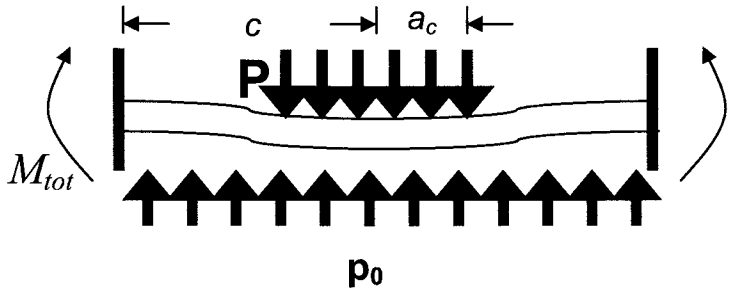

Figure 3.14 Schematic of the applied bending moment for a circular flat plate with clamped edges on a compliant foundation.

However, instead of using a point load (as was examined for the stress in the film) a more appropriate method is to assume that the contact load forms a circular projection on the film where the radius is less then the radius of the circular plate. For a first order approximation a uniformly loaded region corresponding to the contact area can be used (as shown in figure 3-14). While the actual loading profile follows elastic-plastic contact theories, the added complications of having an elastic film on a plastically deforming substrate make the imposition of a Hertzian pressure distribution challenging and as a starting approximation the uniformly loaded indentation radius will be used in this study. The bending moment M_θ can be estimated from [52]

$$M_\theta = \frac{P}{4\pi}(1+\nu)\left(\frac{a_c^2}{4c^2} - \ln\frac{a_c}{c}\right) \tag{4}$$

where P is the external applied load from the indenter, ν is poisson's ratio, a_c is the contact radius, and c is the radius of the circular plate (in this case it is the plastic zone radius).

There is also a second moment produced from the substrate applying a repulsive force that was opposite in direction of the indenter load. The moment created by the substrate M_{sub} can be modeled as a uniformly loaded circular plate [52]

$$M_{sub} = \frac{p_0 c^2}{8} \tag{5}$$

where p_0 is the uniform pressure carried by the substrate. The total moment acting at the clamped edge of the plate is a superposition of the two moments acting on the film.

$$M_{Tot} = M_{\theta} - M_{sub} \tag{6}$$

A first order approximation of the stress intensity factor can be calculated from the total bending moment produced at the clamped edge. Neglecting the radial force, because there is minimal stretching of the film from the contact load and assuming the residual stress is negligible, the stress intensity factor is [53]

$$K = \sigma\sqrt{\pi a}F\left(a/h_f\right) \tag{7}$$

where a is length of the surface crack, σ is the stress in the film at the clamped edge and $F(a/h_f)$ is a correction function taking the film thickness and the crack size into account. [53] Since the hardness of the substrate is about 200 MPa (corresponding to a tensile strength of about 75 MPa), the total residual stress which could develop in the system would be mitigated by plastic deformation in the underlying aluminum during cooling. As these stresses are much lower than those imposed by the indentation, to first order they will be ignored. The stress at the plate edge can be calculated by [53]

$$\sigma = \frac{6M_{tot}}{h_f^2} \tag{8}$$

Physical measurements of the initial crack size could not be performed due the surface topography of the oxide, only an estimate of this size can be made by examining the roughness of the samples. Pre-existing surface flaws would have a distribution of sizes and orientations. The critical surface flaw would be oriented perpendicular to the radial stresses. Therefore, to a first order, the applied stress intensity at fracture will be calculated using a constant a/h_f and then by varying a/h_f.

The applied stress intensity factor for a constant normalized critical crack size of 0.3 can be seen in figure 3-15. The stress intensity factor was highest for thinner films and decreased asymptotically towards a critical value for thicker films for all three substrates. The applied stress intensity factor for the thermally grown oxide on the 1100 mechanically polished, 1100 electropolished, and the 99.99% pure Al substrate were 0.17, 0.32, and 0.57 $MPam^{1/2}$, respectively, for the thicker films.

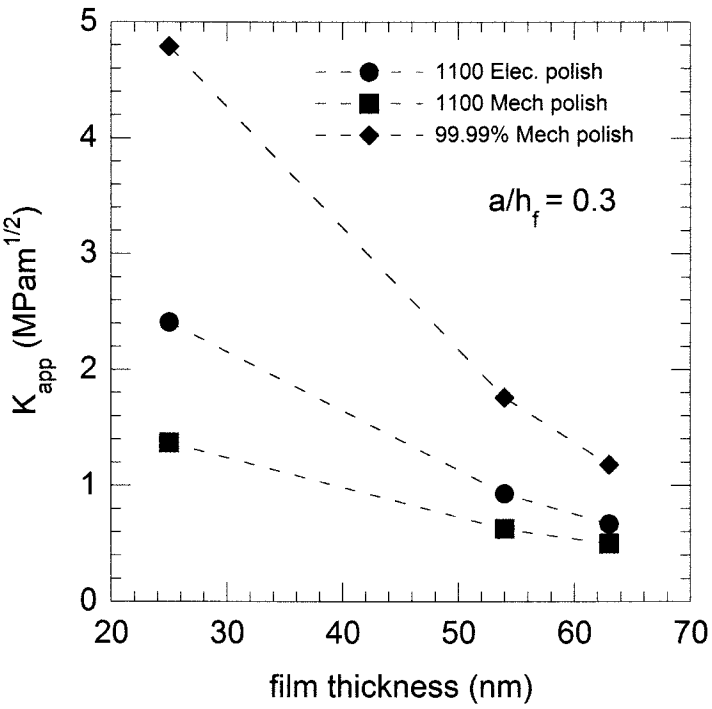

Figure 3.15 Applied stress intensity factor at fracture in the aluminum oxide – aluminum system assuming a constant normalized crack size of 0.3.

The surface crack size and orientation to the indent has a large effect on the applied stress intensity factor. The influence of the crack size was approximated by normalizing it to the film thickness. Figure 3-16 shows the relationship between the stress intensity factor for various substrates and crack sizes. For a given crack size to film thickness ratio the 99.99% mechanically polished aluminum substrate had the largest applied stress intensity factor and the 1100 mechanically polished substrate was found to have the smallest. The applied stress intensity at fracture for a crack length to film thickness ratio of 0.04 for the 54 nm thick film was 0.62, 0.32,

and 0.22 $MPam^{1/2}$ for the oxide film on the 99.99% pure, 1100 electropolished, and 1100 mechanically polished, respectively. As the ratio of crack size to film thickness increased to 0.30 the stress intensity increased to 1.76, 0.93, and 0.63 $MPam^{1/2}$ for the oxide film on the 99.99% pure, 1100 electropolished, and the 1100 mechanically polished substrates, respectively. These values for the stress intensity factor are reasonable for brittle ceramics.

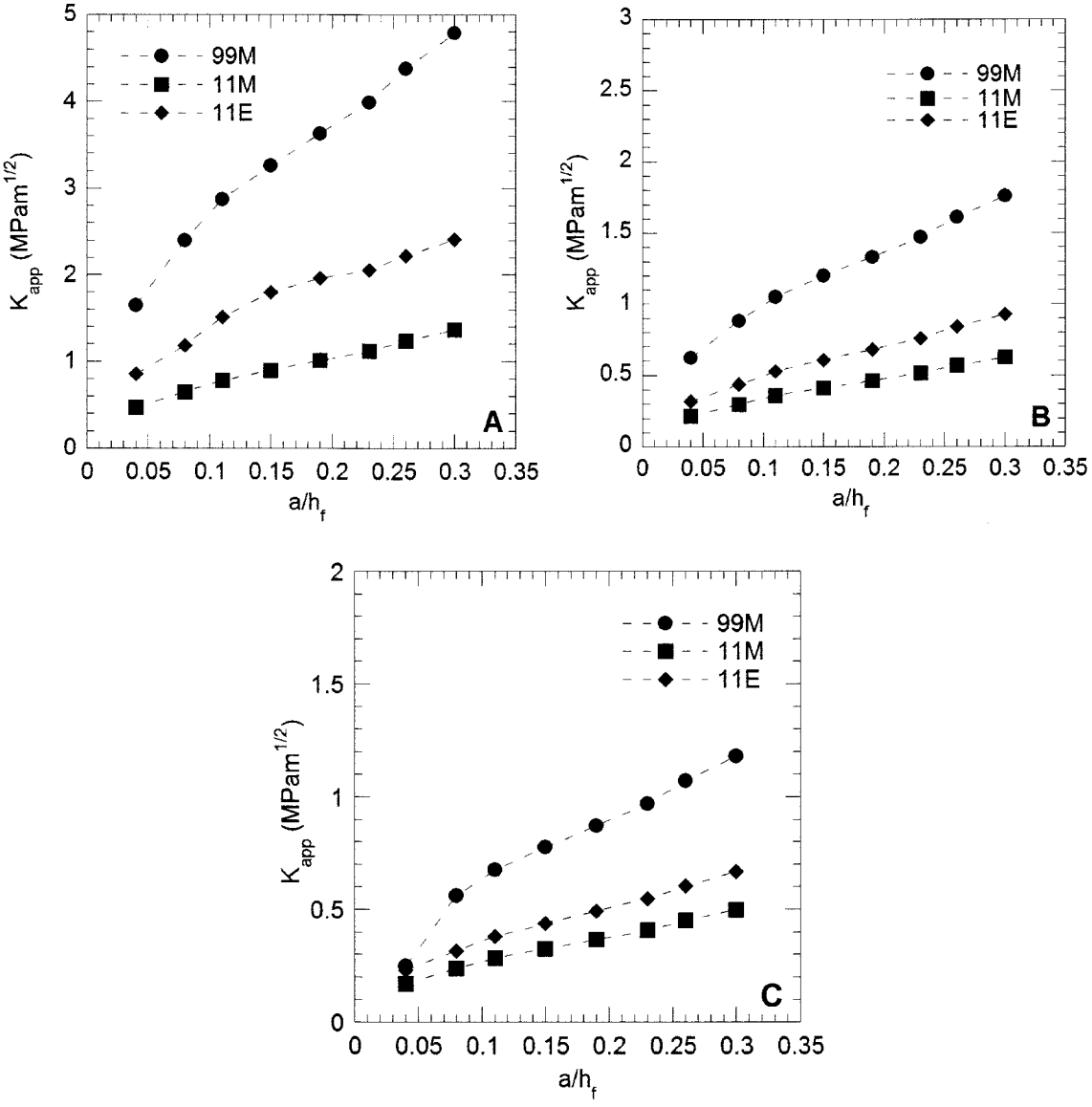

Figure 3.16 Applied stress intensity factor at fracture for various a/hf values for the a) 25 nm b) 54 nm and c) 63 nm thick films

In determining the critical parameters for film fracture, Chechenin *et al* considered the film as an elastic film on a yielding substrate and used the bending of circular clamped-edge plate with constant pressure acting from the substrate and a contact force from the indenter that increases towards the center. [1] This model is the same as the current study. However, Chechenin *et al* found that the film deflection was comparable to the film thickness. The bending moments were neglected and only considered the membrane force for failure. The current study showed that for this current system the film deflection was less than the film thickness and that the bending moments dominate the failure.

Weppelmann and Swain conducted a similar experiment using micro-indentation to determine a fracture criterion for hard films deposited on compliant substrates by physical vapor deposition. It was shown that film failure was caused by large tensile stresses in the surface region outside the contact radius. [12] The large tensile stress at the surface for thin films was proven by Chai and Lawn using finite element analysis. [13] The representative curves for mode I stress intensity factor against a/h_f showed the same trends as the current study. Mode II fracture was neglected due to the small shear stresses created during indentation.

4. Results from energy method to analyze through thickness thin film fracture

The hardness of the aluminum substrate and the grade II polycrystalline titanium were determined through nanoindentation with a maximum load of 900 μN and 6000μN, respectively. The average hardnesses for the aluminum and titanium substrates are 200 MPa and 2.41 GPa, respectively. The hardness values were calculated from 15 indents at various locations in the polycrystalline samples. No discontinuities were present on the load-depth curves for the both substrates. The yield stress can be estimated using Tabor's relationship between the hardness, H and yield stress, σ_y.

$$\sigma_y = \frac{H}{3} \tag{9}$$

The yield stress was determined to be 75 MPa and 800 MPa for the aluminum and titanium, respectively. A curve fit operation was then used to determine the loading profile of the titanium substrate. The loading curve follows a power law relationship and was curve fit using [20]

$$P_s = K\delta^n + C \tag{10}$$

where P_s is load applied to the substrate, K, n and C are empirical constants, and δ is the depth of penetration. The resulting load-depth curves from the indentations made into the anodized titanium showed discontinuities. The load-depth curves from the substrates did not contain any discontinuities. Two typical load-depth curves, one from the anodized titanium and one from the titanium without a film, can be seen in figure 4.1. The titanium sample without the film was shown to reach higher penetration depths at lower loads than the anodized sample. The load - depth curve for anodized titanium was clearly affected by the presence of titanium oxide on the surface.

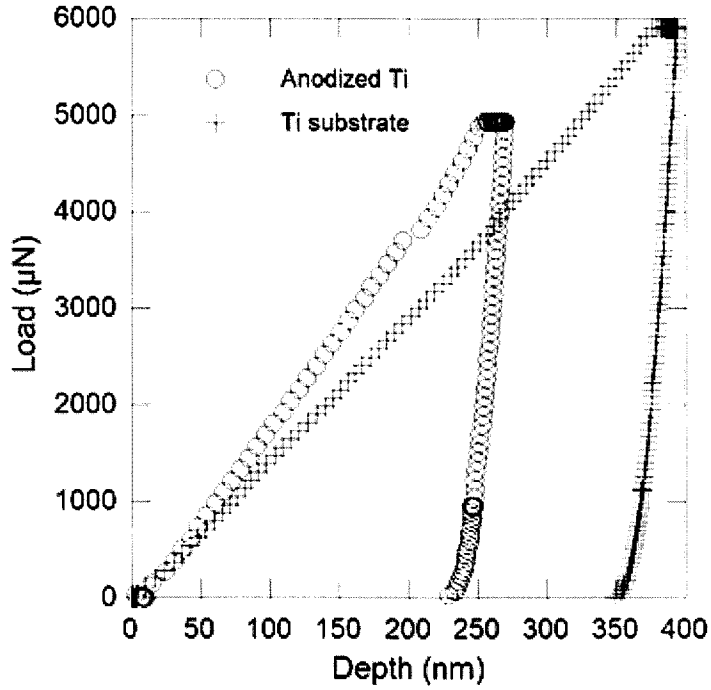

Figure 4.1 Load-depth results from indentations into grade II polycrystalline Ti with and without an anodized film

Nanoindentation was also performed on an anodized aluminum substrate, as discussed in section 3, using a tip with a larger radius (approximately 1 μm) and a film that is thicker than the thermally grown oxides, approximately 150 – 250 nm thick. A discontinuity at 8mN was caused from a circumferential crack that occurred outside of the tip contact radius. The circumferential crack around the indentation can be seen in figure 3-6. The contact radius is labeled as a_c and the radius of the circumferential crack is labeled as c. Circumferential cracks were not present around indentations made with a maximum load of 7mN. The anodized film was utilized to demonstrate the circumferential cracking because the film's surface was smooth compared to the thermally grown oxides.

The position of the through thickness cracks are located at the elastic-plastic boundary in the substrates. [54] The film covering the plastic region is allowed to deform. The film beyond the plastic zone is held in place during indentation. Estimation to the plastic zone radius under nanocontacts has been shown to be [55]

$$c = \sqrt{\frac{3P_s}{2\pi\sigma_y}} \tag{11}$$

where P_s is the load carried by the substrate at the time just prior to fracture and σ_y is the yield stress of the substrate. The radial plastic zone will result in circumferential cracking of the film outside the contact area of the tip. Scanning electron micrographs, which are shown in figure 3-13, show that the spherical model for the plastic zone radius is a good estimation to the location of the through thickness fracture of the oxide films. A schematic for the position of the through thickness crack can be seen in figure 4-2.

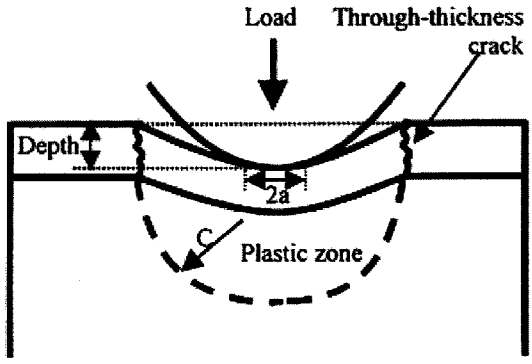

Figure 4.2 schematic of through thickness cracking of the thin film

Simple integration of the load-depth curves produced during indentation result in the energy that was put into the system. Integration of the load-depth curves, from the anodized film, until the onset of fracture (beginning of the discontinuity) will give the total energy applied, U.

$$U = \int_0^{\delta_c} P(\delta) d\delta \tag{12}$$

This includes energy participating in deformation of the substrate and film. The energy does not decipher between elastic or plastic deformation. The area of integration for the anodized film and titanium substrate is shown in figure 4-3.

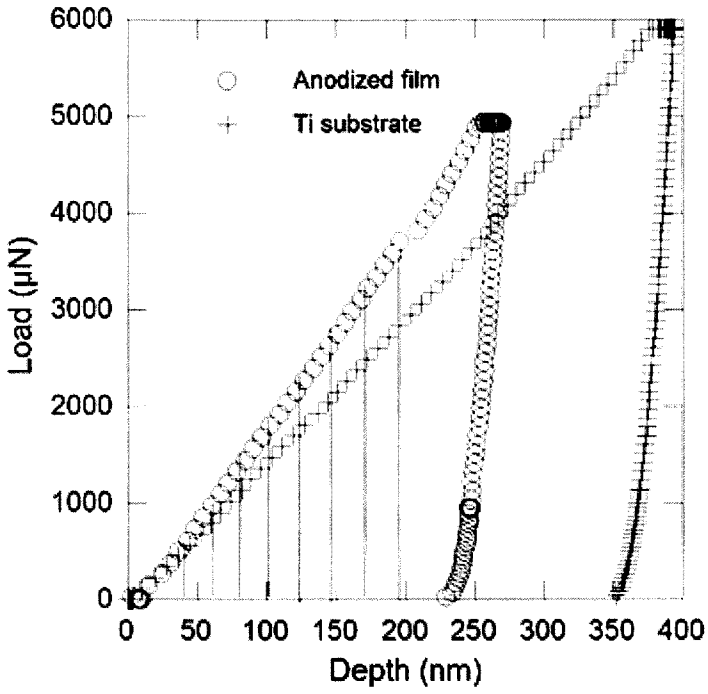

Figure 4.3 Energy applied to the system during indentation of the anodized titanium

The total energy put into the system is a superposition of the energy to fracture the film and the energy to plastically deform the substrate. An integration of the resulting load-depth curves from the titanium prior to anodizing gave estimation into the amount of energy needed to plastically deform the substrate. The integration was conducted until the critical depth at fracture occurred for the anodized titanium. The amount of energy needed to fracture the film, U_{film} can then be determined by subtracting the energy for plastic deformation of the substrate, $U_{substrate}$ from the

total energy applied to the system, U_{system}. The superposition of energies from the film and substrate can be seen in figure 4-4.

$$U_{film} = U_{system} - U_{substrate} \tag{13}$$

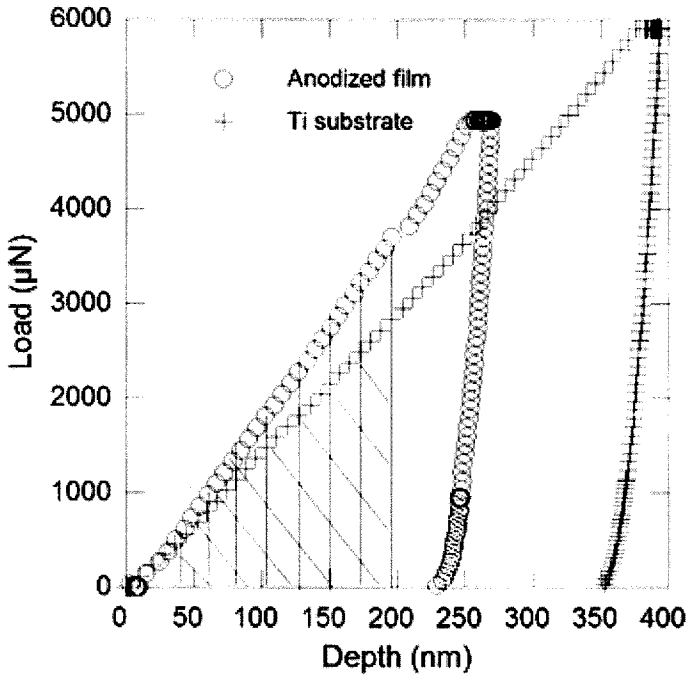

Figure 4.4 The energy to fracture the film determined by substracting the energy to deform the substrate from the entire system

The energy to fracture the titanium oxide films were shown to differ by an order of magnitude. The energy for fracture is dependent on the thickness of the film and the location of where the crack initiates. The energy is dependent on the new area produced from the formation and propagation of the crack. Table 3 summarizes the average energy needed for fracture for each film thickness and substrates.

The methods outlined by van der Varst *et al* [17] and Abdul-Baqi *et al* [18] to determine fracture energy was shown to be reasonable for thin films. The thermally grown oxide with a thickness of 63 nm on the electropolished aluminum substrate was found to have an average fracture energy of 0.070 pJ with a standard deviation of 0.061 pJ using the method outlined by van der Varst. The method outlined by Abdul-Baqi calculated an average fracture energy of

Table 3 Energy results for thermally grown oxides (TGO) on various aluminum substrates and an anodized titanium

Sample	h_f (nm)	U_{system} (pJ)	U_{film} (pJ)
1100Al Mech polish (TGO)	25	0.093 +- 0.032	0.052 +- 0.031
	54	0.133 +- 0.048	0.072 +- 0.017
	63	0.121 +- 0.074	0.079 +- 0.052
1100Al Electropolish (TGO)	25	0.073 +- 0.034	0.052 +- 0.024
	54	0.098 +- 0.018	0.066 +- 0.035
	63	0.103 +- 0.059	0.071 +- 0.033
99.99%Al Mech polish (TGO)	25	0.179 +- 0.105	0.122 +- 0.078
	54	0.260 +- 0.138	0.136 +- 0.095
	63	0.274 +- 0.188	0.104 +- 0.56
Anodized Titanium	250	249.7 +- 130 .1	74.69 +- 37.89

0.056 pJ with a standard deviation of 0.039 pJ. The method in the current work resulted in an average fracture energy of 0.071 pJ and a standard deviation of 0.033 for the same system. This similarity, which may at first be taken as encouraging, is likely more fortuitous than not, because the three methods (that described in Fig. 4-4, Abdul-Baqi, and that of van der Varst) are inherently different measurements of energy.

In thin film fracture, we will assume a crack is initiated and propagates completely through the thickness. It takes a certain amount of force to move the crack front. In thin film fracture a crack is initiated and propagates completely through the thickness. The surface area of the crack is the circumference of the crack multiplied by the thickness of the film. The energy can then normalized by the area of the crack. This will result in the crack extension force for the film. The equation for the crack extension force is

$$G = \frac{U_{film}}{4\pi c h_f} \tag{14}$$

where c is radius of plastic zone and h_f is the film thickness. The plastic zone radius was determined from the load applied to the substrate. The denominator is multiplied by 2 because there are two new surfaces being created during the crack extension. The equation for the crack extension force was modeled for a constant load condition for fracture. The crack extension force for the titanium oxide film is 19.75 J/m^2. The crack extension force for the different aluminum oxide thicknesses on various aluminum substrates and the anodized titanium is summarized in table 4. The elastic modulus used to calculate the stress intensity at fracture for the thermally grown aluminum oxide and anodized titanium oxide was 411 GPa and 180 GPa, respectively. This elastic modulus for the thermally grown aluminum oxide and titanium oxide is considered to be an upper bound because they were taken from their crystalline structures. The thermally grown oxide films may have an amorphous structure. Amorphous materials typically have lower elastic modulus than its crystalline form. The elastic modulus for the anodized aluminum was 140 GPa. [56]

Figure 4-5 shows the resulting crack extension force for the 25, 54, and 63 nm thick oxide films on the various aluminum substrates. Each point on the graph is an average of 10 indents randomly positioned on the sample. The standard deviation shows that there is some overlap in data from the 25 nm thick film to the 64 nm thick film. The standard deviation for the crack extension force, for a given film thickness, overlapped. This shows that no matter what substrate was used for the thermally grown aluminum the crack extension force was equivalent. Since it takes a critical amount of energy for a crack to propagate the crack extension force has to approach a critical value. From the data given a critical value for the crack extension force could not be deduced. The average crack extension force for the aluminum oxide ranged from 0.32 to

1.67 J/m^2 for the various thicknesses and substrates. The anodically grown aluminum oxide film was found to have a fracture energy of 0.31 J/m^2. Polycrystalline sapphire was shown to have fracture energies between 6 and 7.3 J/m^2. [57] The crack extension force for the 250 nm thick titanium oxide film was 19.8 J/m^2 with a standard deviation of 7.74 J/m^2. A general study of bulk titanium oxide fracture toughness measured a fracture energy of 68 J/m^2. [58]

Table 4 Calculated results for crack extension force (G) and stress intensity at frature (K_{app}) for the oxide films grown on various aluminum substrates and an anodized titanium

Sample	h_f (nm)	G (J/m^2)	K_{app} (MPam$^{1/2}$)
1100Al Mech polish (TGO)	25	0.96 +- 0.53	0.64 +- 0.16
	54	0.59 +- 0.14	0.51 +- 0.06
	63	0.56 +- 0.34	0.48 +- 0.15
1100Al Electropolish (TGO)	25	0.63 +- 0.30	0.52 +- 0.13
	54	0.34 +- 0.18	0.37 +- 0.12
	63	0.32 +- 0.09	0.38 +- 0.05
99.99%Al Mech polish (TGO)	25	1.67 +- 0.95	0.83 +- 0.25
	54	0.74 +- 0.49	0.55 +- 0.20
	63	0.49 +- 0.40	0.45 +- 0.14
Anodized Titanium oxide	200	19.8 +- 7.74	2.51 +- 0.51
Anodized Aluminum oxide	200	0.31 +- 0.03	0.22 +- 0.01

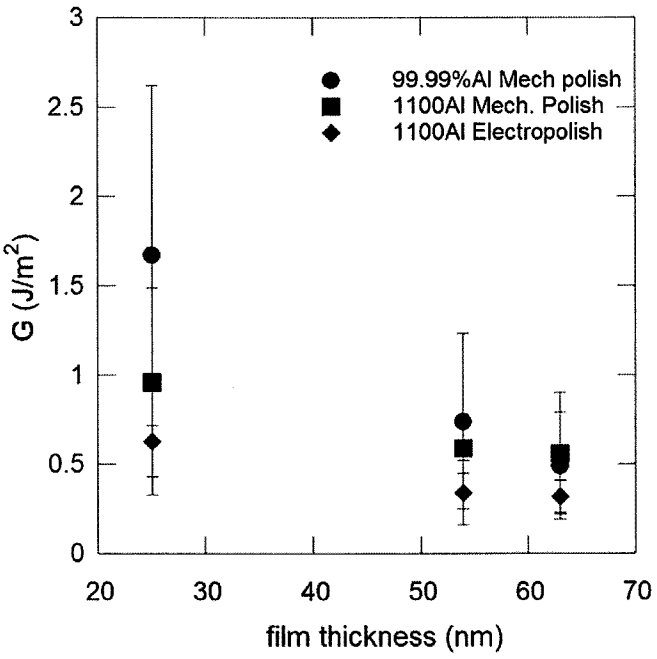

Figure 4.5 Resulting crack extension forces from 25, 54, and 63 nm thick oxide films on various aluminum substrates

The crack extension force is the fracture criterion from an energy basis. There is a correlation between the energy method and the stress intensity method. It is reasonable to assume the thin films are in a state of plane stress. The correlation between the crack extension force and stress intensity, for plane stress, is

$$K = \sqrt{GE} \tag{15}$$

where E is the plane strain elastic modulus of the film. The elastic modulus of titanium oxide thin films was shown to vary between 65 GPa and 147 GPa for films produced by reactive evaporation and ion plating, respectively. [59] The elastic modulus for sintered polycrystalline plates of titanium dioxide is on the order of 185 GPa and rutile varied between 120 GPa and 480 GPa, depending on crystal orientation. [60,61] An elastic modulus of 180 GPa was chosen for the anodically grown titanium oxide thin film. This gives two different methods for determining fracture. The stress intensity at fracture could be related back to the stress applied to the film and the size of a critical flaw. Table 3 summarizes the applied stress intensity at fracture calculated

from the crack extension force. Figure 4-6 illustrates the applied stress intensity at fracture for the varying aluminum oxide thicknesses and aluminum substrates.

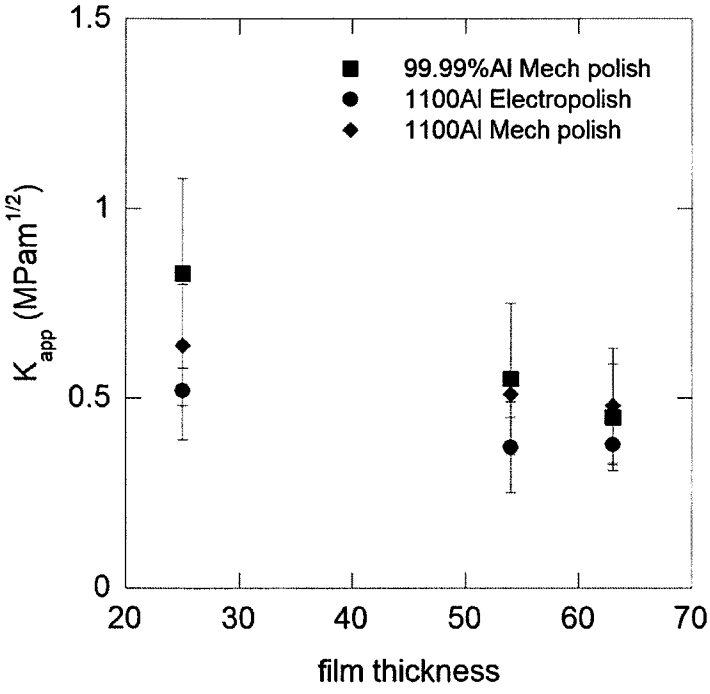

Figure 4.6 Resulting stress intensity values at fracture for 25, 54, and 63 nm thick oxide films on various aluminum substrates

Similar to the crack extension force the results for the applied stress intensity show that standard deviation from the average overlap no matter what the thickness of the oxide or substrate that the film was grown on. The asymptotic behavior for the stress intensity at fracture as the film increases from the energy approach (figure 4-6) is similar to the graph of the stress intensity at fracture from the plate bending approach where the ratio of defect size to film thickness was held constant (Figure 3-16). This shows that the critical defect size in the thermally grown oxides increased with increasing film thickness. As the crack extension force has a critical value there is a critical value for the applied stress intensity for a crack to propagate. The stress intensity from the crack extension force calculations for the aluminum oxide thin film was between of 0.37 and 0.83 MPa-m$^{1/2}$. The anodically grown aluminum oxide was 0.22 MPa-m$^{1/2}$ with a standard deviation of 0.01. Single crystal sapphire has been shown

using a controlled flaw fracture test to have fracture toughness values from 2.43 to 4.54 MPa-$m^{1/2}$ depending on the plane and crystallographic direction the test was administered. [62] These values were obtained using a double cantilever beam fracture test in a nitrogen atmosphere. Fracture testing of single crystal sapphire using indentation has shown that it has fracture toughness between 1.89 and 2.55 MPa-$m^{1/2}$. [63] The titanium oxide film was shown to have a stress intensity of 2.51 MPa-$m^{1/2}$ with a standard deviation of 0.51 MPa-$m^{1/2}$. A general study of bulk titanium oxide fracture determined the fracture toughness to be 6.1 MPa-$m^{1/2}$. [58] The fracture energies and applied stress intensity at fracture for the aluminum oxide and titanium oxide thin films were comparable to the bulk properties. The properties for the thin films were slightly lower than the bulk properties.

5. Results from slip step analysis

Indentations were made into several grains of different orientations with a sharp 90 degree conical tip, a very blunt 90 degree conical tip which behaves more similarly to a spherical tip and, in some cases, with a standard Vickers tip. Most indentations were made in 21-6-9 stainless steel, however some comparisons are made to indentations in nickel.

5.1 Increasing Load

Indentations made into a grain with a surface orientation of (0 1 8) are shown in Figure 5. 1 for loads ranging from 5mN to 500mN. For maximum loads of 25mN and up the pattern formed from the slip steps appears to change very little. The two lowest loads appear somewhat different, however it is beginning to take on the same general form as the others. The effects of tip geometry and surface orientation will be addressed in following sections.

5.2Growth of the Plastic Zone

Two different sets of experiments contribute evidence that slip steps propagate outward with the plastic zone boundary, such that a step formed will only continue to grow for a finite period and will then cease.

Figure 5. 2 (a) shows an error signal AFM image of a 100g Vickers indentation in nickel. Slip steps appear to begin immediately at the edge of the indentation impression. In reality these

steps were most likely formed during earlier stages of indentation. They ultimately end up at the very edge of the indentation only after the tip continued to penetrate deeper into the sample. As the depth continued to increase, the edge of the indenter overlapped into the pile up material and consumed the prior slip steps. The specimen was then briefly polished to remove the pile up material and regain a flat surface, but not so much as to remove the residual indentation impression. The Vickers tip was then carefully realigned with the impression and loaded to 200g. Figure 5. 2 (b) is an error signal AFM image of this same indentation after being reloaded. It can be seen that all of the slip steps further from the indentation were reactivated, however near the edge of the indentation fewer slip steps continued to grow.

Similar results have also been observed by repeating this procedure in 316 stainless steel. Figure 5. 3 shows two such examples of this. Both of these indentations are near grain boundaries due to the smaller grain size of the material used. For this reason the step patterns are not as regular as those in Figure 5. 2, however the decreased number of slip steps reactivated near the edge of the indentation can still be observed.

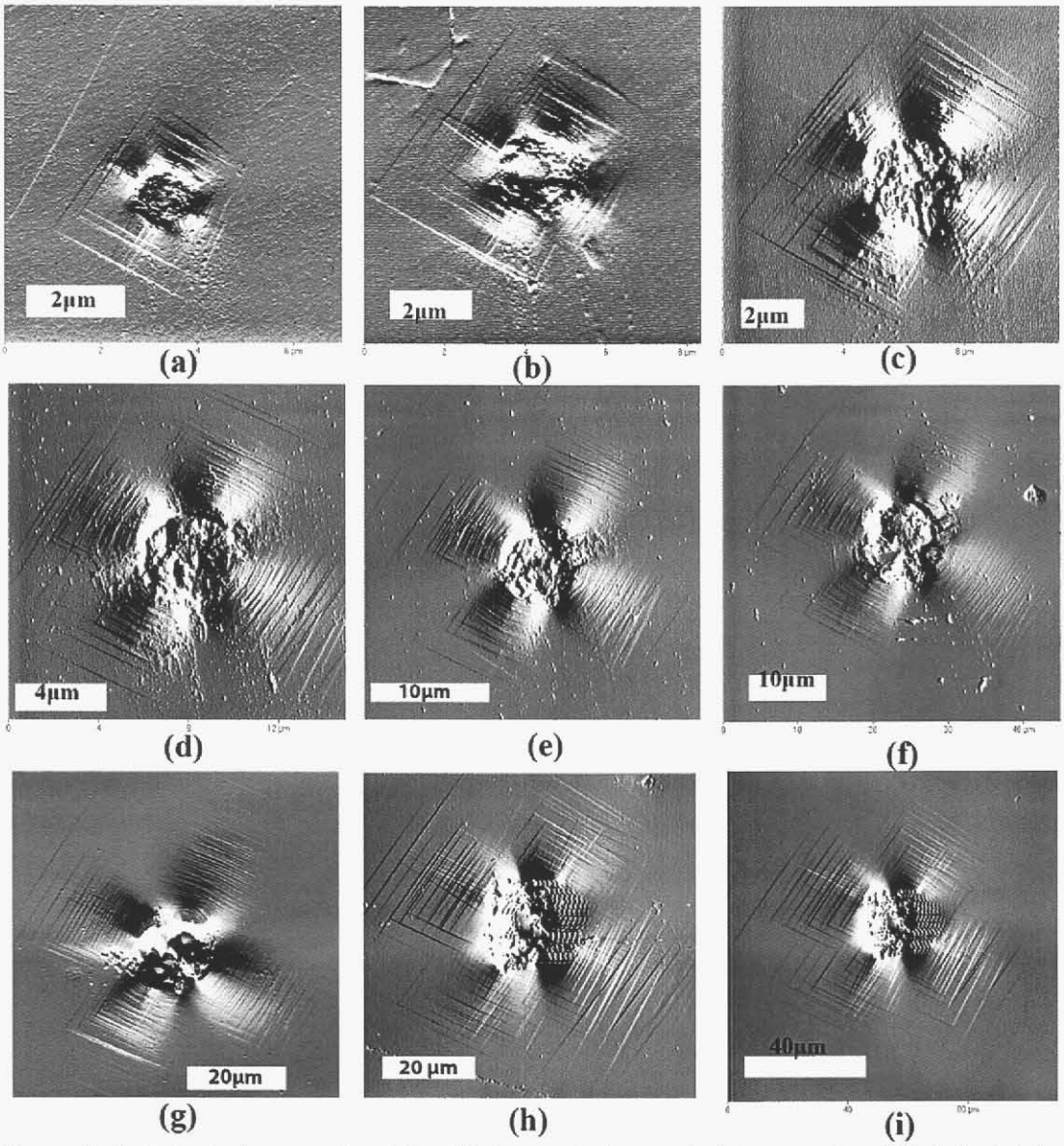

Figure 5. 1 Indentations made with a 90 degree indenter tip into a grain of 21-6-9 stainless steel with surface orientation (0 1 8) to max loads of (a) 5mN, (b) 10mN, (c) 25mN, (d) 50mN, (e) 100mN, (f) 250mN, and (g) 500mN. Indentations in the same grain made with a blunter tip are also shown to (h) 500mN and (i) 1000mN.

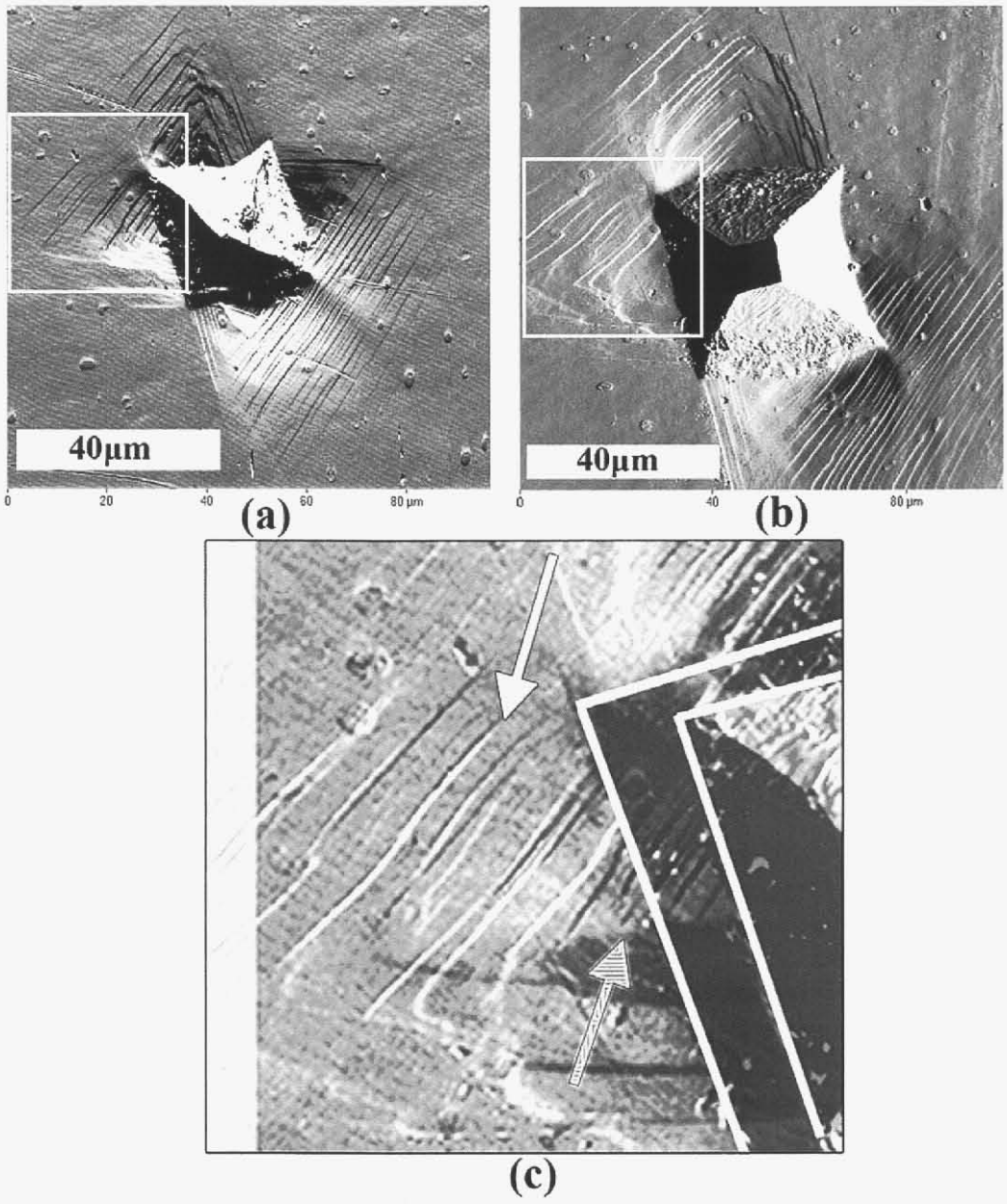

Figure 5. 2 An error signal AFM image of a 100g (a) Vickers indentation shows slip steps immediately next to the indentation. The specimen was polished to remove the pile up material and slip steps only, then the indentation was enlarged at a load of 200g (b). The region from within the boxes are overlaid in (c) where the white steps are from (b) and the black steps are from (a). Steps further away from the indentation line up indicating that the same steps continued to grow during the second loading as indicated by the white arrow. The hashed arrow points to steps near the indentation which formed during the first loading, but did not continue to grow during the second loading. The white lines outline the edges of both indentation impressions.

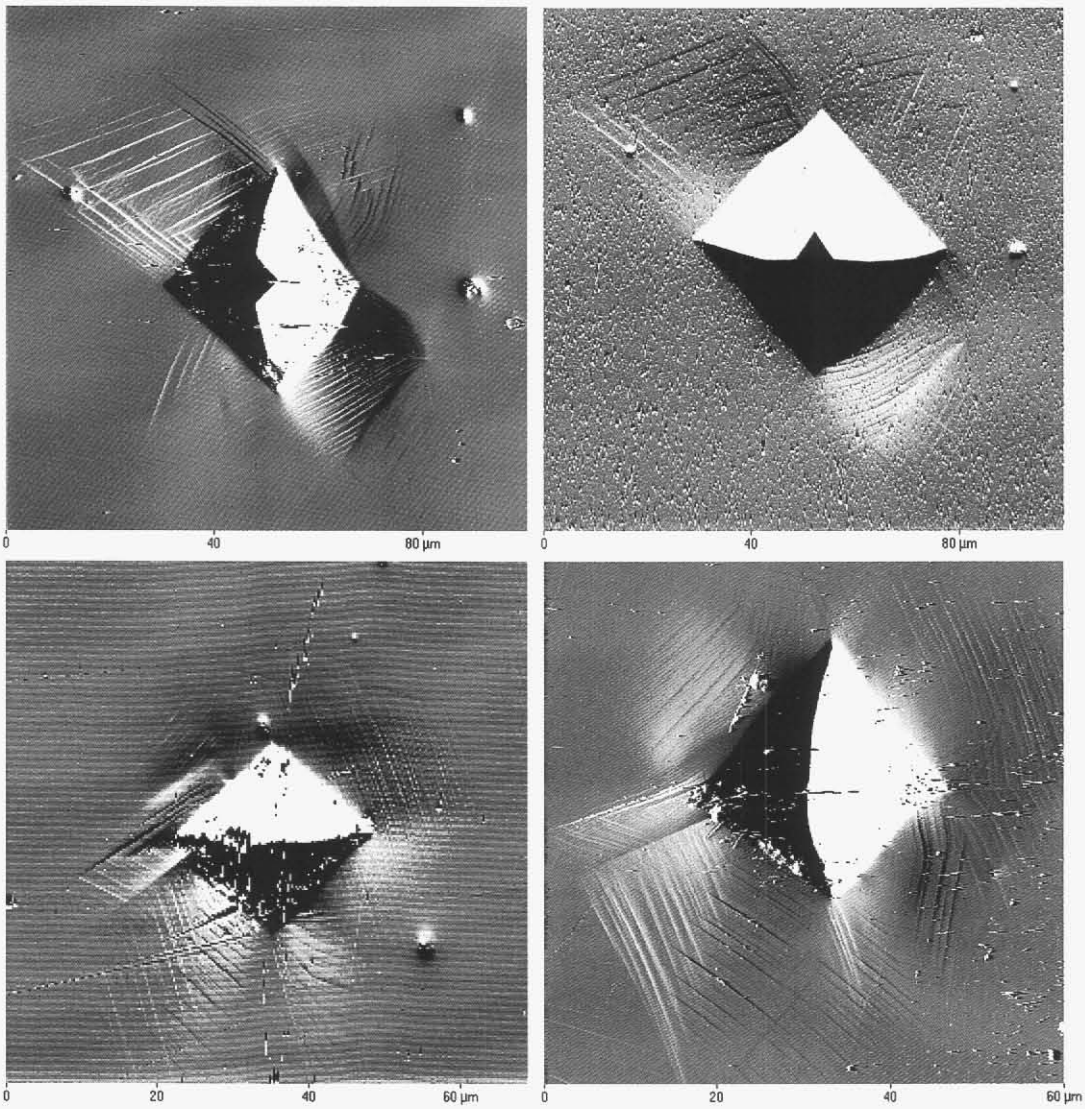

Figure 5. 3 Error signal AFM images of indentation into 316 stainless. (a) 200g indentation was made and then polished flat and enlarged to (b) 300g. In a different grain a 50g indentation (c) was made, then polished flat and enlarged to 100g (d).

A second experiment which provides evidence that slip steps near the indentation cease to grow after the plastic zone expands beyond a certain point involved measuring the height and spacing of slip steps immediately next to indentations of various loads in stainless steel. In the region near the edge of the indentation, the height and spacing of slip steps was found to be relatively constant over a range of indentation depths.

Figure 5. 4 (a) and (b) shows indentations made with a sharp 90° conical tip at 20mN and 500mN peak loads into a grain with a surface orientation of (13 11 18) in 21-6-9 stainless steel.

Figure 5. 4 (c) shows cross section plots taken from 2μm scans just beyond the left edge of the indentation. The average step height and spacing was calculated from these sections using the procedure described in Chapter 5. For the 500mN indentation, the average step height was measured to be 7.1 nm and the average spacing was 88μm. The 20mN indentation was measured to have an average step height of 5.6nm and average spacing of 90μm. The small increase in step height from 20mN to 500mN loads could be a result of a small amount of additional step growth with increasing load. However, measurements were also made from a 250mN indentation in this same grain and the average height was found to be 4.8nm with an average spacing of 86μm. This indicates that the variation in step height is within the bounds of experimental error and should not be related to changes in peak load.

5.3 Effect of Surface Orientation

Indentations were made into multiple grains with different surface orientations to observe the effects of crystal orientation on the slip step patterns formed. Patterns were observed in polycrystalline stainless steel and nickel for various grains, particularly with orientations near {001}, {011} and {111} as well as for a (111) single crystal of nickel.

Figure 5. 5 shows indentations made into five different surface orientations: (a) (1 2 30), (b) (0 1 8), (c) (8 5 2), (d) nickel (111), (e and f) (13 11 18). Slip step patterns in the (1 2 30) orientation behaves nearly the same as would be expected from a perfect (001). Four distinct regions of pile up occur and each contain slip steps from a different {111} slip plane. All of the slip steps result from the positively inclined slip planes. When the surface rotates a bit further away from (001), such as with the (0 1 8) orientation, there still remain four distinct pile up lobes. However, two of them (those to the upper and lower left sides in Figure 5. 5 (b)) contain slip steps from only the positively inclined slip plane, while the other two lobes of pile up contain slip steps from both the positively and negatively inclined slip planes.

The (8 5 2) orientation behaves similarly to a (110) surface. The indentation shown in Figure 5. 5 (c) has a slip step pattern consisting of long, parallel slip steps on both sides of the indentation. These steps all belong to the same set of parallel slip planes meaning that the positively inclined slip plane is active on one side of the indentation while the negatively inclined slip plane is active on the other. The discontinuity of these steps near their middle is an indication that while all are on the same set of slip planes, they do not likely all have the same

Burgers vector. The steps join up with bounding steps on either side and the active Burgers vector is likely the one which is shared with the bounding steps.

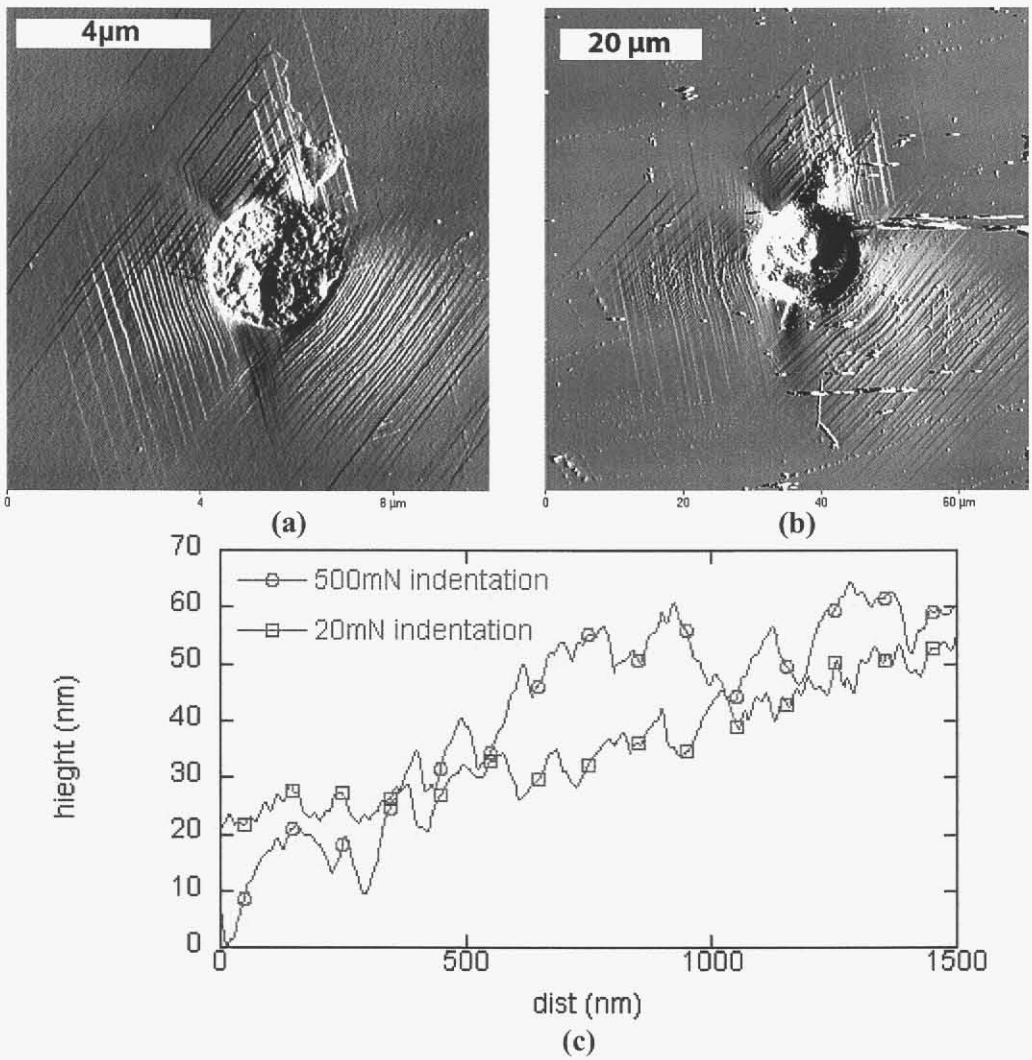

Figure 5. 4 Cross section plot (c) of slip steps very near the left side edge of a 20mN (a) and 500mN (b) indentation made into the same grain show that the height and spacing of the steps are very similar even for indentations of significantly different depths.

Figure 5. 5 (d) is an indentation made into a (111) single crystal of nickel. This was used to show the perfect symmetry found when indentations are made into a perfect (111) surface and this study was never successful in finding a grain within the polycrystalline samples which had an orientation very close to (111). This pattern shows parallel slip steps from each of the three other {111} slip planes. Similar to the (8 5 2), they are bound on either side by bounding steps

and are discontinuous at their middle. Again this is believed to be the result of different Burgers vectors acting on either side.

Figure 5. 5 (e) shows an indentation into 21-6-9 stainless steel with a surface orientation of (13 11 18). The slip steps to the upper and left side of the indentation form in a pattern consistent with that seen by the perfect (111) surface seen in Figure 5. 5 (d), however they do not form symmetrically around the indentation. Figure 5. 5 (f) is an AFM topography image of the same scan shown in (e) which clearly shows that pile up is very asymmetrical and constrained only to the upper and left sides where most of the slip steps occur. It should be pointed out that the bright region immediately to the right of the indentation that looks to be a region of pile up is not. Rather, the observed height here is an artifact resulting from hysteresis in the piezoelectric AFM scanner tube. As a large voltage change is applied to move the tip deep into the indentation and then back to the surface, residual voltage remains in the scanner and it does not accurately find the surface.

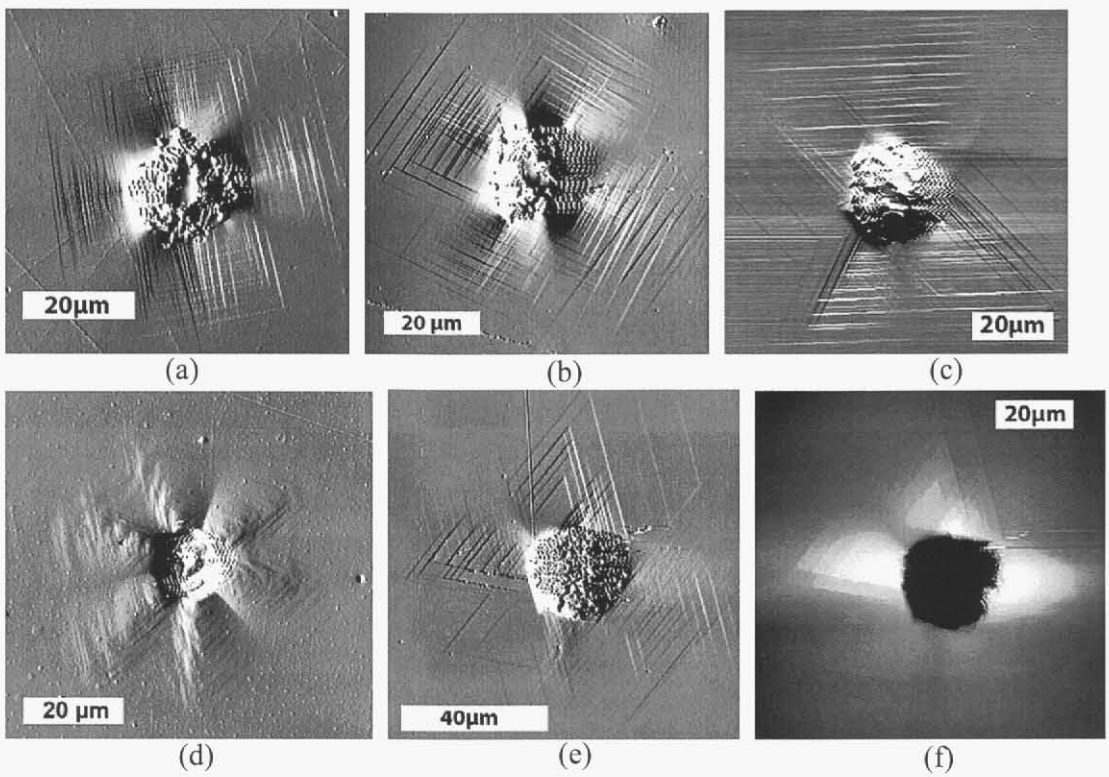

Figure 5. 5 Indentations made into surfaces of various orientations: (a) (1 2 30); (b) (0 1 8); (c) (8 5 2); (d) nickel (111); (e) (13 11 18) and (f) topography image of indentation shown in (e).

5.4 Effect of Tip Geometry/Orientation

Three different tips were used in these experiments. Two different tips were used which are nominally 90 degree conical tips. One has a tip radius of 1-2μm and will be referred to as the sharp tip. The other has not been well characterized, but is known to be quite blunt with a radius likely greater than 10μm and will be referred to as the blunt tip.

The third tip used was a standard Vickers four sided pyramid indenter tip.

There are distinct differences between the slip steps patterns which result from the sharp and blunt tips. Figure 5. 6 (a) and (b) show the result of indentation made with the (a) sharp and (b) blunt tips into a (0 1 8) oriented surface. The sharper tip produces more pile up and slip steps are spaced much closer together. Figure 5. 6 (c) and (d) shows Vickers indentations in this same grain with (0 1 8) orientation. In Figure 5. 6 (d) the tip was rotated 45° about the loading axis with respect to that shown in Figure 5. 6 (c). Figure 5. 6 (c) shows a "sharp" orientation for the tip where the faces of the pyramid are aligned parallel with the {111} slip planes. This results in slip step patterns which appear similar to those which result from the sharp conical tip. Likewise, the Vickers tip appears to also have a "blunt" orientation, shown in Figure 5. 6 (d), which results when the faces of the tip are not aligned parallel with the {111} planes. This orientation produces slip step patterns which appear similar to those produced by the blunt conical tip. Figure 5. 6 (e) shows a sharp tip indentation into a grain with surface orientation of (13 11 18) and (f) shows an indentation made in this same grain with the blunt tip. The blunt tip produced only a small amount of pile up, which occurs on the positively inclined slip planes and its bounding planes. The sharp tip results in only a small amount of additional growth of those steps, but adds a significant increase to the total amount of pile up via closely spaced steps on the negatively inclined planes to the left of and below the indentation as shown in Figure 5. 6 (e).

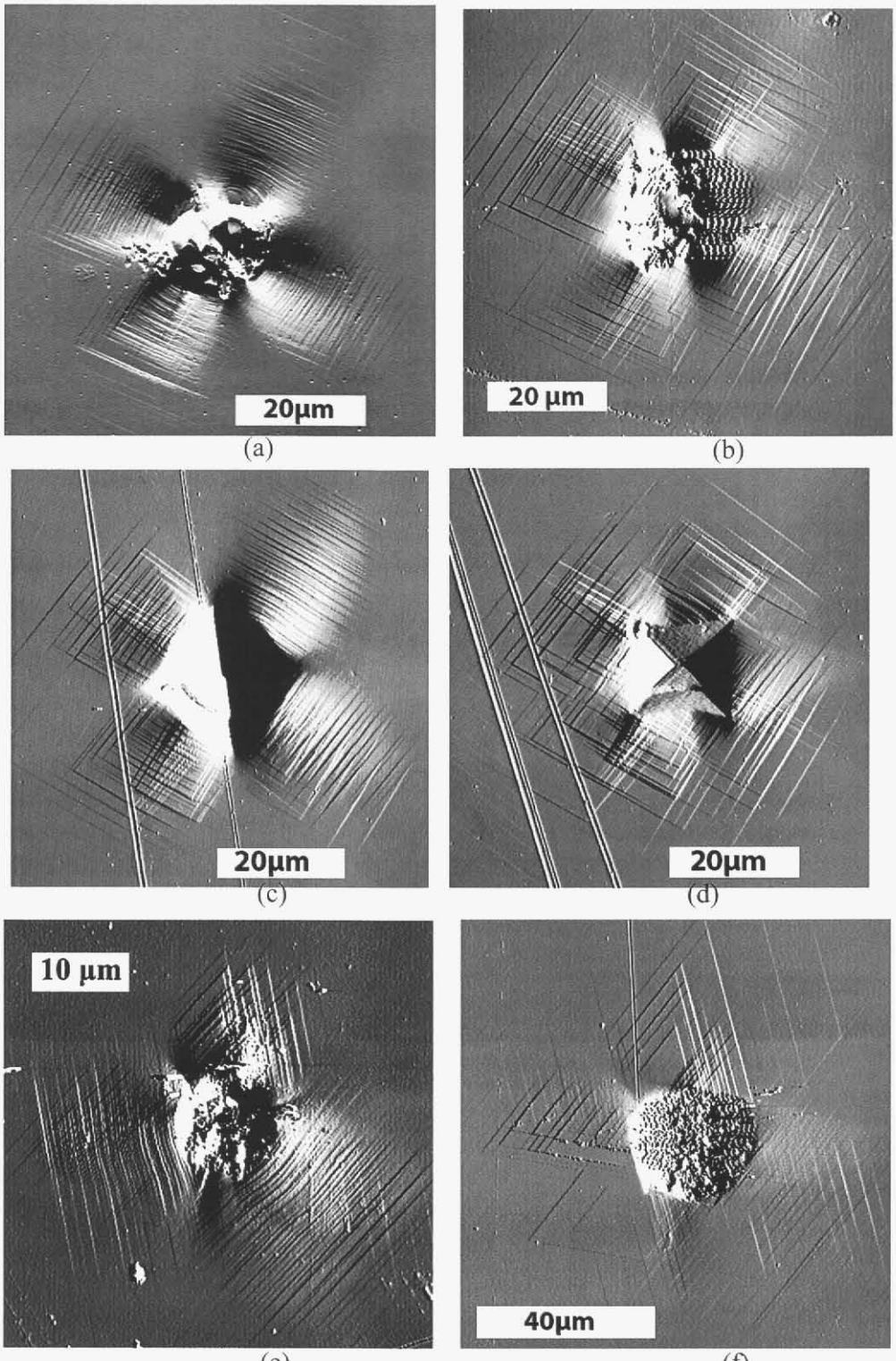

Figure 5. 6 Slip steps patterns which result from (a) sharp tip and (b) blunt tip in (0 1 8) surface orientation, as well as Vickers indentations oriented at 45° rotations, and sharp tip (e) and blunt tip (f) indentation into a surface with (13 11 18) orientation.

5.5 Slip steps across grain boundaries

Similarly to the experiments described in Chapter 4, blunt tip indentations were made near the grain boundary in grains adjacent to the (0 1 8) grain.

Figure 5. 7 shows optical microscopy images of indentation made across grain boundaries on either side of the (0 1 8) grain as well as an indentation made entirely within this grain for comparison. All three images were made with the sample oriented the same way and the optical images have been flipped to match with the AFM image. As described previously in section 6.2.2, the slip steps to the upper left of the indentation in

Figure 5. 7 (c) result from a single set of slip planes whereas those to the lower right result from two different sets of slip planes.

Figure 5. 7 (a) and (b) show that this same step pattern still formed in the (0 1 8) grain even when the grain boundary is present.

5.6 Discussion of Results of slip step analysis

Each of these observations contribute to an overall mechanistic understanding of the deformation taking place during an indentation test. This section will first look at the elastic stress state around an indentation which has been developed by other authors and compare it with experimental results. The transition from elastic to plastic deformation and the resulting pile up will then be addressed. Finally, necessary requirements will be inferred for the stresses acting during pile up which result in the slip steps observed for different experimental conditions.

5.6.1 Contribution of Elastic Stresses

At the initial onset of plasticity in any indentation process the only strains present are due to the elastic stresses. These strains are all downward into the bulk of the material and do not contribute to out-of-plane deformation, or pile up. Out of plane deformation occurs only after the plastic zone has grown to a point at which the elastic expansion of the surrounding material can no longer accommodate the displaced volume of the indentation [19].

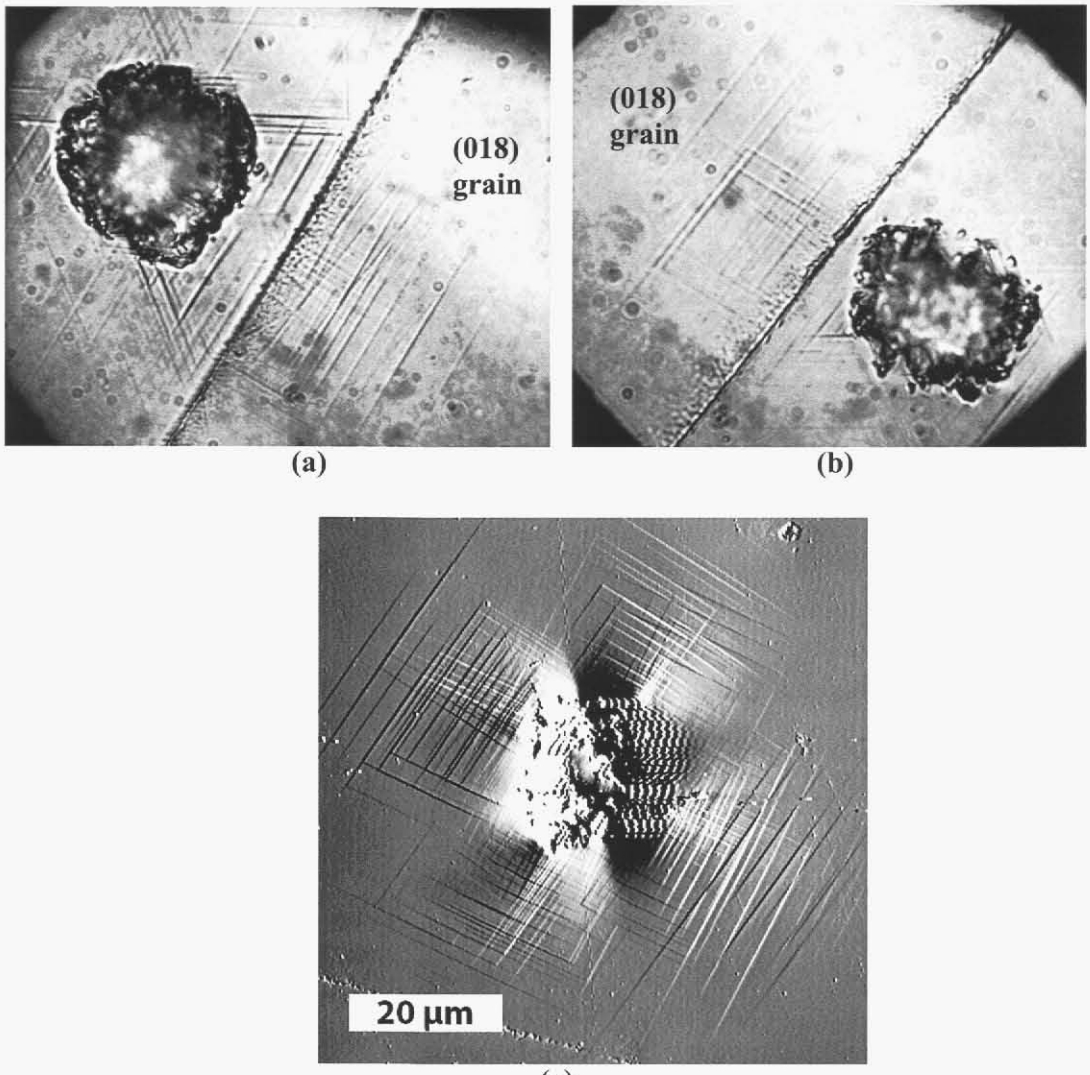

(a) (b)

(c)

Figure 5. 7 Indentations made in grains adjacent to the (018) grain, (a) and (b), produce slip patterns across the grain boundary which match those produced by an indentation entirely within the (018) grain (c).

These elastic stresses present during the early stages of indentation can be estimated as the elastic stresses due to a concentrated normal force. Using cylindrical coordinates with the axis of indentation in the z direction these stresses are [19]:

$$\sigma_r = \frac{P}{2\pi}\left\{(1-2\upsilon)\left(\frac{1}{r^2}-\frac{z}{\rho r^2}\right)-\frac{3zr^2}{\rho^5}\right\} \tag{16}$$

$$\sigma_\theta = -\frac{P}{2\pi}(1-2\upsilon)\left(\frac{1}{r^2} - \frac{z}{\rho r^2} - \frac{z}{\rho^3}\right) \tag{17}$$

$$\sigma_z = -\frac{3P}{2\pi}\frac{z^3}{\rho^5} \tag{18}$$

$$\tau_{rz} = -\frac{3P}{2\pi}\frac{rz^2}{\rho^5} \tag{19}$$

where P is the concentrated point force, r and z are the positions in the radial and axial directions, respectively and

$$\rho = \sqrt{r^2 + z^2} \tag{20}$$

σ_z and τ_{rz} can be combined into a resultant stress, Σ, which will remain constant along a spherical surface beneath the loading and will always act in a direction pointing toward the point load as shown in

Figure 5. 8 such that

$$\Sigma = \left(\sigma_z{}^2 + \tau_{rz}{}^2\right)^{1/2} = \frac{3P}{2\pi d^2} = \textbf{\textit{constant}} \tag{21}$$

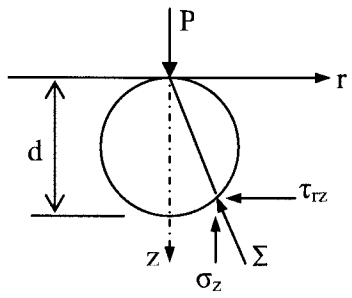

Figure 5. 8 The elastic stresses resulting from a concentrated load produce a normal stress in the z direction and a shear component which can be combined to produce a normal stress Σ, which will be constant along a sphere of radius, d, and always points in a direction toward the point of application of the load. The radial and tangential stress components will act in addition and are not shown in this figure.

These stresses can be resolved on slip planes using Schmid's law as shown in Figure 5. 9. Parallel slip planes on either side of the indentation and inclined at an angle φ to the surface will be subjected to a radially symmetric stress state such that the normal stresses will be equal, but the shear stress component will have opposite sign. The resolved shear stress will therefore not be equal at different points around the indentation. Figure 5. 10 plots the resolved shear stress evaluated at a position, such that $r=z$, as a function of the angle (φ) between a slip plane and the surface plane for slip planes with any angle between 0 and 90° for both positively and negatively inclined slip planes. At an inclination of 45°, τ_{rz} has no resolved component and so the total resolved stress resulting from σ_r and σ_z will be the same on both planes. For angles greater than 45° the slip plane with negative inclination will have the higher resolved shear stress and for angles less than 45° the slip plane with positive inclination will have the greater resolved shear stress.

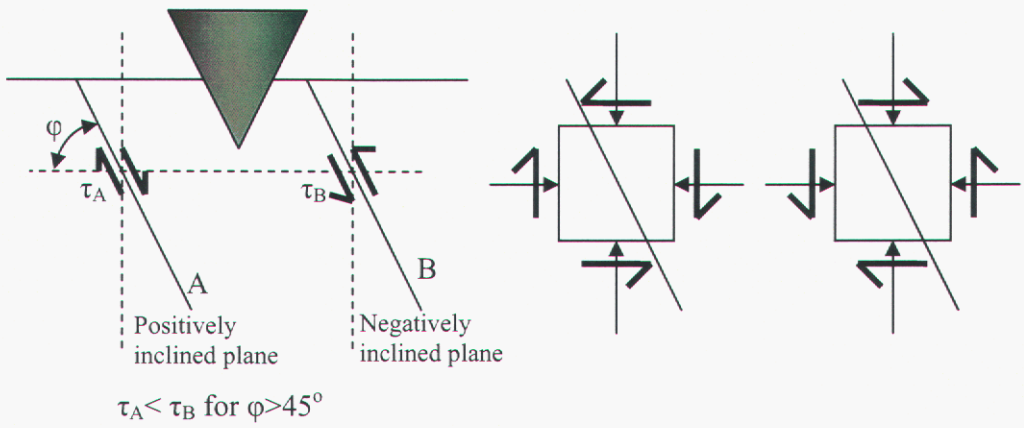

Figure 5. 9 The elastic stresses from a point loading will produce an axisymetric stress field such that parallel slip planes on either side of an indentation will experience the same normal stresses, but the shear component will have the opposite sign. The result of this is that when the plane is inclined at an angle greater than 45° with respect to the surface, the negatively inclined slip plane will have a larger resolved shear stress, while the positively inclined plane will have a larger resolved stress in the inclination is less that 45°.

During the initial stages of indentation, the elastic strains as well as the plastic flow is in a direction down into the bulk. The elastically expanding bulk must then exert outward compressive stresses which ultimately are responsible for the upward flow of material which creates the out of plane deformation on the surface. The stresses which act on the plastically

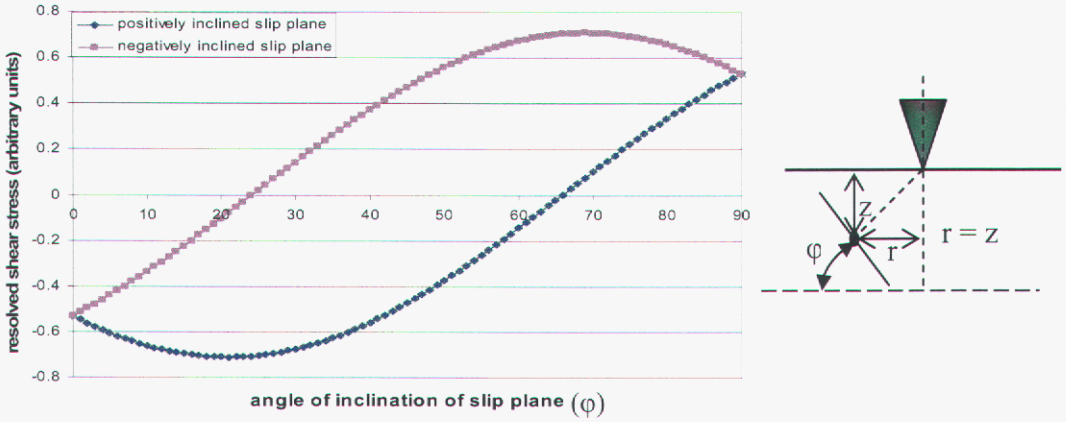

Figure 5. 10 The resolved shear stress acting on a slip plane is plotted in arbitrary units for planes inclined at an angle φ with respect to the surface. The plot is evaluated for any point where $r = z$ and the actual magnitude of the resolved stress will decrease with the distance from the point of loading and increase with applied load. The top curve represents the stress on a positively inclined plane whereas the lower is the stress on a negatively inclined slip plane.

deforming material and displace it up and out at the free surface involve both the contact stresses of the indenter pushing into the material as well as the stresses exerted out from the compressed material around the indentation. Contact mechanics calculations of the stresses around indentation often eliminate this difficulty by considering only elastic deformation or by considering the deforming material to be perfectly plastic.

When little or no pile up occurs around an indentation these calculations for the elastic stresses around an indentation may be appropriate for predicting where slip steps will occur. In work done by Kadijk et al [23], slip steps are observed inside the residual impression left from indentations made using a spherical tip in MnZn ferrite. The steps accommodate the downward displacement of material in the impression, as can be seen in Figure 5. 11. These slip steps are very different than those shown in the observations of section 6.2 all of which accommodate the upward flow of material pile up. There is little or no pile up visible and the elastic stresses described by equations 16-20 can be used to describe this type of behavior.

Berkovich indentations have been examined in MgO by Tromas et al and slip lines have been noted extending along the surface away from the indentations as shown in Figure 5. 12 [24]. These steps appear very different than those presented by Kadijk, which were confined within the impression, however they are still quite similar. The schematic in Figure 5. 12(b)

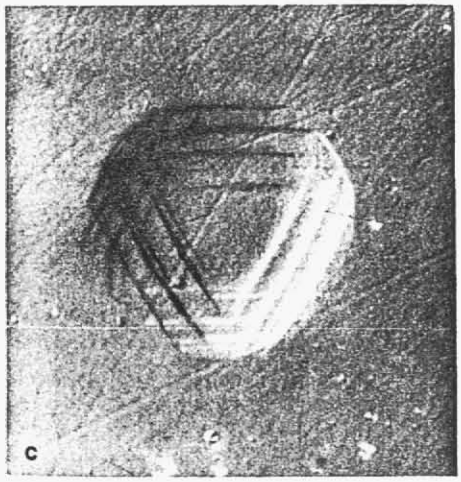

Figure 5. 11 10N indentation made with 0.25mm ball into (111) MnZn Ferrite surface. The visible slip steps are inside the impression and accommodate the downward displacement of the indenter, not the upward flow of pile up. The indentation is approximately 60μm across. (S. E. Kadijk and A. Broese Van Groenou *Acta. Metall.,* Vol. 37, No. 10, (1989) p. 2627.)

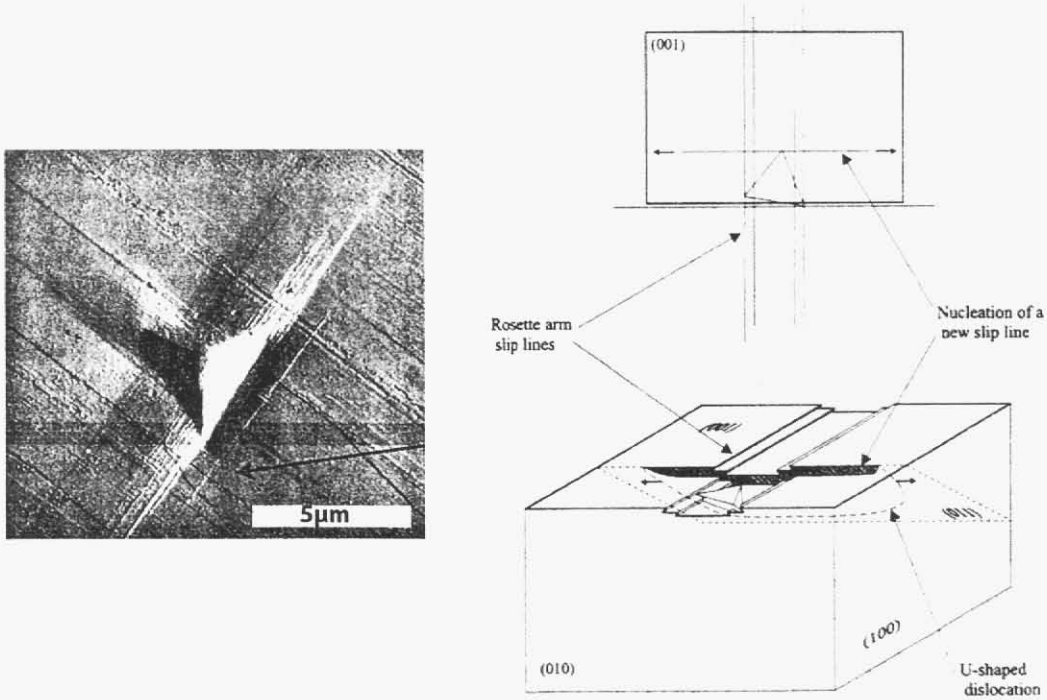

Figure 5. 12 A 67mN indentation into a (001) cleave surface of MgO developed slip lines in a rosette pattern. The schematic shows demonstrates that these steps contribute to downward strains around the indentation and are not producing material pile up. (Figures reproduced from reference [24])

demonstrates that the steps still accommodate downward material flow. Other authors have observed this type of rosette pattern of either slip steps or dislocation etch pits around indentations [64-66]. While these rosette patterns are important and worth study, it is important to note that they do not seem to directly contribute to pile up and it must therefore be understand that their formation occurs due to a different phenomenon than that which causes the slip steps in regions of material pile up.

5.6.2 Indentations with Pile up

The observations of section 5.1.2 clearly indicate that the slip steps visible on the surface around indentations in materials that pile up are either the result of, or result from, the pile up. If pile up occurs as a result of the sub-surface strain exceeding that which elastic expansion can accommodate, then downward flow should precede the pile up. This cannot be tested simply be comparing indentations made at different loads, because the strains from self-similar indenter tips are determined by tip geometry rather than the downward displacement of the tip.

Therefore it is necessary to look for signs of sub-surface downward flow even when pile up is clearly present. This has been observed most clearly from the blunt tip indentation into a (13 11 18) surface shown in Figure 5. 5 (e) and (f). The surface slip steps, seen in the derivative AFM image in (e) and the corresponding height image (f) show that pile up is largely limited to two distinct lobes on the left and above the indentation. (Note: the bright area to the right of the indentation in Figure 5. 5(f) does not actually represent a height feature on the surface, but rather is a result of scanner hysterisis, an artifact which occurs as a large voltage is applied to the piezoelectric scanner to raise the AFM tip out of the deep indentation and back up to the surface [67]). For this particular surface orientation, which is rotated 11° from a perfect (111) surface, there are three slip planes that are oriented favorably for slip down into the bulk and the other, the (111), is nearly parallel to the surface. Of the other three slip planes, the (11$\bar{1}$) is inclined 82° to the surface, the ($\bar{1}$11) is 68° and the (1$\bar{1}$1) is at 62°. Figure 5. 13 plots the resolved shear stress as a function of the angle of inclination of a slip plane to the surface. This plot is similar to Figure 5. 10, except here the resolved stress is evaluated where $r=z/10$, which corresponds to 5.7° from the indentation axis, nearly directly beneath the indentation. It can be seen from Figure 5. 13 that for all three of these slip planes, the resolved shear stress will be higher on the negatively inclined slip plane. In addition, the resolved shear stress on the (1$\bar{1}$1), at 62°, is the highest, at 68°, the ($\bar{1}$11)

is a bit lower on and the lowest is on the (11$\bar{1}$) at 82°. Downward flow of material would occur on the ($1\bar{1}1$) and ($\bar{1}11$) slip planes prior to occurring on the (11$\bar{1}$).

Dislocation dynamics simulations were performed and verified that dislocation activity is much greater on the ($1\bar{1}1$) and ($\bar{1}11$) planes than on the (11$\bar{1}$) as shown in Figure 5. 14 (a) and (b). For this simulation, the surface was rotated 10° about the (0$1\bar{1}$) direction which results in a surface normal of approximately (13 13 18), which is similar to the (13 11 18) surface which is shown indented in Figure 5. 14 (c). The overlay of the three slip planes demonstrates the direction of downward material flow due to each of the planes. The two regions of greater pile up correspond with the more active ($1\bar{1}1$) and ($\bar{1}11$) planes.

In this manner greater upward flow, i.e. larger pile up, would occur above the regions with the greatest downward strains. The claim has often been made that pile up occurs where the stress field aligns with the crystallographically preferred slip systems [68]. While this general statement cannot be argued, it might be more accurate to say that pile up will occur above the regions with significant downward flow of material, down into the bulk. This downward flow will be dependant on the alignment of the indentation stress field with the slip systems capable of supporting that flow. Therefore it should be possible to predict pile up behavior based primarily on the slip systems oriented for downward flow.

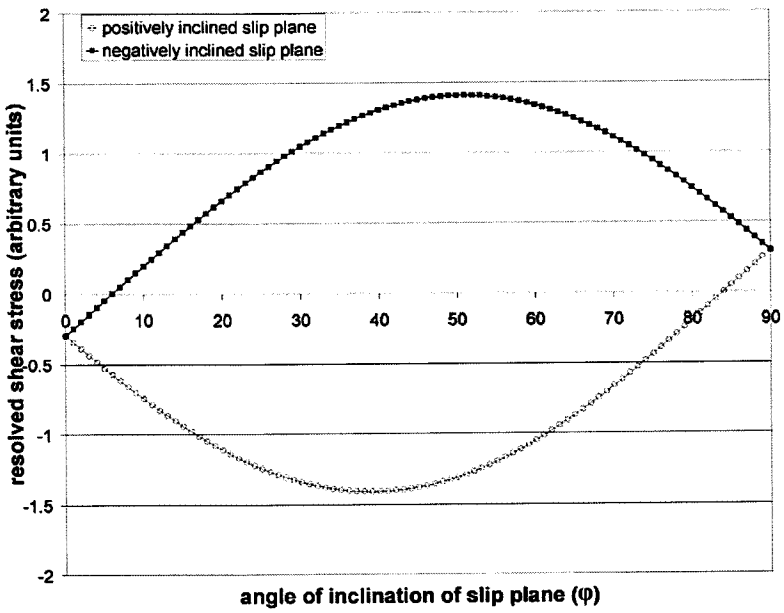

Figure 5. 13 The resolved shear stress measured 5.7 degrees from the axis of indentation changes with the angle of inclination of the slip plane, which is measured with respect to the surface plane. Plane 1 and 2 represent planes at the same angle but opposite inclination.

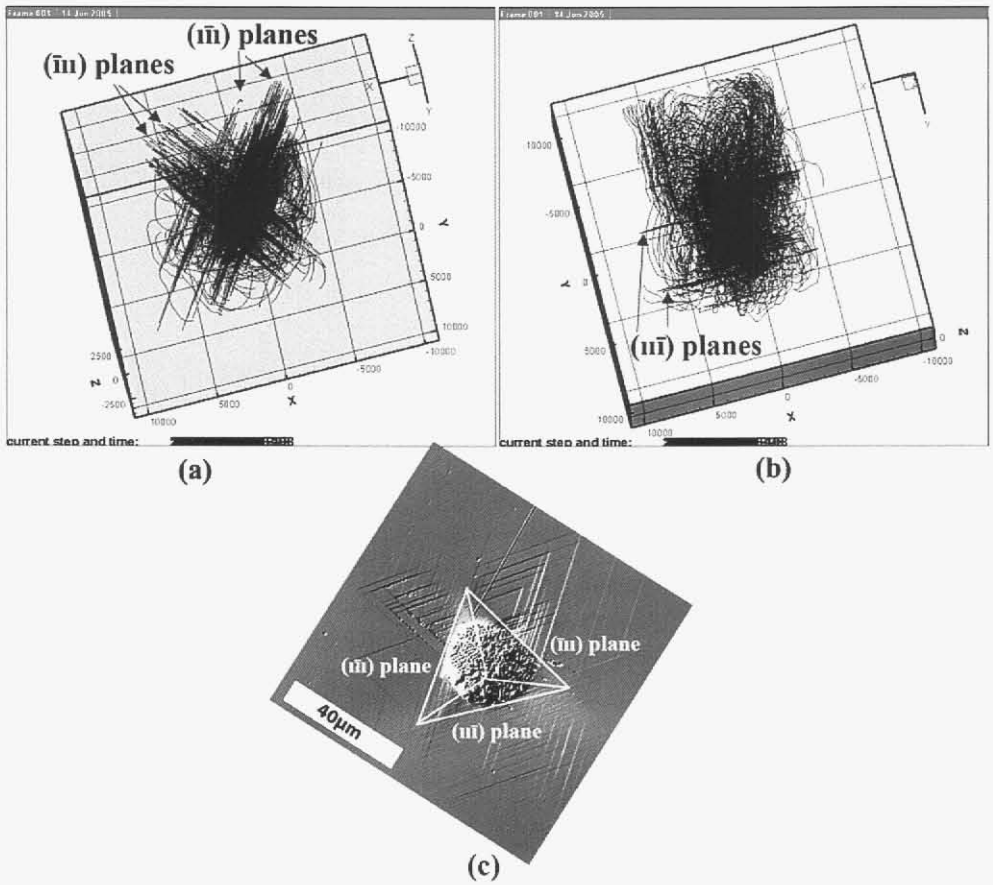

Figure 5. 14 Dislocation dynamics simulations show a high concentration of dislocation loops on the ($\bar{1}$11) and (1$\bar{1}$1) slip planes (a) and only limited activity on the (11$\bar{1}$) planes for a surface rotated 11° for (111). This orientation is very similar to the (13 11 18) surface shown indented in (c). The planes with higher dislocation activity correspond to the regions of greater pile up around the indentation.

5.6.3 Empirical assessment of stresses during pile up

Once pile up is occurring, the elastic back stress of the bulk is responsible for pushing material to the surface. Since satisfactory analytical models of this process have not been well developed, it is valuable to explore some of the necessary attributes for this process and some possible mechanisms to explain it.

When a blunt tip indentation is made into a (1 2 30) oriented surface of 21-6-9, slip steps form with the symmetry expected for a perfect (001) crystal as shown in Figure 5. 15 (a). All of the slip steps occur from the positively inclined slip planes, as is represented by the schematic cross section shown in Figure 5. 15 (c). Figure 5. 15 (b) and (d)

demonstrate that as the strain is increased by indenting with a sharper tip, slip steps begin to form from the negatively inclined slip planes. This would indicate that the resolved shear stress is greater on the positively inclined slip plane, but as that system strains and hardens, the resolved shear stress on the negatively inclined slip plane will reach a value large enough to cause slip. If this is the case, then rotating further from (001) should cause the distribution of resolved stresses on the positive and negatively inclined planes to differ for one side of the indentation with respect to the other. This was tested by performing indentations in a grain with surface orientation of (018) as shown in Figure 5. 16. Indentations made with a blunt tip into this grain show slip steps from only the positively inclined slip planes on one side, but from both planes on the other side. On the left side (as depicted in Figure 5. 16), φ, the angle of inclination of the slip plane with respect to the surface, is decreased from its value in a perfect (001) surface for the positively inclined slip plane, and increased for the negatively inclined slip plane and this results in a greater difference in the resolved shear stress. On the right side, the opposite occurs and the result is a decrease in the difference between the resolved shear stress for each plane. When the strain is increased by using a sharper tip, the steps on the left side still form only from the positively inclined slip plane. On the right side, steps form from both slip planes, with the negatively inclined plane becoming the dominant source of the steps.

The assumption that pile up results from the response of the elastic hinterland implies that the actual stress state which produces the pile up is complicated and the stress field produced by the indenter itself should not be used to directly predict pile up.

An estimate of this response is made by assuming a point loading exists beneath each region of localized strain. Figure 5. 17 demonstrates this situation schematically. Downward flow on slip systems predicted by the elastic stresses produced from the indenter tip produced regions of localized strain beneath the surface. This strain induces an elastic response which pushes material back toward the free surface.

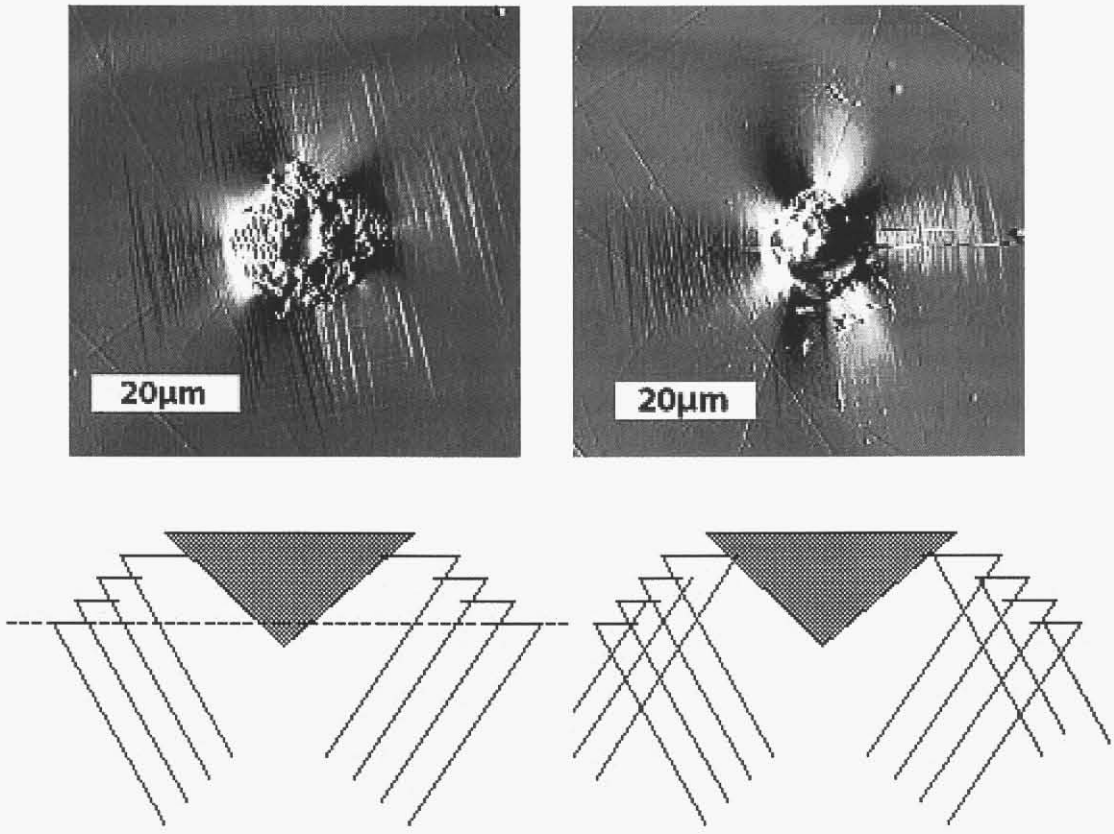

Figure 5. 15 Slip steps form only from the positively inclined slip planes around blunt tip indentations in a grain with surface orientation of (1 2 30). When the effective strain is increased by using a sharp tip, steps form from both the positively and negatively inclined slip planes.

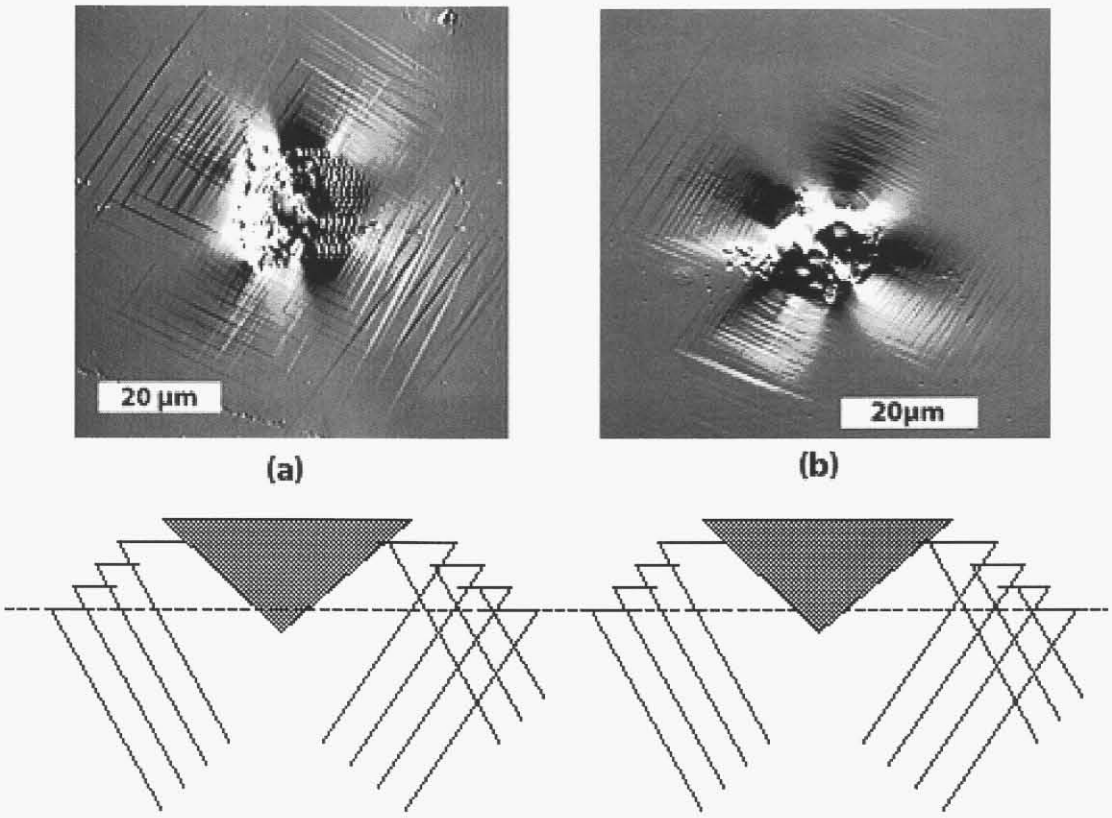

Figure 5. 16 When indentations are made into a grain with surface orientation of (0 1 8), slip steps form from only the positively incline slip plane on one side, but from both the positively and negatively inclined slip planes on the other side. Increasing the strain by using a sharp tip increases the number of slip steps and pile up height but does not appear to change this distribution significantly.

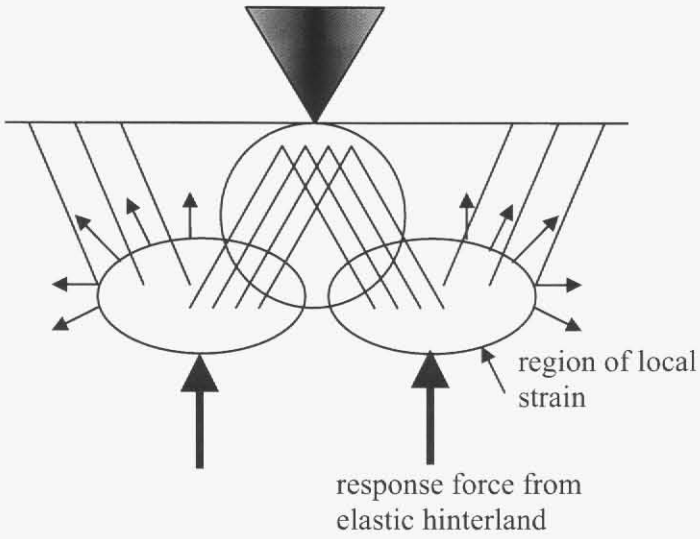

Figure 5. 17 This schematic demonstrates a possible mechanism by which downward strains below the indentation could lead to regions of higher stress beneath the surface which in turn act to promote slip back to the surface to produce out-of-plane pile up.

Figure 5. 18 plots the resolved shear stress which would result from the elastic response when modeled as a point load. In part (a) a perfect (001) surface is assumed and the resolved shear stress is plotted as a function of angular position, α, in the *r,z* plane beneath the indentation where $\alpha=\text{atan}(z/r)=90^{\circ}$ is directly above the point load.

Figure 5. 18 (b) plots the resolved shear stress when the surface is rotated 10°. It can be seen that on the left side the positively inclined slip plane will still have the larger resolved shear stress, whereas on the right side the negatively inclined slip plane will now have the larger resolved shear stress. This result matches that shown in Figure 5. 16 for indentations in a surface with (018) orientation.

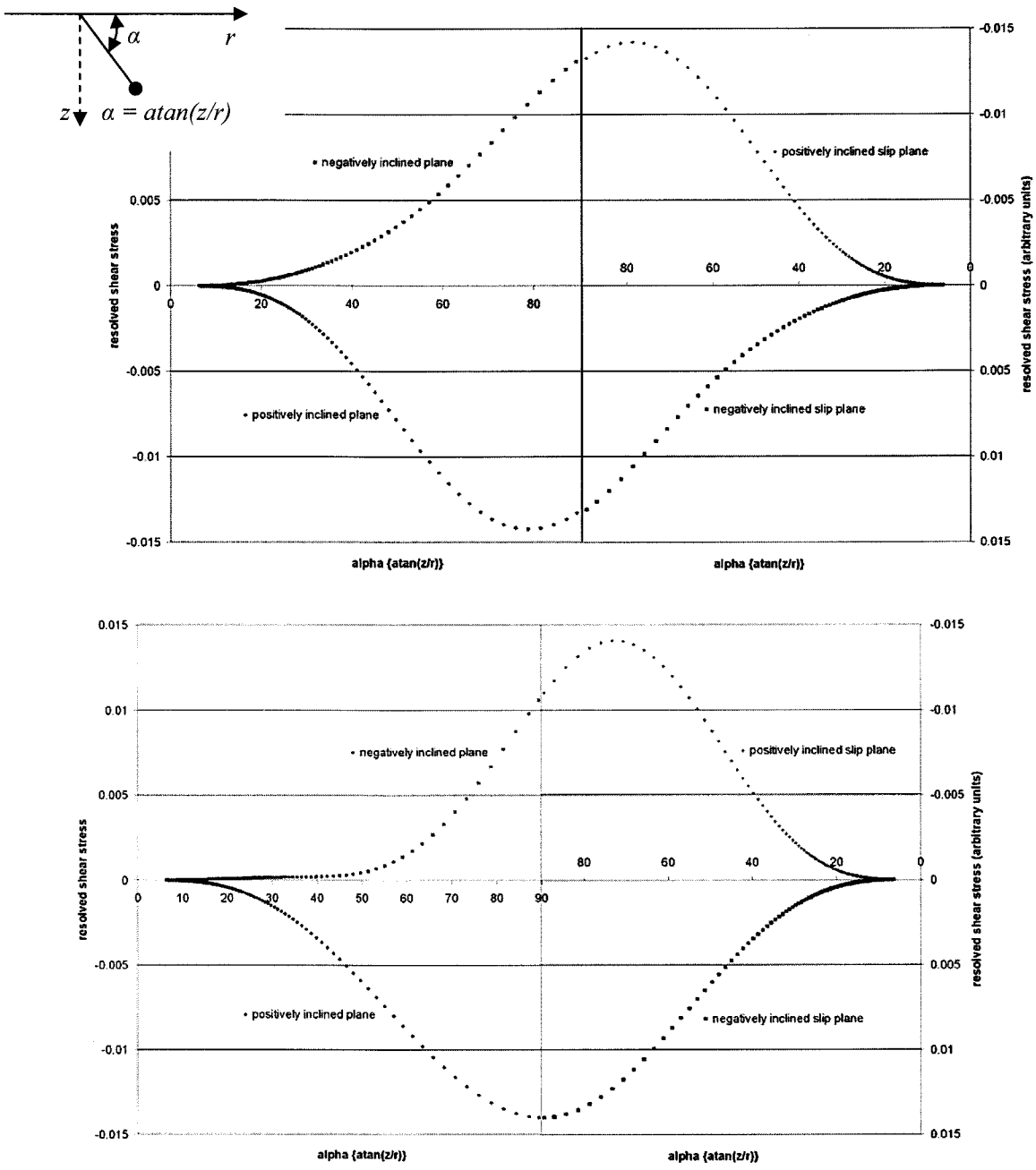

Figure 5. 18 Resolved shear stress resulting from the loading response of the elastic hinterland is plotted as a function of distance from the point of loading. The response stress is approximated as a point loading from beneath the indentation. (a) is plotted for the perfect (001) orientation and on both sides of the indentation the maximum resolved shear stress is always on the positively inclined slip plane. The stress on the negatively inclined slip plane is only somewhat lower. (b) is plotted for a surface rotated 10^{o} from (001). On the left side, the resolved stress on the negatively inclined slip plane is significantly lower than that on the positively inclined slip plane. On the right side, both planes experience similar resolved stresses.

6. Results of in situ film fracture testing

Figure 6.1 shows the anodic polarization behavior of 304 SS in an aqueous solution of pH 1 and a salt concentration of 0.01 M NaCl, respectively; the arrows indicate the stable passive and metastable pitting potentials at which the films were grown. Figure 6.2 illustrates the load-depth curves of ex-situ and in-situ nanoindentations for the passive film formed on 904L stainless steel using the rounded Berkovich indenter tip. Tables 5 and 6 show the design, conditions, the averages and the standard deviations of the loads at fracture for the passive films formed at the stable passive and metastable pitting potentials, respectively. Each cell in the two tables represents the average load at fracture of at least six indents in two different grains. Forcing an indenter into a hard film, the passive oxide film, on a relatively soft substrate, the stainless steel, causes the substrate to deform easier than the film. To accommodate the deformation of the substrate a large tensile stress develops in the film leading to film fracture outside the contact region.

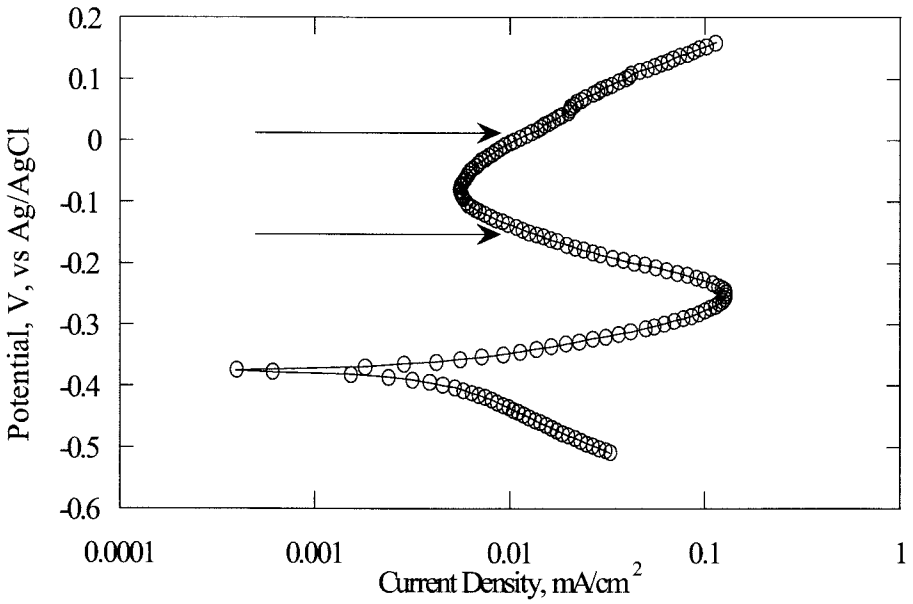

Figure 6.1 typical polarization curve for 304 stainless steel in chloride solution, the arrows indicate to the potentials used to grow the films

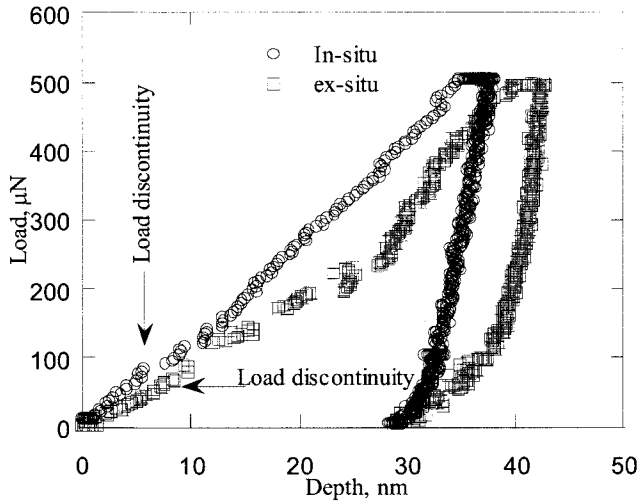

Figure 6.2 Ex-situ and in-situ nanoindentation curves of the passive film formed on 904L in chloride solution

Table 5 The design, conditions, and average fracture load of passive films formed in the stable passive potential region

	Time (min)			60	120	60	120
	Temperature (°C)			40	40	15	15
Condition	SS	pH	S.C	Fracture Load, μN			
1	304	1	0.01	80 ±9	86 ±9	74 ±15	87 ±8
2	304	3	0.05	83 ±11	87 ±11	81 ±10	90 ±5
3	304	5	0.1	89 ±18	86 ±17	82 ±12	94 ±13
4	316	1	0.1	69 ±8	91 ±13	76 ±16	74 ±16
5	316	3	0.01	73 ±8	87 ±6	82 ±10	82 ±11
6	316	5	0.05	74 ±7	80 ±13	89 ±3	86 ±4
7	904	1	0.05	103 ±11	100 ±9	93 ±6	96 ±5
8	904	3	0.1	92 ±9	92 ±11	95 ±12	96 ±9
9	904	5	0.01	98 ±16	96 ±9	99 ±14	105 ±14

Table 6 The design, conditions, and average fracture load of passive films formed in the metastable pitting potential region

	Time (min)			60	120	60	120
	Temperature(°C)			40	40	15	15
Condition	SS	pH	SC	Fracture Load, μN			
1	304	1	0.01	41 ±8	45 ±11	38±9	42 ±9
2	304	3	0.05	44 ±9	40 ±8	48 ±7	39±3
3	304	5	0.1	36 ±6	41 ±6	30 ±6	39 ±3
4	316	1	0.1	40 ±11	35 ±5	43 ±11	42 ±4
5	316	3	0.01	49 ±6	53 ±11	43 ±6	54 ±6
6	316	5	0.05	45 ±7	42 ±5	42 ±5	49 ±7
7	904	1	0.05	49 ±8	53 ±4	46 ±4	56 ±4
8	904	3	0.1	43 ±5	43 ±5	43 ±5	44 ±6
9	904	5	0.01	51 ±5	59 ±3	54 ±3	60 ±8

The shape of tip influences the load required to fracture the passive film. Two different tips were using in this study, a cube corner tip was utilized to indent the passive film in ambient air while the in-situ nanoindentation measurements were preformed using a Berkovich tip. Figure 6.3 illustrates the main effect plot for the load required to fracture the passive film formed at a stable passive and metastable pitting potentials measured ex-situ and in-situ. The Y axis represents the load required to fracture the film. On the X axis, the levels of the control factors, alloy chemistry, pH, and salt concentration, are represented. The dashed line illustrates the overall average of the load at fracture for all testing conditions. The sharper tip (the cube corner) leads to fracture at a lower load than the blunter Berkovich tip.

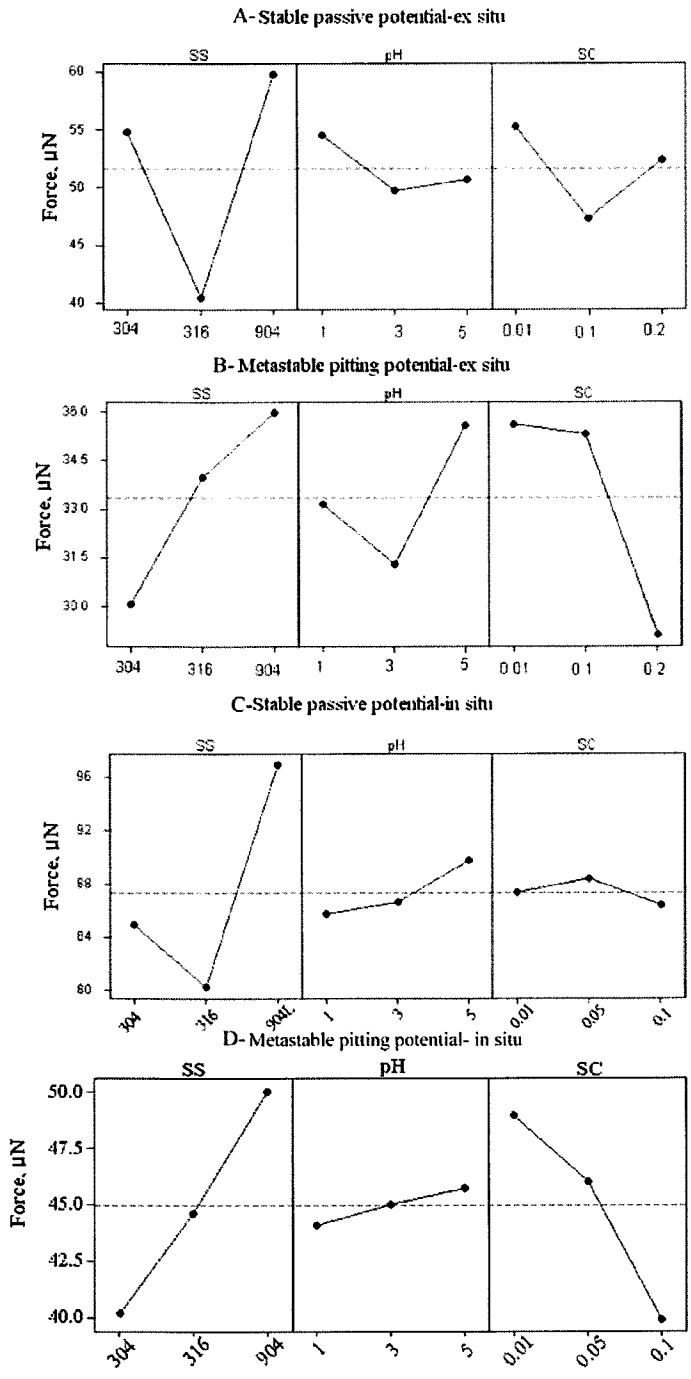

Figure 6.3 Main effect plot for the load required to fracture the passive film formed at A) stable passive potential and measured ex-situ, B) metastable pitting potential and measured ex-situ, C) stable passive potential and measured in-situ, and D) metastable pitting potential and measured in-situ.

Rather than solely compare loads for fracture, one possible method to approximate the applied tensile stress is to use a first order estimation by assuming the initial loading is similar to the elastic loading of surface by a sphere. The radial tensile stress at the contact surface for elastic contacts can estimated by using Hertzian contact mechanics of spherical bodies which is given by [19]

$$\sigma = \frac{1-2\upsilon}{3}\left[\frac{6PE^{*2}}{\pi^3 R^2}\right]^{\frac{1}{3}} \tag{22}$$

where P is the load at fracture, E^* is the reduced modulus, R is the effective radius of curvature which is defined as [69]

$$\frac{1}{E^*} = \frac{(1-\upsilon_i^2)}{E_i} + \frac{(1-\upsilon_f^2)}{E_f} \tag{23}$$

where E and ν are the elastic modulus and Poisson's ratio of the indenter and the film, respectively. The in-situ nanoindentation measurements for the loads at fracture were used to roughly estimate the radial stress by using equations (1) and (2). The elastic modulus and Poisson ratio of the passive film and the tip were assumed to be 325GPa and 0.25 and 1140 GPa and 0.07, respectively [70,35]. The values of stress were statistically analyzed using Minitab®, a commercial software program.

The significant level was set at 0.05. Therefore, any test resulting in a p value under 0.05 would be significant. In-situ nanoindentation measurements of the passive film formed at the stable passive potential showed that the alloy chemistry had the most significant effect on the load at fracture with P values equal to 0.032 and 0.028 for the linear and quadratic effects respectively. On the other hand, the linear influences of both the alloy chemistry and the salt concentration had the significant influences on the load at fracture for the passive film formed at a metastable pitting potential; the P values were equal to 0.042 and 0.049 .respectively.

Figures 6.4 and 6.5 show the main effect plots based on in situ measurements for the tensile stress required to fracture the passive film formed at the stable passive and metastable pitting potential, respectively. The Y axis represents the applied tensile stress. On the X axis, the levels of the control factors, alloy chemistry, pH, and salt concentration, are represented. The

dashed line illustrates the overall average of the applied tensile stress at fracture for all testing conditions.

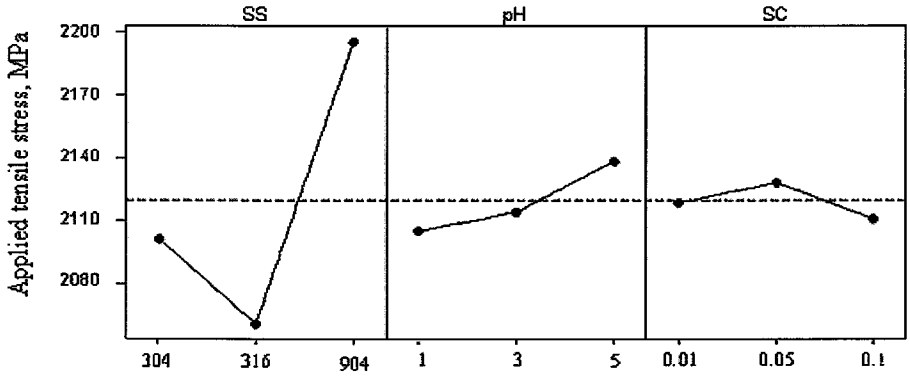

Figure 6.4 The effect of the controlled factors (salt concentration, pH, and stainless alloy composition) on the tensile stress applied to the passive films formed at a stable passive potential during in-situ experiments.

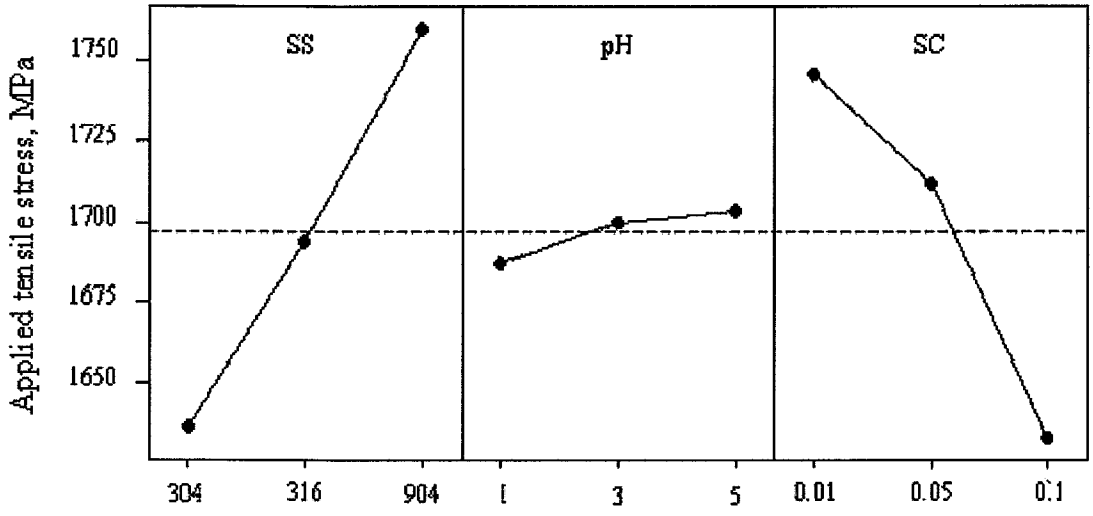

Figure 6.5 The effect of the controlled factors (salt concentration, pH, and stainless alloy composition) on the tensile stress applied to the passive films formed at a metastable pitting potential during in-situ experiments.

For the passive films formed at the stable passive potential, figure 6.4 shows that the substrate on which the passive film is formed was the most important factor affecting the tensile stress required to fracture the film; changing the substrate from 316SS to 304SS to 904L SS increased the strength of the passive film correspondingly. The influences of pH and the salt

concentration are almost negligible. Similar results were obtained for the films indented in air [37].

For the passive film formed at the metastable pitting potential, on the other hand, figure 6.5 shows that the tensile stress required to fracture the film is significantly influenced by both the salt concentration in the electrolyte and the substrate on which the film was formed. Increasing the salt concentration in the electrolyte from 0.01 to 0.05 to 0.1 M NaCl decreased the applied tensile stresses needed to fracture the film from 1.74 ± 0.09 to 1.70 ± 0.06 to 1.63 ± 0.05 GPa, respectively. The applied tensile stresses needed to fracture the film reduced from 1.76 ± 0.08 to 1.70 ± 0.06 to 1.63 ± 0.04 GPa when the substrate on which the film was formed was changed from 904L SS to 316SS to 304SS.

Figures 6.6 and 6.7 illustrate the influence of the applied potential on ex situ and in situ measurements, respectively, for the applied tensile stresses caused the fracture of the passive film formed at the different conditions. The X axis illustrates the growth conditions corresponding to the rows in tables 1 and 2. The bars show the standard deviation while the circles and squares illustrate the average applied tensile stress that caused passive film fracture for each condition. Figures 6.6 and 6.7 shows that the passive films formed at the stable passive potential were stronger than those formed at a metastable pitting potential. The overall average tensile stress required to fracture the passive film formed at the stable passive potential decreased from 3.05GPa to 2.10GPa when the test environment was changed from ex situ to in situ. For the passive film formed at the metastable pitting potential changing the test environment from ex situ to in situ reduces the tensile stress required to break the film from 2.60GPa to 1.7GPa as shown in figure 6.8.

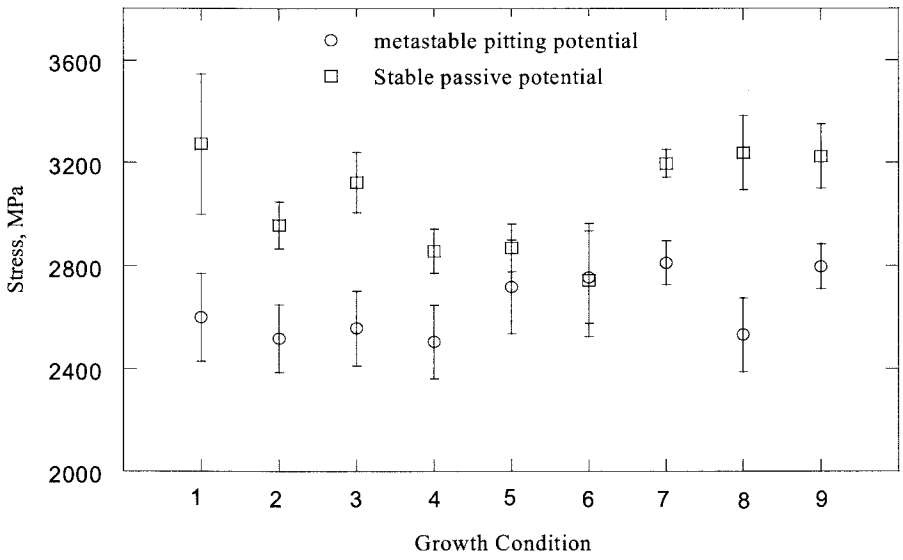

Figure 6. 6 Ex-situ results of the applied tensile stress at fracture for the passive film growth conditions shown in Table 1.

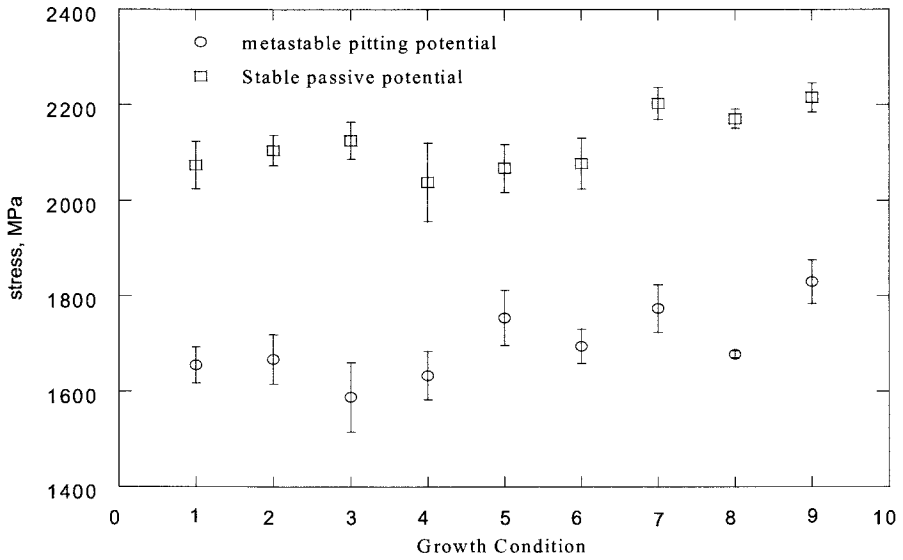

Figure 6.7 In-situ results of the applied tensile stress at fracture for the passive film growth conditions shown in Table 1.

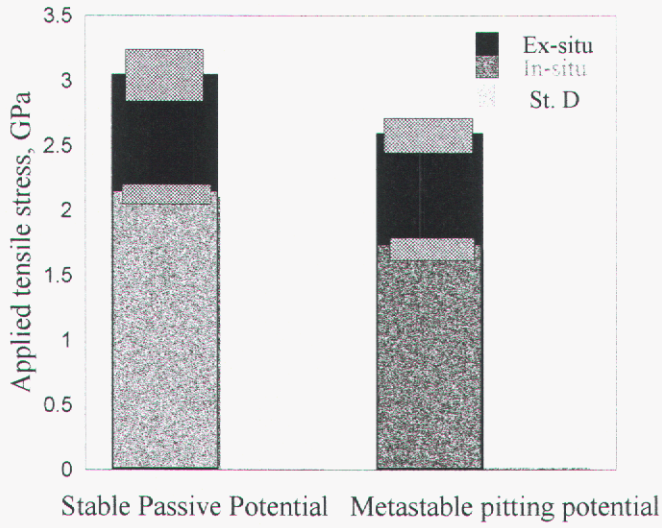

Figure 6. 8 The overall averages of the applied tensile stress required to fracture the passive films formed at stable passive and metastable pitting potentials and indented in ambient air and in situ

An important point to note in this study is the similarity between the trends observed in the in-situ and ex-situ experiments. For instance, in comparing the effects of alloy composition at a passive potential (Figure 4a and c), the film on 304 SS was stronger than the film on 316 SS, and the film formed on 904L was stronger than either of the other alloys. However, at the metastable pitting potential (Figure 4b and d), the film formed on 304 SS was the weakest while the film formed on 904L was the strongest. These similarities in the trends (the actual loads vary due to different tips used for these experiments) suggest that the observed changes in strength are due to the passive film, and not a salt film (which would have been removed in the ex-situ test) or solely substrate effects (because the passive and metastable potentials vary). The influence of the alloy chemistry on the tensile stress required to fracture the passive film formed could be due to the change of the film structure. A previous transmission electron microscopy study of these alloys found that the film formed on 904L SS was an epitaxial layer while for the films formed on 304SS and 316SS consisted of small crystalline islands [71].

Generally, both ex-situ and in-situ measurements indicate that the films formed at the stable passive potential were stronger than those formed at the metastable pitting potential. The

influence of the applied potential on the tensile stress needed to fracture the films might be explained by the two possible mechanisms: First, the repeated repassivation-depassivation process which takes place at the metastable pitting potential. Dawson and Ferreira [72] observed the repassivation-depassivation process as pulses of current in the polarization curves, and described the repassivation-depassivation process to the film breaking down due to mechanical effects of chloride adsorption on the film. In the stable potential regime the chloride would be less likely to adsorb and become incorporated in the film. The second reason for the decrease in the film strength at increased potential is that an increase of the applied potential increases the iron content in the film [73,74]. This increase could mechanically weaken the passive film formed on austenitic stainless steels due to subsequent changes in film structure.

The passive films tested in air were stronger than films indented in-situ. This might be due to the reaction of the film with the ambient environment during the transfer from the electrolyte to the nanoindenter which might have increased the film stability [75,76]. Moreover, the difference in the tensile stress values of the ex-situ and in-situ film could be attributed to the capillary effect of the thin water layer between the nanoindenter tip and the surface while measuring in situ passive films, which other authors have found to impact the surface mechanical behavior [77,78].

7.0 Conclusions

7.1 Conclusions regarding indentation induced film fracture

Two different methods for determining the stress intensity at fracture of the thin films using nanoindentation were outlined and tested. The method outlined in chapter 3 utilized a plate bending approach to determine the stress intensity at fracture. Chapter 4 discussed a method by measuring the energy at film fracture from the load-depth curves. The ability to incorporate two different metal oxide systems to the energy method implies that it could be universal for hard film soft substrate systems. The plate bending approach was only tested using the aluminum oxide/aluminum system. The results from the plate bending method were in good comparison to the stress intensity calculations from the energy method. The final results for both methods were reasonable values for the stress intensities and crack extension forces.

This plate bending method developed a first order analytical model for characterizing the stress intensity leading to thin film failure during nanoindentation, and applied this model to thermally grown oxide films on aluminum. The films were modeled as a thin elastic circular plate with clamped edges supported by a compliant substrate. In the aluminum oxide/aluminum system, the radial stress at fracture was calculated using a superposition of the bending and membrane stress. The bending stress was found to dominate the overall stress at fracture. The 63 nm films were determined to have ultimate strengths of 8.87, 4.77, and 6.21 GPa for the 1100 Al mechanically polished, 1100 Al electropolished, and 99.99% Al mechanically polished substrates, respectively.

The applied stress intensity factor was calculated from the bending moment produced during indentation. The radial force was neglected in the stress intensity factor calculation due minimal deflection of the oxide at failure. As the ratio of crack size to film thickness increased to 0.30 (which is approximately the ratio of the roughness of the films to the total film thickness) the stress intensity at fracture increased to 1.76, 0.93, and 0.63 $MPam^{1/2}$ for the 99.99% pure mechanically polished, 1100 electropolished, and the 1100 Al mechanically polished substrates, respectively. It is interesting to note that the oxide the grown on the 99.99% pure aluminum substrate had the highest load at fracture and was shown to have the highest stress intensity at fracture. The reason for this is that the oxide film grown on the 99.99% pure aluminum substrate would have fewer trace elements producing a higher quality film. The 1100 aluminum substrate

contains trace amounts of foreign elements that could be incorporated into the oxide during growth.

An energy based method was used to determine the toughness of brittle oxide films on metal substrates. The total energy being applied to the system is a superposition of the energy needed to deform the film and the substrate. The initial loading for the film/substrate system was steeper than the response from the substrate. The applied energy difference between the film/substrate system and the substrate alone was the energy applied to the film. The loading profile of both the film/substrates system and the substrate was then integrated up to the same critical depth as the system. Subtraction of the energy applied to the substrate from the system gives the fracture energy of the film. The crack extension force, or energy per unit area of crack surface, was determined by dividing the energy by newly acquired surface produced from crack initiation and propagation by using the relationship that the film is a high strength ceramic and it undergoes elastic deformation until fracture. The average crack extension force for the various thicknesses and substrates ranged from 0.32 to 1.67 J/m^2. The stress intensity at fracture for the various aluminum substrates and oxide thicknesses ranged from 0.37 and 0.83 $MPam^{1/2}$. The average crack extension force and stress intensity at fracture for the 200 nm thick titanium oxide film was 19.8 J/m^2 and 2.51 $MPam^{1/2}$, respectively.

Defects in the films were the main contributor to fracture. The 25nm thick films were shown to fracture at the highest stress intensity and decreased with thickness according to the energy method. This result is similar to the stress intensity graph from the plate bending approach for a constant defect size to film thickness ratio. This implies that the critical defect size is scaling with film thickness. The critical defect in the thermally grown oxide films are the equiaxed grains produced during growth. Other sources of defects could be from dislocations in the film created from either lattice misfits between the film and substrate, a rough substrate surface, or foreign particles in the substrate. As the film thickness increases and the defects are typically created from the substrate they can become more pronounced.

The fracture pattern is believed to be circumferential around the indentation contact area. Even though the cracking pattern for the thermally grown samples were not able to be directly observed after the first discontinuity, it was shown that at indentations with maximum loads beyond the first discontinuity to have predominately circumferential cracking with crushing of the film beneath the tip's contact area. An anodized aluminum sample was shown to fracture in a

circumferential pattern around the indentation. Indentations beyond the first discontinuity of the anodized aluminum showed sequential circumferential cracking of the film.

The approximated stress intensity factors for aluminum oxide thin films on aluminum substrates are in good agreement with observations made by Thurn and Cook. [79] Vapor deposited alumina films were found to have a stress intensity at fracture between 1.7 and 2.1 $MPam^{1/2}$. The stress intensity factor shows that very low loads can cause film fracture with the presence of small surface flaws.

7.2 Conclusions regarding slip step analysis

Slip steps appear around indentations in a consistent and repeatable manner. The steps form in the outer region of the plastic zone and, as the plastic zone continues to expand outward, steps will cease to grow larger. The general form of the patterns formed by the slip steps is dependant on crystal orientation while tip geometry has less significant affects. The elastic stresses generated from a concentrated point loading can be used to estimate the stresses responsible from downward flow of material around an indentation, but if out-of-plane pile up is observed, the stress state is significantly more complicated. Even for indentations as small as a couple microns, indentations produce well developed plastic zones with dislocation structures comparable to those developed in bulk tests.

7.3 Conclusions regarding in situ electrochemistry and indentation for film fracture

For passive films formed at stable passive potentials on austenitic stainless steels, the alloy chemistry was the most important factor affecting the strength of the passive film; films grown on 316 SS were weaker than films grown on 304 SS which were weaker than films formed on 904L. The salt concentration and the alloy chemistry were the two important factors that affected the mechanical strength passive film formed at a metastable pitting potential; at this potential increasing the salt concentration decreased the strength of the passive film. The strength of passive films measured in situ during electrochemical film growth is approximately 33% less than when the same films are tested in ambient conditions after removal from solution. However, the similarity between trends in film strength with alloy chemistry and salt concentration implies the in-situ and ex-situ tests are indeed measuring similar mechanical properties of these anodically grown passive films.

8.0 Acknowledgements

The authors gratefully acknowledge the support of Sandia National Laboratories under contract DE-AC04-94AL85000. Sandia is a multiprogram laboratory operated by Sandia Corporation, a Lockheed Martin Company for the United States Department of Energy's National Nuclear Security Administration under contract DE-AC04-94AL85000. This work would not have been possible except for the extensive efforts of the students involved in the project, including those not directly supported but who provided assistance on experimental techniques. In particular we wish to thank:

Bachelor of Science

Mr. Scott Anderson, BS Materials Science and Engineering, May 2005

Mr. Richard Vance, BS Materials Science and Engineering, expected May 2006

Masters of Science

Ms. Marian Kennedy, MS Materials Science and Engineering, December 2003

Mr. Kevin R. Morasch, MS Materials Science and Engineering, May 2005

Doctor of Philosophy

Dr. Abdulaziz Al-amr, Ph.D. Materials Science, May 2005

Dr. Kevin A. Nibur, Ph.D. Materials Science, August 2005

Mr. Gus Vasquez, Ph.D. Materials Science expected 2007.

9.0 Publications, Presentations, and Professional Activities 2003-2005

Books, Book Chapters, and Editor

1. Comprehensive Structural Integrity, Chapter 8.13, *Nanoindentation methods in interfacial fracture testing*, by A. A. Volinsky, D. F. Bahr, M. D. Kriese, N. R. Moody, and W. W. Gerberich, Elsevier Science, Amsterdam, The Netherlands (2003)
2. Mechanical Properties Derived from Nanostructuring Materials, Materials Research Society Symposium Proceedings, vol. 778, eds. David F. Bahr, Harriet Kung, Neville R. Moody, and Kathryn J. Wahl , Materials Research Society, Warrendale PA (2003)
3. Fundamentals of Nanoindentation and Nanotribology III, , Materials Research Society Symposium Proceedings, vol. 841, eds. Kathryn J. Wahl, Norbert Huber, Adrian B. Mann, David F. Bahr, and Y.-T. Cheng , Warrendale, PA (2005).
4. *Mechanical Properties of Nanostructured Materials—Experiments and Modeling,* Materials Research Society Symposium Proceedings, vol. 880, edited by J.G. Swadener, E. Lilleodden, S. Asif, D. Bahr, and D. Weygand, Warrendale, PA (2005)

Refereed Journal Publications

1. *Mechanical Measurements of Passive Film Fracture on an Austenitic Stainless Steel*
   D. Rodriguez-Marek, M. Pang, and D.F. Bahr, Metallurgical and Materials Transactions, A. vol. 34A, pp. 1291-1296 (2003)
2. *Quantifying improvements in adhesion of platinum films on brittle substrates*
   M.J. Cordill, N.R. Moody, and D.F. Bahr, Journal of Materials Research, vol. 17, pp. 181-1825 (2004).
3. *Hydrogen Effects on Dislocations Around Indentations*
   K.A. Nibur, D.F. Bahr, and B.P. Somerday, TMS Letters, vol. 1, pp. 1-2 (2004).
4. *Recent Developments in Thin Film Adhesion Measurement*
   M.J. Cordill, D.F. Bahr, N.R. Moody, and W.W. Gerberich, IEEE Transactions on Device and Materials Reliability, vol. 4, pp. 163-168 (2004).
5. *Effects of Microstructure on the mechanical properties of copper films for high aspect ratio structures,*
   M.J. Cordill, T. Muppidi, N.R. Moody, D.F. Bahr, Microsystem Technologies, vol. 10, pp. 451-455 (2004).
6. *Length Scale Based Hardening Model for Ultra-small Volumes*
   J.M. Jungk, W.M. Mook, M.J. Cordill, M.D. Chambers, W.W. Gerberich, D.F. Bahr, N.R. Moody, J.W. Hoehn, Journal of Materials Research, vol. 19, pp. 2812-2821 (2004).
7. *Coupling Bulge Testing and Nanoindentation to Characterize Materials Properties of Bulk Micromachined Structures*
   M.S. Kennedy, A.L. Olson, J.C. Raupp, N.R. Moody, D.F. Bahr, Microsystem Technologies, vol. 11, pp. 298-302 (2005).
8. *The Effects of Plasticity on Adhesion of Hard Films on Ductile Interlayers*
   M.J. Cordill, N.R. Moody, and D.F. Bahr, Acta Materialia, vol. 53, pp. 2555-2562 (2005).
9. *Effects of alloy and solution chemistry on the fracture of passive films on austenitic stainless steel*
   A. Alamr, D.F. Bahr, and Michael Jacroux, Corrosion Science, in press (2005).

10. *Nanomechanical Testing for Fracture of Oxide Films*
K.R. Morasch and D.F. Bahr, Journal of Materials Research, vol.20, 1490-1497 (2005)
11. *The Effects of Solid Solution Impurities on Dislocation Nucleation During Nanoindentation*
D.F. Bahr and G. Vasquez, Journal of Materials Research, vol. 20, 1947-1951 (2005).

Conference Proceedings

1. *Probing Hydrogen – Deformation Interactions Using Nanoindentation*
D.F. Bahr, K.A. Nibur, K.R. Morasch, and D.P. Field, Hydrogen Effects on Material Behavior and Corrosion Deformation Interactions, N.R. Moody, A.W. Thompson, G.W. Was, R. Ricker, and R.H. Jones, ed., TMS, Warrendale PA, pp. 165-172 (2004)
2. *Investigation of Indentation Methods for Properties Determination in Hard Film - Soft Substrate Systems*
M.S. Kennedy, N.R. Moody, and D.F. Bahr in *Fundamentals of Nanoindentation and Nanotribology III,* edited by Kathryn J. Wahl, Norbert Huber, Adrian B. Mann, David F. Bahr, and Y.-T. Cheng, Proceedings of the Materials Research Society. **841**, pp. R12.7 (2005).

Presentations

1. *Fracture in Thin Oxide Films*
D.F. Bahr, **Invited**, Materials Research Society Fall Meeting, Symposium U, Thin Films Stresses and Mechanical Properties X, December 2 (2003)
2. *Adhesion of Hard Coatings on Electroplated Metals for Microelectronic Based Systems*
D.F. Bahr, M.J. Cordill, and N.R. Moody, TMS Annual Meeting, 5th Global Innovations Symposium: Trends in LIGA, Miniaturization, and Nano-scale Materials: Small Volume Deformation, March (2004)
3. *Through thickness fracture behavior in hard films on soft substrates*
4. D.F. Bahr **Invited**, K.R. Morasch, M.S. Kennedy, S.P. Anderson, A Alamr, and N.R. Moody, TMS Annual Meeting, Mechanical Properties of Thin Films and MEMS Symposium, February (2005)
5. *Adhesion and through thickness fracture of ceramic – metal systems in MEMS*
D.F. Bahr, **Invited**, Army Research Office Workshop on Dynamic Fracture in MEMS, Arlington, VA, August (2005).

Professional Activities

Symposium Organizer:
"Fundamentals of Nanoindentation and Nanotribology III", MRS Fall Meeting 2004.
"Mechanical Properties of Nanostructured Materials – Experiments and Modeling", MRS Spring Meeting 2005.

Professional Committee Membership and Leadership –
ASM/TMS Joint Mechanical Behavior Chair 10/04-9/06
TMS Nanomechanical Behavior of Materials Committee, member 2/02- present
TMS Student Affairs Committee, member 3/04 - present
TMS Public and Governmental Affairs Committee, member 2/05 - present
MRS Web Subcommittee member 1/03 – 9/03, Chair 10/03 - present

10.0 References

1. N.G. Chechenin, J. Bottiger, and J.P. Krog: Nanoindentation of amorphous aluminum oxide films II. Critical parameters for the breakthrough and a membrane effect in thin hard films on soft substrates, *Thin Solid Films* **261**, 228-235 (1995)
2. M. Pang and D.F. Bahr: Thin-film fracture during nanoindentation of a titanium oxide film-titanium system, *J. Mater. Res.* **16**, 2634-2641 (2001)
3. T.F. Page, W.C. Oliver, and C.J. McHargue: The deformation behavior of ceramic crystals subjected to very low load (nano) indentations, *J. Mater. Res.* **7**, 450-473 (1992)
4. S.K. Venkataraman, D.L. Kohlstedt and W.W. Gerberich: Continuous microindentation of passivating surfaces, *J. Mater. Res.* **8**, 685-688 (1993)
5. D.E. Kramer, K.B. Yoder, and W.W. Gerberich: Surface constrained plasticity: oxide rupture and the yield point process, *Phil. Mag. A* **81**, 2033-2058 (2001)
6. D.F. Bahr, C.L. Woodcock, M. Pang, K.D. Weaver, and N.R. Moody: Indentation induced film fracture in hard film – soft substrate systems, *Inter. J. Frac.* **119/120**, 339-349 (2003)
7. D. Rodriquez – Marek, M. Pang and D.F., Bahr: Mechanical Measurements of passive film fracture on an austenitic stainless steel, *Metal. Mater. Trans. A* **34A**, 1291-1295 (2003)
8. S.V. Hainsworth , M.R. McGurk, and T.F. Page: The effect of coating cracking on the indentation response of thin hard coated systems, *Surf. Coat. Tech.* **102**, 97-107 (1998)
9. R. Andersson, G. Toth, L. Gan, and M.V. Swain, Indentation response and cracking of sub-micron silica films on a polymeric substrate, *Eng. Fract. Mech.* **61**, 93-105 (1998)
10. M.R. McGurk, H.W. Chandler, P.C. Twigg and T.F Page: Modelling the hardness response of coated systems: the plate bending approach, *Surf. Coat. Tech.* **68/69**, 576-581 (1994)
11. W.W. Gerberich, A. Strojny, K. Yoder and L-S. Cheng: Hard protective overlayers on viscoelastic-plastic substrates, *J. Mater. Res.* **14**, 2210-2218 (1999)
12. E. Wepplemann and M.V. Swain: Investigation of the stresses and stress intensity factors responsible for fracture of thin protective films during ultra-micro indentation tests with spherical indenters, *Thin Solid Films* **286**, 111-121 (1996)
13. H. Chai and B.R. Lawn: Fracture mode transitions in brittle coatings on compliant substrates as a function of thickness, *J. Mater. Res.* **19**, 1752-1761 (2004)
14. J. Malzbender and G. de With: Energy dissipation, fracture toughness and the indentation load-displacement curve of coated materials, *Surf. Coat. Tech.* 135, 60-68 (2000)
15. X. Li and B. Bhushan: Measurement of fracture toughness of ultra thin amorphous carbon films, *Thin Solid Films*, **315**, 214-221 (1998)
16. X. Li, D. Diao, and B. Bhushan: Fracture mechanisms of thin amorphous carbon films in nanoindentation, *Acta Mater.* **45,** 4453-4461 (1997)
17. P.G. Th. van der Varst and G. de With: Energy based approach to the failure of brittle coatings on metallic substrates, *Thin Solid Films* **384**, 85-89 (2001)

18. A. Abdul-Baqi and E. Van der Griessen: Numerical Analysis of indentation-induced cracking of brittle coatings on ductile substrates, *Int. J. of Sol. Struct.* **39,** 1427-1442 (2002)

19. K.L. Johnson: *Contact Mechanics*, (Cambridge University Press, Cambridge, U.K., (1985)

20. S.V. Hainsworth, H.W. Chandler, and T.F. Page: Analysis of nanoindentation load-displacement loading curves, *J. Mater. Res.*, **11** 1987-1995 (1996)

21. D.F. Bahr, K.A. Nibur and K.R. Morasch, Journal of Electronic Materials, vol. **31**, pp. 66 - 70 (2002)

22. E. Carrasco, M. A. Gonzalez, O. Rodriguez de la Fuente, and J. M. Rojo "Analysis at Atomic Level of Dislocation Emission and Motion Around Nanoindentations in Gold" *Surface Science* Vol. 572 (2004) pp. 467-475.

23. S. E. Kadjik and A. Broese Van Groenou "Cross-Slip Patterns by Sphere Indentations on Single Crystal MnZn Ferrite" *Acta. Metall.,* Vol. 37, No. 10, (1989) pp. 2625-2634.

24. C. Tromas, J. C. Girard, V. Audrier, and J. Woirgard "Study of the low stress plasticity in single-crystal MgO by nanoindentation and atomic force microscopy" *Kluwer Academic Publishers,* Vol. 34 (1999) pp. 5337-5342.

25. Y. Gaillard, C. Tromas and J. Woirgard "Pop-in phenomenon in MgO and LiF: observations of dislocation structures" *Philosphical Magazine Letters,* Vol. 83, No. 9, (2003) pp. 553-561.

26. Y. Gaillard, C. Tromas, and J. Woirgard "Study of the dislocation structure involved in a nanoindentation test by atomic force microscopy and controlled chemical etching", Acta Materialia, Vol. 51 (2003) pp. 1059-1065.

27. C. -O. A. Olsson and D. Landolt. Passive films on stainless steels—chemistry, structure and growth. *Electrochimia acta.* **48** (2003) 1093-1104.

28. J.X. Li, W.Y. Chu, Y.B. Wang, and L.J. Qiao. In situ TEM study of stress corrosion cracking of austenitic stainless steel. *Corrosion Science* **45** (2003) 1355-1365.

29. R.M. Latanision and R.W. Staehle. Plastic deformation of electrochemically polarization nickel single crystals. *Acta Metall.* **17** (1969) 307-319.

30. S.F. Bubar and D.A. Vermilyea. Deformation of passive films. *J. Electrochem Soc.* **114** (1967) 882-885.

31. D.G. Kolman, M.A. Gaudett, and J.R. Scully. Modeling of anodic current transients resulting from oxide rupture of plastically strained β+□ titanium. *J. Electrochem. Soc.* **145** (1998) 1829-1839

32. K.J. Bowman, S.E.Harrfield-Wunsch, and R. Gibala. Surface film effects during cyclic deformation of dislocation-mobility-limited materials. *Scripta Metal. Mater.*. **26** (1992) 1529-1534

33. M. Chiba and M. Seo. Potential dependence of normalized friction coefficient of passive iron surface evaluated by nano-scratching in solution. *Electrochimica Acta,* **50** (2004) 967-975.

34. U.Kamachi Mudali, and Y. Katada. Electrochemical atomic force microscopic studies on passive films of nitrogen-bearing austenitic stainless steels. *Electrochimica Acta.* **46** (2001) 3735-3742

35. W. C. Oliver & G. M. Pharr. An improved technique for determining hardness and elastic modulus using load and displacement sensing indentation experiments. *J. Mater. Res.* **7**. No. 6. 1564-1583.(June 1992)

36. Y. Yao, X. Cao, L. Qaio, and W. Chu. Yield point phenomena during nanoindentation. *Tribology Trans.*. **47** (2004) 239-247

37. A. Alamr, D. Bahr, and M. Jacroux. Effects of alloy and solution chemistry on the fracture of passive films on austenitic stainless steel. *Corrosion Science* (2005) in press

38. A. Alamr, D. Bahr, and M. Jacroux. Effects of alloy and solution chemistry on the fracture of anodic films formed at metastable pitting potentials. *Corrosion eng. sci. tech.* (2005) in press.

39. D.W. Aylmore, S.J. Gregg, W.B. Jepson: The oxidation of aluminum in dry oxygen in the temperature range 400-650 °C, *J. Inst. Metals* **88**, 205-208 (1959)

40. E.A. Gulbransen and W.S. Wysong: Thin oxide films on aluminum, *J. Phys. Colloid Chem.*, **51**, 1087-1103 (1947)

41. L.P.H Jeurgens, W.G. Sloof, F.D. Tichelaar, and E.J. Mittemeijer: Structure and morphology of aluminum-oxide films formed by thermal oxidation of aluminum, *Thin Solid Films* **418**, 89-101 (2002)

42. A.B. Mann and J.B.Pethica. nanoindentation studies in a liquid environment. *Langmuir*. **12** (1996) 4583-4586

43. N.Q. Chinh, Gy. Horvath, Zs. Kovacs, and J. Lendvai: Characterization of plastic instability steps occurring in depth-sensing indentation tests, *Mater. Sci. Eng. A* **324**, 219-224 (2002)

44. M.Y. He, A.G. Evans, and J.W. Hutchinson: The Ratcheting of compressed thermally grown thin films on ductile substrates, *Acta Mater.* **48**, 2593-2601 (2000)

45. V.K. Tolpygo and D.R. Clarke: Wrinkling of □-alumina films grown by thermal oxidation I. Quantitative studies on single crystals of Fe-Cr-Al alloy, *Acta Mater.* **46** 5153-5166 (1998)

46. D. Kramer, H. Huang, M. Kriese, J. Robach, J. Nelson, A. Wright, D. Bahr, and W.W. Gerberich: Yield strength predictions from the plastic zone around nanocontacts, *Acta Mater.* **47**, 333-343 (1998)

47. S.V. Hainsworth, H.W. Chandler, and T.F. Page: Analysis of nanoindentation load-displacement loading curves, *J. Maters. Res.* **11**, 1987-1995 (1996)

48. S. Timoshenko and S. Woinowshy-krieger: *Theory of plates and shells*, Mcgraw-Hill, New York (1959)

49. W.D. Kingery, H.K. Bowen, and D.R. Uhlman, *Introduction to Ceramics 2nd Ed.,* Wiley, New York, 777 (1976)

50. G.W.C. Kaye and T.H. Laby, *Tables of Physical and Chemical Constants*, 14th ed., Longman, London, 31 (1973)

51. B.R. Lawn: Fracture and deformation in brittle solids: A perspective on the issue of scale, *J. Mater. Res.* **19**, 22-29 (2004)

52. J.P. Den Hartog: *Advanced strength of Materials*, Dover Publications Inc., New York (1952)

53. G.C. Sih: *Handbook of Stress Intensity Factors*, Lehigh University, Bethlehem, PA (1973)

54. D.F. Bahr, C.L. Woodcock, M. Pang, K.D. Weaver, and N.R. Moody: Indentation induced film fracture in hard film – soft substrate systems, *Inter. J. Frac.* **119/120**, 339-349 (2003)

55. D. Kramer, H. Huang, M. Kriese, J. Robach, J. Nelson, A. Wright, D. Bahr, and W.W. Gerberich: Yield strength predictions from the plastic zone around nanocontacts, *Acta Mater.* **47**, 333-343 (1998)

56. G. Alcala, S. Mato, P. Skeldon, G.E. Thompson, A.B. Mann, H. Habazaki, K. Shimizu: Mechanical properties of barrier-type anodic alumina films using nanoindentation, *Surf. Coat. Tech.* **173**, 293-298 (2003)

57. S.W. Wiederhorn: Fracture of sapphire, *J. Amer. Ceram. Soc.* **52**, 9, 485-491 (1969)

58. W.P. Minnear and R.C. Bradt: Stoichiometry Effects on the fracture of TiO2-x, *J. Amer. Ceram. Soc.* **63**, 485-489 (1980)

59. O. Anderson, C. R. Ottermann, R. Kuschnereit, P. Hess, and K. Bange: Density and young's modulus of thin TiO2 films, Fresenius Journal of Analytical Chemistry **358**, 315-318 (1997)

60. W.P Minnear and R.C. Bradt: Elastic properties of polycrystalline titanium oxide (TiO2-x), *J. Amer. Ceram. Soc.* **60**, 458-459 (1977)

61. M.H. Grimsditch and A.K. Ramdas: Elastic and elasto-optic constants of rutile from a Brillouin scattering study, *Phys. Rev.* **B14**, 1670-1682 (1976)

62. M. Iwasa and T. Ueno: Fracture toughness of quartz and sapphire single crystals at room temperature, *Zairyo* **30**, 337, 1001-1004 (1981)

63. G.R. Anstis, P. Chantikul, B.R. Lawn, and D.B. Marshall: A critical evaluation of indentation techniques for measuring fracture toughness: I direct crack measurements, *J. Amer. Ceram. Soc.* **64**, 9, 533-538 (1981)

64. W. Zielinski, H. Huang, and W.W. Gerberich, J "Microscopy and microindentation mechanics of single crystal Fe-3 wt. % Si: Part II. TEM of the indentation plastic zone", *J. Mater Res.*, Vol. 8 (1993) pp. 1300-1310.

65. S. M. Hu "On indentation dislocation rosettes in silicon" *Journal of Applied Physics,* Vol. 46, No. 4, (1975) pp. 1470-1472.

66. Y. Gaillard, C. Tromas and J. Woirgard "Pop-in phenomenon in MgO and LiF: observations of dislocation structures" *Philosphical Magazine Letters,* Vol. 83, No. 9, (2003) pp. 553-561.

67. Rebecca Howland and Lisa Benetar *A Practical Guide to Scanning Probe Microscopy* Park Scientific Instruments (1993-1997) pp. 38-40.

68. N.A. Stelmashenko, M. G. Walls, L. M. Brown and Yu. V. Milman, "Microindentations on W and Mo oriented single crystals: An STM study", *Acta Metallurgica et Materialia* Vol. 41 (1993) pp. 2855-2865.

69. D.F.Bahr, J.C.Nelson, N.I. Tymiak, and W.W.Gerberich. the mechanical behavior of a passivating surface under potentiostatic control. *J. Mater. Res.* **12** (1997) 3345-3353

70. P. Hones and F. Levy. Influence of deposition parameters on mechanical properties of sputter-deposited Cr2O3 thin films. *J. Mater .Res.* **14** (1999) 3623-3629

71. A. Alamr, R.S. Yasser, D.F Bahr, L. Scudiero, and M. G. Norton. Correlating structure and mechanical behavior of passive films on austenitic stainless steels. *Submitted to Corrosion (2005)*

72. J.L. Dawson, and M. Ferreira. Electrochemical studies of the pitting of austenitic stainless steel. *Corrosion Science* **26** (1986) 1009-1026

73. I.Olefjord and L. Wegrelius. Surface analysis of passive state. *Corrosion Science.* **31** (1990) 89-98

74. G. Okamoto. Passive film of 18-8 stainless steel structure and its function. *Corrosion Science.* **13** (1973) 471-489

75. S. Haupt, C. Calinski, U. Collisi, H.W. Hoppe, H.D. Speckmann, and H.H. Strehblow. XPS and ISS examinations of electrode surfaces and passive layers with a specimen transfer in a closed system. *Surf. Interface Anal.* **9** (1986) 357-365

76. J.A.Bardwell, G.I.Sproule, and M.J. Graham. Ex situ surface analysis of passive films on iron-chromium alloys. When is it valid? *J. Electrochem. Soc* **140** (1993) 50-53

77. S.A. Syed Asif, K.J. Wahl, and R.J. Colton. The influence of oxide and adsorbates on the nanomechanical response of silicon surfaces. *J. Mater .Res.* **15** (2000) 546-553

78. U.Kamachi Mudali, and Y. Katada. Electrochemical atomic force microscopic studies on passive films of nitrogen-bearing austenitic stainless steels. *Electrochimica Acta.* **46** (2001) 3735-3742

79. J. Thurn and R.F. Cook: Mechanical and thermal properties of physical vapour deposited alumina films: Part II Elastic, plastic, fracture, and adhesive behaviour, *J. Mater. Sci.* **39**, 4809-4819 (2004)

Distribution List

1	MS 9405	Robert W. Carling, 8700
1	MS 9409	Paul A. Spence, 8754
5	MS 9409	Neville Moody, 8754
2	MS 9018	Central Technical Files, 8945-1
2	MS 0899	Technical Library, 4536
1	MS 0188	D. Chavez, LDRD Office, 1011